The Astrophysics of Active Galactic Nuclei Variability in Large Scale Spectroscopic Surveys

John J. Ruan

A dissertation
submitted in partial fulfillment of the
requirements for the degree of

Doctor of Philosophy

University of Washington

2017

Reading Committee:

Scott F. Anderson, Chair

Matthew McQuinn

Eric Agol

Program Authorized to Offer Degree:
Astronomy

University of Washington

Abstract

The Astrophysics of Active Galactic Nuclei Variability
in Large Scale Spectroscopic Surveys

John J. Ruan

Chair of the Supervisory Committee:
Professor Scott F. Anderson
Department of Astronomy

More than 50 years after the initial discovery of the extragalactic nature of quasi-stellar objects (quasars) by Schmidt (1963), studies of luminous active galactic nuclei (AGN) have revolutionized our understanding of black hole growth across cosmic time, accretion and jet physics, as well as galaxy evolution and cosmology. In the coming decade, these studies will be further fueled by large (a few $\times 10^6$) samples of quasars from massive optical spectroscopic surveys (e.g., from eBOSS and DESI). These spectra will be accompanied by well-sampled photometric light curves from time-domain imaging surveys (e.g., from Pan-STARRS and LSST), enabling discovery of rare objects and new time-domain phenomena.

Current spectroscopic and imaging surveys have well-established that nearly all Type 1 quasars are optically variable, although the origin of this variability is still unknown. The primary goal of this thesis is to investigate various AGN variability phenomena in the UV/optical, to understanding their origin. In particular, I investigate the origin of 10-20% flux variability ubiquitously observed in quasars, the apparent change in accretion states observed in 'transition blazars', as well as the rapid fading observed in the recently-discovered 'changing-look quasars' phenomenon. I also prepare for the science enabled by the large samples of AGN that will be discovered in future time-domain imaging surveys, by characterizing the unique properties of variability-selected AGN.

The primary technique I use in this dissertation to probe AGN variability is repeat optical spectroscopy. AGN optical spectra contain a wealth of information about the central engine, encoded in the properties of the emission lines, absorption lines, and continuum emission. Repeat optical spectroscopy can further probe the time-variable nature of these emission components, but this has previously been little explored in comparison to single-epoch spectroscopy. One notable exception in repeat AGN spectroscopy is the well-established reverberation mapping technique of mapping the size of AGN broad line regions; this has lead to the development of black hole mass estimates based on broad Balmer emission line widths in single-epoch spectroscopy. However, these and other studies based on repeat AGN spectroscopy are only available for small samples of a few dozen AGN at low redshifts, due to the expensive nature of repeat spectroscopy for large samples of faint quasars at higher redshifts. The development of multi-object spectrographs now have the ability to do repeat spectroscopy for large numbers of quasars, opening new windows into AGN astrophysics in the time-domain. Surveys dedicated to repeat quasar spectroscopy, including currently in SDSS-IV and in the future in SDSS-V, will fuel the early science results from this dissertation.

In this dissertation, I first use SDSS repeat spectroscopy of quasars to quantify the bluer-when-brighter trend of wavelength-dependent quasar spectral variability, and use it to constrain simple models of quasar variability. In particular, I test whether the observed spectral variability is consistent with recent toy models of inhomogeneous accretion disks with large temperature fluctuations. These models provide a natural explanation for quasar UV/optical variability, and the first to be consistent with measurements of quasar accretion disk sizes and characteristic timescales of variability. I show that the observed spectral variability can be reproduced by strongly inhomogeneous disks with large temperature fluctuations.

I then use SDSS repeat spectroscopy to investigate the origin of the 'transition blazars' phenomenon, which is observed in a handful of AGN with relativistic jets aligned with the line of sight. In transition blazars, the blazars appear to switch between BL Lac objects and

Flat-Spectrum Radio Quasars (FSRQs) classifications, which correspond to low- and high-accretion rate states, respectively. I show that transition blazars are FSRQs with especially strong beaming, such that the strongly-beamed continuum swamps the broad emission lines. This occasionally causes the broad emission lines to disappear and reappear, producing the transitional behaviour.

Furthermore, I mine SDSS repeat spectroscopy to uncover the origin of the recently-discovered 'changing-look quasars' phenomenon. Repeat optical spectroscopy of this new class of objects show dramatic transitions from luminous broad line quasars into quiescent galaxies or low-luminosity AGN. Surprisingly, these changes occur over timescales of just a few years, a factor of $>10^4$ faster than both theoretical expectations and scaling spectral state transition timescales in X-ray binaries to $10^8 M_\odot$ supermassive black holes (SMBHs). To understand this phenomenon, I perform the first large systematic search for CL quasars and I show that the fading of the continuum and broad emission lines in CL quasars is consistent with rapidly decreasing accretion rates, while disfavoring alternative interpretations including changes in intrinsic dust extinction and transient tidal disruption events or supernovae.

Finally, future time-domain imaging surveys such as the ZTF and LSST will discover a few $\times 10^7$ variable objects, and AGN will constitute the majority of variable objects discovered. To understand the science enabled by these massive variability-selected samples of AGN, I utilized spectra from the Time-Domain Spectroscopic Survey (TDSS) to understand the unique properties of variability-selected quasars. TDSS is the first systematic spectroscopic survey of variable objects, and I show that variability-selected quasars complement color-based selection by selecting additional redder quasars, resulting in a smooth redshift distribution. Furthermore, I show that variability selection yields higher fractions of peculiar AGN such as broad absorption line quasars and blazars.

TABLE OF CONTENTS

LIST OF FIGURES

Chapter 1
INTRODUCTION

The field of Active Galactic Nuclei (AGN) is broad, spanning topics from strong-field gravity to galaxy evolution. This dissertation focuses primarily on the astrophysics of UV/optical variability of AGN from an observational perspective. To motivate the investigations in this dissertation in a broader context, I provide a brief overview of the theoretical and observational properties of AGN in this chapter. At the beginning of each subsequent chapter, more detailed introductions specific to the individual investigation in that chapter are provided.

1.1 Overview of Active Galactic Nuclei

1.1.1 Supermassive Black Hole Accretion

A supermassive black hole (SMBH) is believed to exist at the center of every massive galaxy (Kormendy & Richstone, 1995), including our own Milky way (Genzel & Townes, 1987). Ranging from 10^{6-10} $M_{\odot}$ in mass, SMBHs grow over cosmic time primarily through the accretion of gas (Alexander & Hickox, 2012). Actively accreting SMBHs are termed active galactic nuclei (AGN), and are observable in the local and distant Universe up to redshifts of $z > 7$ (Mortlock et al., 2011). During periods of high accretion rates (and thus fastest growth), they are amongst the most luminous persistent objects in the universe (with luminosities of $\gtrsim 10^{45}$ erg s^{-1}), and are commonly referred to as 'quasars'. Conversely, during periods of low accretion rates (with luminosities of $\lesssim 10^{45}$ erg s^{-1}), they are referred to as 'low-luminosity AGN'. At the lowest of accretion rates, AGN may even appear to be nearly quiescent, like the slowly-accreting SMBH at the Galactic center (Melia & Falcke, 2001).

Observations show that AGN come in a wide variety of types, which stem at least in

part from orientation effects (Urry & Padovani, 1995; Antonucci, 1993). Orientation-based unification assumes a common structure for AGN that include: (1) an accretion disk of gas surrounding the central SMBH, (2) a broad line region of gas with high velocity dispersion, (3) a collimated relativistic jet launched from the inner accretion disk with small opening angle, (4) a torus of dust at distances of light-weeks beyond the dust-sublimation radius, and (5) a narrow line region of AGN-photoionized gas that extends to kpc-scale distances. In this framework, for the same AGN observed at different orientations, the observed diversity of AGN types is due to the different structures that are observable along the line of sight (see Figure 1). For example, a quasar observed perpendicular to its jet axis would have its central engine (including the accretion disk and broad line region) obscured by the dust torus, although strong jets and radio lobes may be observable (Antonucci & Ulvestad, 1985). At angles closer to the jet axis, the accretion disk and broad line gas emission would be observable, although these emission may be swamped by jetted synchrotron emission if the jet is aligned along the line of sight (Kollgaard et al., 1992).

At the same orientation, AGN can also appear dramatically different depending on the accretion state of the quasar. At high accretion rates (approximately $\gtrsim$0.1 times the Eddington limit), the accretion disk is theoretically expected to be geometrically-thin and optically-thick (Lynden-Bell & Rees, 1971; Pringle & Rees, 1972). The high luminosities of quasars imply that the radiative efficiencies of these disks are high, with $\eta \sim 0.1$ - 0.3 (e.g., Soltan, 1982; Haehnelt et al., 1998; Davis & Laor, 2011), where the luminosity is $L = \eta \dot{M}_{\rm BH} c^2$. These thin accretion disks are believed to be able to photoionize a broad line region of gas, support a dust torus, and occasionally produce a relativistic jet. At low accretion rates ($\lesssim$0.01 times the Eddington limit), the accretion flow is theoretically expected to dramatically transition to become geometrically-thick and optically-thin (Narayan & Yi, 1994). The low gas density enables energy in the hot gas to be directly advected into the SMBH rather than be radiated, resulting in a low-luminosity AGN with low radiative efficiency. In this accretion regime, the central engine is not observed to host broad line regions or dusty tori, but collimated jets are commonly observed.

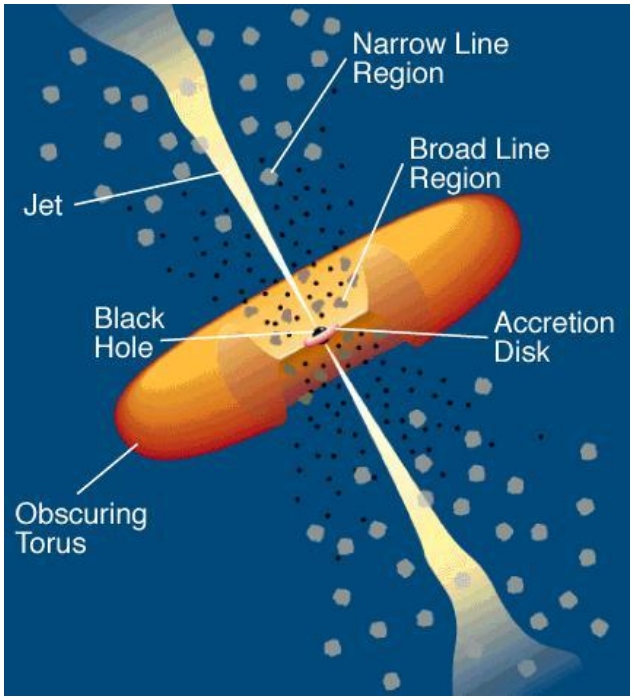

Figure 1.1: The general structure of AGN central engines include: (1) an accretion disk surrounding the SMBH, (2) a broad line region of high-velocity gas, (3) a dusty torus, (4) a narrow line region of photoionized gas, and (5) a relativistic jet. Orientation-based schemes of AGN unification posit that different types of observed AGN have similar fundamental structure, but their apparent differences are a geometric effect because they are observed along different lines of sight. Figure from Urry & Padovani (1995).

1.1.2 Accretion Disks

The high luminosities of quasars strongly suggest that gravitational collapse of gas onto SMBHs is releasing gravitational potential energy into radiation (Lynden-Bell, 1969). Conservation of angular momentum will cause the gas to settle into a rapidly-spinning accretion disk, where some source of viscosity will cause gas to accrete onto the SMBH (Pringle, 1981). In luminous unobscured quasars, the optical/UV continuum emission spectrum (the 'big blue bump') has long been believed to originate in an accretion disk (Shields, 1978; Malkan

& Sargent, 1982) described by the simple Shakura-Sunayev thin disk model (Shakura & Sunyaev, 1973). In this model, gas rotating in the accretion disk release its gravitational energy by emitting thermal radiation. The temperature of the disk is dependent on radius from the central SMBH, and highest at the inner most stable circular orbit. The resulting multi-temperature blackbody spectral energy distribution (SED) for thin disks is generally a power-law in the optical, with a exponential Wien cutoff in the UV. At longer wavelengths, dust emission overwhelms the Rayleigh-Jeans tail of the SED.

Despite its eminence, there is a plethora of inconsistencies between Shakura-Sunayev thin disk model and observations of quasars (Antonucci, 2015). Firstly, the observed UV spectrum in nearby AGN is significantly more luminous than the predicted Wien cutoff (Zheng et al., 1997; Shang et al., 2005), and does not appear to scale with properties of the SMBH such as $M_{\rm BH}$ and luminosity (Bonning et al., 2007; Davis et al., 2007). Secondly, measurements of accretion disk sizes in AGN from gravitational microlensing (e.g., Morgan et al., 2010; Blackburne et al., 2011; Jiménez-Vicente et al., 2014) and X-ray/UV/optical reverberation time-lag observations (e.g., McHardy et al., 2014; Edelson et al., 2015; Jiang et al., 2017) now consistently infer disk sizes that are factors of a few larger than predicted. This suggests that the disk thermal emission is not emitted at the radius where the gravitational energy of the gas is released in the gravitational potential of the SMBH. Finally, observations of the complex temporal variability of the UV/optical emission is difficult to reconcile with this static disk model (see Section 1.2). These (and other) inconsistencies present serious challenges to the validity of the Shakura-Sunayev disk model.

1.1.3 Relativistic Jets

AGNs often produce collimated jets that emit strongly in the radio through synchrotron radiation. In many radio galaxies, observations show narrow jets that inflate giant radio lobes on both sides of the galaxy. These jets are launched at relativistic speeds, reaching Lorentz factors of order ~ 10. Relativistic jets are thought to be produced by the Blandford-Znajek mechanism (Blandford & Znajek, 1977), through the acceleration of relativistic electrons by

twisted poloidal magnetic fields anchored in the inner accretion disk (Begelman et al., 1984). Although relativistic jets are most commonly observed in low-luminosity AGN, they can also be produced by high-luminosity quasars. Since the accretion flow in these two regimes is different, the jet triggering mechanism may be distinct at high- and low-accretion rates (Maraschi & Tavecchio, 2003; Ghisellini & Tavecchio, 2008), but this is an open question.

Perhaps the clearest indication of relativistic jets from both high- and low-luminosity AGN comes from observations of blazars. Blazars are rare radio-loud AGNs in which a relativistic jet is aligned closely along the line of sight, i.e. observed directly 'down the barrel' of the jet (Blandford & Rees, 1978). Due to relativistic beaming effects, the non-thermal jet emission is Doppler boosted in luminosity and completely dominates the SED, while time dilation causes the jet emission to be highly variable on timescales as short as hours. Blazars are observed to exist in both low-luminosity AGNs and high-luminosity quasars, referred to as BL Lac objects and flat-spectrum radio quasars, respectively (Stickel et al., 1991; Stocke et al., 1991). Intriguingly, previous observations have suggested that some rare blazars actually transition from one class to another (Ghisellini et al., 2011; Shaw et al., 2012). It is possible that these rare 'transition blazars' are be undergoing rapid switches between low- and high-Eddington accretion modes. In Chapter 3, I search for and investigate the nature of these 'transition blazars', to test if the central engine is indeed switching between high- and low-accretion rate regimes.

1.2 Observable Properties of AGN Variability

A defining characteristic of AGN emission is its temporal variability (Ulrich et al., 1997). Depending on orientation, the UV/optical continuum emission from the central engine can dominated by either the accretion disk or jet emission, and both are known to be highly variable. However, the physical mechanism producing this UV/optical variability is highly unclear. The continuum variability may be inherent in the thermal emission from the accretion disk, but this is not encapsulated in the static Shakura-Sunyaev disk model, and radiative magnetohydrodynamic simulations of accretion disks are not yet able to reproduce

the observations. Alternatively, if the thermal emission stems primarily from heating of the disk by X-rays from a corona (Frank et al., 2002; Cackett et al., 2007), the UV/optical variability may instead be driven by variability in the X-rays. This reprocessing interpretation has support from multi-wavelength monitoring observations that show the UV/optical emission lags the X-rays in some AGN (Shappee et al., 2014; McHardy et al., 2014). However, other observations show no such lag (Uttley et al., 2003; Starkey et al., 2017) or even the opposite lag in other AGN (Maoz et al., 2000; Arévalo et al., 2005), while the origin of the variability in the X-ray emission is also unclear. Further insights into the physics of AGN UV/optical variability will have to be teased from large samples of light curves.

The proliferation of optical photometric time-domain surveys have now produced well-sampled light curves with decades-long baselines, enabling statistical studies to characterize the variability and understand its origin. Surveys such as SDSS Stripe 82 have confidently revealed that quasar UV/optical variability is well-described by a first-order continuous autoregressive process (Kelly et al., 2009; MacLeod et al., 2010), also known as a damped random-walk. In this model, variability is correlated with amplitude that increases in variance as a function of time-lag between observations. The variance saturates to a maximum of $\sim$10-20% in flux at a characteristic timescale of $\sim$200 days. Intriguingly, the variability amplitudes are also well-known to be correlated with physical properties of the quasars, including black hole mass ($M_{\rm BH}$) and luminosity (Hook et al., 1994; Vanden Berk et al., 2004; Wilhite et al., 2008). Complementing these photometric observations, repeat spectroscopic observations of quasars have revealed that the UV/optical continuum turns bluer in color when the quasar gets brighter (Vanden Berk et al., 2004; Wilhite et al., 2005). The physical origin for all these observed properties is unclear, although thermal fluctuation in the accretion disk has been suggested (Kelly et al., 2009, 2011). In Chapter 2, I compare the spectral variability of quasars as observed in repeat optical spectroscopy to recent time-dependent accretion disk models that can explain these variability properties.

1.2.1 Accretion State Transitions in Supermassive Black Holes

Over cosmic time, quasar activity peaks at redshift $z \sim 2$, but galaxies in the local Universe are instead observed to be quiescent or host low-luminosity AGN. This implies that accretion onto SMBHs have shut down in our recent past, possibly due to quasar feedback processes that operate in the host galaxies (Fabian, 2012). Accretion state transitions from high- to low-accretion regimes are commonly observed in stellar BH X-ray binary systems, where the hours-long timescales for this process to occur are shorter (e.g., Homan & Belloni, 2005). It is commonly thought that the physics of accretion around stellar mass BHs directly scales up to SMBHs (Sobolewska et al., 2011), but the long 10^{4-5} year timescales expected for accretion state transitions to occur in SMBHs makes direct comparison to observations of X-ray binaries difficult (Done et al., 2007).

Evidence for accretion shutdown in individual quasars have been scarce, and comes primarily from the discovery of 'voorwerps'. Voorwerps are kpc-scale emission line clouds around currently-quiescent galaxies, photoionized by past quasar activity (Lintott et al., 2009; Schawinski et al., 2010; Keel et al., 2012a). The quasar in the host galaxy has shut off, leaving the voorwerp as a photoionization echo of its previous luminous state. However, the recent discovery of 'changing-look quasars' (LaMassa et al., 2015), has upended our understanding of SMBH accretion state transition. These objects display dramatic transitions from luminous quasars to quiescent states (and vice versa, Gezari et al. 2017), over surprisingly short timescales of just a few years. If this phenomenon is indeed due to accretion state transitions, this may indicate that the physics of accretion does not directly scale from stellar mass BHs to SMBHs. However, other possible explanations have been suggested, including variable dust obscuration (Runnoe et al., 2016), transient tidal disruption events (Merloni et al., 2015), and Type IIn supernovae (Ruan et al., 2016a). In Chapter 4, I undertake the first systematic search for changing-look quasars and investigate the origin of their dramatic transitions.

1.3 The Sloan Digital Sky Survey

Nearly all of the spectroscopic data used in this dissertation comes from the Sloan Digital Sky Survey (SDSS, York et al., 2000). The SDSS is a 2.5m telescope at Apache Point Observatory in New Mexico, and has operated since 2000 in several phases, each with difference science programs (Gunn et al., 2006). SDSS began as a multi-filter wide-field imaging survey (Gunn et al., 1998) to provide the first digital image of the full northern sky (Padmanabhan et al., 2008), but included a complementary multi-object optical spectroscopic redshift survey. The original spectrograph used 640 optical fibers, and was later upgraded to a 1000-fiber spectrograph in SDSS-III that provided a wider wavelength range (Smee et al., 2013). To date, the ongoing SDSS project has obtained more than 4 million spectra, including ∼400,000 quasars.

A powerful component of SDSS is its robust data reduction pipeline, enabling public release of well-calibrated data. Optical spectra from SDSS are reduced using the spec2d pipeline, which extracts and calibrates the individual exposures into stacked 1 dimensional spectra. The spectrophotometric calibration is based on spectra of standard stars that were simultaneously observed with the science targets on each plate. Automated classification and redshift estimates for the resulting spectra are performed using the spec1d pipeline (SubbaRao et al., 2002; Bolton et al., 2012). Due to the diverse and non-linear nature of quasar spectra, visual inspection of each quasar targeted in SDSS-I/II/III provided additional assurance of the reliability of the automatic classification and redshift estimates (e.g., Schneider et al., 2010; Pâris et al., 2017). In SDSS-IV, the sheer volume of quasar targets prevented visual inspection for the majority of quasar targets. The resulting proprietary data is available for immediate download to the SDSS collaboration, and later to the general public as part of planned yearly data releases (e.g., SDSS Collaboration et al., 2016) through the Science Archive Server and SkyServer online interfaces (Weaver et al., 2015).

Several science programs in SDSS specifically targeted quasars for spectroscopy. For example, the Baryon Oscillation Spectroscopic Survey in SDSS-III (Dawson et al., 2013)

targeted quasars at $z > 2.2$ for Lyman-α forest studies (Ross et al., 2012), while the Extended Baryon Oscillation Spectroscopic Survey in SDSS-IV (Dawson et al., 2015) targeted quasars at $0.9 < z < 2.2$ for cosmological clustering studies (Myers et al., 2015). Furthermore, the SDSS spectroscopic archive contains a large number ($\gtrsim$30,000) pairs of repeat spectra of quasars, spanning a wide range in time-lag up to $\gtrsim$10 years in the rest-frame. These repeat spectra include serendipitous repeat observation, as well as those specifically targeted for repeat observation as part of the survey plan. For example, the Time-Domain Spectroscopic Survey (Morganson et al., 2015; Ruan et al., 2016b) in SDSS-IV targeted $\sim$13,000 quasars for repeat spectroscopy in its Few-Epoch Spectroscopy and Repeat Quasar Spectroscopy programs for a variety of science goals (MacLeod et al., 2017). In several of the investigations in this dissertation, I mine these repeat SDSS quasar spectra to probe various aspects of AGN variability. The initial science results yielded from these repeat quasar spectra provides a preview of the science enabled by future time-domain spectroscopic and photometric surveys (including SDSS-V, ZTF, and LSST), which will obtain much larger samples.

1.4 Outline of this Dissertation

Each chapter in this dissertation describes a discrete project with a distinct science goal, under a overall theme of AGN variability. In Chapter 2, I use SDSS repeat quasar spectra to understand the wavelength-dependent UV/optical spectral variability of accretion disk emission, to constrain models of quasar variability. In Chapter 3, I mine SDSS repeat blazar spectra to search for 'transition blazars' that appear to transition between BL Lac and flat-spectrum radio quasar classifications, and use their multi-wavelength properties to understand their nature. In Chapter 4: I mine SDSS repeat quasar spectra to provide the first sample of 'changing-look quasars', in which quasars appear to transition between quiescent and luminous states, and test various scenarios for the origin of this phenomenon. In Chapter 5, I investigate the properties of quasars from the Time-Domain Spectroscopic Survey, to understand the unique properties of variability-selected quasars. In Chapter 6, I conclude and discuss future directions for research as a result of my work.

Chapter 2

EVIDENCE FOR LARGE TEMPERATURE FLUCTUATIONS IN QUASAR ACCRETION DISKS FROM SPECTRAL VARIABILITY

UV/optical continuum variability is a ubiquitous characteristic of quasars. Although the continuum emission is known to originate from the accretion disk, the variability mechanism is unknown. The observed variability has many interesting properties, including the well-known bluer-when-brighter trend. This trend is is a signature of the complex processes in the accretion disk, and can be a probe of the quasar variability mechanism. In this chapter, I use a sample of 604 variable quasars with repeat spectra in SDSS-I/II, and construct difference spectra to investigate the physical causes of this bluer-when-brighter trend. The continuum of our composite difference spectrum is well-fit by a power-law, with a spectral index in excellent agreement with previous results. I measure the spectral variability relative to the underlying spectra of the quasars, which is independent of any extinction, and compare to model predictions. I show that our SDSS spectral variability results cannot be produced by global accretion rate fluctuations in a thin disk alone. However, I find that a simple model of a inhomogeneous disk with localized temperature fluctuations will produce power-law spectral variability over optical wavelengths. I show that the inhomogeneous disk will provide good fits to our observed spectral variability if the disk has large temperature fluctuations in many independently varying zones, in excellent agreement with independent constraints from quasar microlensing disk sizes, their strong UV spectral continuum, and single-band variability amplitudes. My results provide an independent constraint on quasar variability models, and add to the mounting evidence that quasar accretion disks have large localized temperature fluctuations.

Material from this chapter was previously published in collaboration with Scott F. Anderson, Jason Dexter, and Eric Agol in the March 2012 edition of the Astrophysical Journal (Ruan et al., 2014a), and has been reproduced here with permission of the American Astronomical Society.

2.1 Introduction

A well-known characteristic of the quasar phenomena is their strong flux variability in many wavelength regimes, including the radio, optical, X-ray, and γ-rays (Ulrich et al., 1997). In particular, the rise of optical large-scale time-domain imaging surveys has led to many recent investigations of broadband quasar optical variability properties using large numbers of well-sampled light curves, especially for use in quasar selection (Kelly et al., 2009; Kozłowski et al., 2010; MacLeod et al., 2010; Schmidt et al., 2010; Butler & Bloom, 2011; Kim et al., 2011; MacLeod et al., 2011; Ruan et al., 2012; Andrae et al., 2013; Zu et al., 2013). These studies have generally revealed that quasars are stochastically variable on the $\sim$10-20% level in flux on long time-scales, and show weaker, correlated variability on timescales $\lesssim 1$ year in the rest-frame. The physical cause of quasar variability is still unclear, but since the optical continuum is likely to be dominated by emission from the accretion disk, some studies have suggested that changes in the global accretion rate in the disk may be able to produce such effects (Pereyra et al., 2006; Li & Cao, 2008; Zuo et al., 2012). These claims appear to be supported (although not implied) by various observed trends between optical variability amplitude, black hole mass, and luminosity in different quasars (Hook et al., 1994; Garcia et al., 1999; Vanden Berk et al., 2004; Wilhite et al., 2008; Bauer et al., 2009a; Kelly et al., 2009; MacLeod et al., 2010; Zuo et al., 2012), in turn suggesting that the differences in variability across a sample of quasars may be driven at least in part by their Eddington ratio.

Accretion rate fluctuations are expected in individual quasars due to processes in the disk such as the magnetorotational instability (MRI, Balbus & Hawley, 1991), which is now generally accepted to operate in a wide range of accretion flows. Results from non-radiative global simulations of thin magnetized disks have also shown that such accretion flows are

almost certain to be highly turbulent (e.g. Armitage et al., 2001; Armitage & Reynolds, 2003; Noble et al., 2009; Noble & Krolik, 2009; Penna et al., 2010), but the exact characteristics of a MRI flow in a global radiative MHD simulation are currently unclear, especially their stability in the radiation pressure-dominated regime (see discussions in Hirose et al., 2009; Janiuk & Misra, 2012; Jiang et al., 2013). Localized temperature fluctuations in highly turbulent disks will also cause flux variations, and such a scenario may be expected since quasar accretion disks are too large to vary coherently in flux over the short variability timescales observed. The characteristic timescales of quasar flux variability have also been shown to be consistent with the thermal timescale (Kelly et al., 2009), independently motivating accretion disk models involving localized temperature fluctuations. Furthermore, it has been shown that such models of inhomogeneous accretion disks can also simultaneously explain quasar microlensing disk sizes, their strong UV spectral continuum, and single-band optical variability properties (Dexter & Agol, 2011).

Although the relative roles of global accretion rate fluctuations and localized temperature fluctuations in accounting for the observed flux variability are unclear, an additional probe is provided by the characteristic bluer-when-brighter trend observed in studies of quasar spectral variability (Cutri et al., 1985; Giveon et al., 1999; Trèvese et al., 2001; Trèvese & Vagnetti, 2002; Vanden Berk et al., 2004; Wilhite et al., 2005; Meusinger et al., 2011; Sakata et al., 2011; Schmidt et al., 2012; Meusinger & Weiss, 2013). This trend is almost certainly a direct consequence of the underlying quasar variability mechanism, and thus provides an independent test of quasar variability models. Indeed, both global accretion rate changes and localized temperature fluctuations in accretion disks will generically produce bluer-when-brighter trends, but the details of the predicted trend are dependent on the details of the model. Intriguingly, previous investigations of quasar spectral variability have sometimes resulted in disparate conclusions.

Wilhite et al. (2005) used a sample of 315 pairs of repeat spectra of variable quasars from the Sloan Digital Sky Survey (SDSS, York et al., 2000), and constructed 'difference spectra', by taking the spectrum of each quasar at the higher-flux epoch and subtracting the spectrum

at the lower-flux epoch; this effectively isolates the variable part of the spectrum. After applying a wavelength-dependent spectrophotometric recalibration on each pair of repeat spectra, they find that the resulting composite quasar difference spectrum has a steeper power-law index than the composite of the individual spectra, showing that quasars are indeed bluer-when-brighter. Based on the composite difference spectrum from that study, Pereyra et al. (2006) fitted synthetic difference spectra generated from a simple Shakura-Sunayev thin disk model (Shakura & Sunyaev, 1973), and showed that the composite difference spectrum can be produced from a simple thin disk in which the global accretion rate has changed (also see Sakata et al., 2011).

In contrast, Schmidt et al. (2012) used a sample of 9093 multi-band quasar light curves from SDSS Stripe 82 to study the bluer-when-brighter trend using many epochs of broadband photometry. After correcting for the effects of broad emission lines (which are well-known to be less variable than the continuum) in each filter, they compare their results to spectral variability predictions from accretion rate fluctuations in a simple thin disk, as well as more detailed static disk models. They find that accretion rate changes in these disk models *cannot* reproduce the strong bluer-when-brighter trend, and instead suggest that ephemeral hot spots on the accretion disk may be needed (also see Trèvese & Vagnetti, 2002; Meusinger & Weiss, 2013).

The conclusions of Wilhite et al. (2005, hereafter WI05) and Schmidt et al. (2012, hereafter SC12) appear at first glance to be at odds: can the bluer-when-brighter trend observed in quasar be explained by fluctuations in the global accretion rate in a simple thin disk, or are localized temperature fluctuations needed? In this paper, we revisit the spectral variability study of WI05 using a larger sample of repeat quasar spectra culled from the full SDSS-I/II data set, to investigate these apparently discordant results. We will also compare our spectral variability results to the recently-developed time-dependent model of inhomogeneous accretion disks by Dexter & Agol (2011). The structure of this paper is as follows: In Section 2.2, we describe the construction of the sample of repeat quasar spectra used in this study, and our spectrophotometric recalibration. In Section 2.3, we discuss the proper-

ties of the quasars' difference spectra, as well as the construction of composite spectra and composite difference spectra. In Section 2.4, we compare our results to the previous studies of WI05 and SC12 using global accretion rate fluctuations in a thin disk. In Section 2.5, we discuss the quasar spectral variability predicted from a time-dependent model with temperature fluctuations, and show that our observations are well-fit by such inhomogeneous disks. In Section 2.6, we discuss the connection between disk properties and the resultant spectral variability, as well as other variability mechanisms that might match the observations. We summarize and conclude in Section 2.7.

2.2 Data Selection and Reduction

2.2.1 SDSS-I/II Repeat Spectra

All spectroscopic data used in our paper is from the SDSS-I/II, which is publicly available in its entirety as part of SDSS Data Release 7 (DR7, Abazajian et al., 2009). The SDSS-I/II obtained follow-up spectra of approximately 1.6×10^6 objects, including more than 1.1×10^5 quasars (Schneider et al., 2010), primarily selected by optical color from the imaging portion of the survey (Richards et al., 2002a). The two fiber-fed SDSS spectrographs utilize a total of 640 fibers plugged into holes drilled onto plates, which are placed at the telescope focal plane. During the normal course of operations, multiple 15-minute exposures of each plate are taken, and spectra from exposures within approximately a month are typically coadded together. The spectral reduction and calibration using the SDSS Spectro2d pipeline are described in Stoughton et al. (2002). Occasionally, entire plates may be reobserved and coadded separately as a second epoch of spectra. This may occur if the first epoch did not reach sufficiently high signal-to-noise ratios (SNR), or in some cases by design as part of the survey plan. For these multiply-observed plates, no attempt was made to ensure that the same fiber was plugged into the same hole on the plate, and so spectra of the same object may have different fiber numbers in the different epochs, even though the plate number is identical. For more details about these repeatedly observed plates, we refer to discussions in

Wilhite et al. (2005).

Although multiple epochs of SDSS spectra are also possible due to spatial overlaps in the sky between adjacent plates, Vanden Berk et al. (2004) showed that additional calibrations based on non-variable stars on the same plates enhance sensitivity to the wavelength-dependent variability properties of quasars. Overlapping regions on adjacent plates are generally small, and will not have many non-variable stars in the overlapping regions to accurately recalibrate the quasar spectra in the same regions. Thus, we focus only on multi-epoch spectra from plates that have been reobserved in their entirety, which ensures that multi-epoch spectra of many calibration stars are available in addition to the quasars. We also note that more epochs of spectra for many SDSS DR7 quasars are now publicly available as part of the SDSS-III Baryon Oscillation Spectroscopic Survey (Dawson et al., 2013). However, SDSS-III utilizes a newer spectrograph, fiber system, and spectral reduction pipeline; robust comparison of continuum properties of spectra between SDSS-I/II and SDSS-III are difficult and thus not considered here.

Using the plate list of 2880 observations of all 2698 unique plates in DR7 from SDSS-I/II, we select only those which are part of the main SDSS survey (and its primary reduction pipeline) by requiring the flag SURVEY = 'sdss'. A data quality cut is then made by requiring the flag PLATEQUALITY = 'good' or 'marginal'; plates which pass this quality cut have SNR > 9 and less than 13% problematic pixels. From the remaining plates, we select those which have multiple observations with time-lag >30 days between each pair of epochs in the observed frame. This time-lag cut is physically motivated from photometric studies of quasar light curves, which have shown that quasars are generally not variable above $\sim$1% in flux on such short timescales (Kelly et al., 2009; Kozłowski et al., 2010; MacLeod et al., 2011). We note that a few plates had three or more observations; in such cases, we use all unique pairs of observations of each plate that pass all the above criterion. There are a total of 71 unique pairs of plate observations in SDSS-I/II, which are listed in Table 2.1. Figure 2.1 shows the distribution of the timelags for these 71 pairs of plate observations, which range from 30 days to about 3 years in the observed-frame.

Table 2.1. All unique pairs of repeatedly-observed plates in SDSS-I/II with time-lag >30 days, PLATEQUALITY = 'good' or 'marginal', along with the number of quasars and variable quasars on each plate.

Plate Number	High-SNR MJD	Low-SNR MJD	Quasars	Variable Quasars
291	51660	51928	21	9
293	51994	51689	54	18
296	51578	51984	26	7
297	51663	51959	23	15
300	51666	51943	41	6
301	51641	51942	45	17
304	51957	51609	26	12
306	51690	51637	35	1
309	51666	51994	47	14
340	51691	51990	24	3
351	51780	51695	36	3
352	51789	51694	29	6
360	51780	51816	69	6
385	51783	51877	49	5
390	51816	51900	30	7
394	51876	51812	31	6
394	51812	51913	28	5
394	51876	51913	31	5
404	51877	51812	14	1
406	51817	51869	48	6

Table 2.1 (cont'd)

Plate Number	High-SNR MJD	Low-SNR MJD	Quasars	Variable Quasars
406	51876	51817	50	4
406	51817	51900	49	5
406	52238	51817	48	19
406	51900	51869	54	6
406	52238	51869	47	19
406	52238	51876	51	19
406	52238	51900	49	20
410	51816	51877	83	22
411	51873	51817	28	8
412	51871	51931	30	3
412	51871	52235	29	8
412	51871	52250	31	8
412	51871	52254	30	13
412	51871	52258	29	11
412	52235	51931	32	12
412	52250	51931	35	13
412	52254	51931	32	11
412	51931	52258	32	11
413	51821	51929	46	3
414	51869	51901	39	3

Table 2.1 (cont'd)

Plate Number	High-SNR MJD	Low-SNR MJD	Quasars	Variable Quasars
415	51879	51810	39	4
416	51885	51811	68	31
418	51884	51817	72	16
419	51812	51868	69	7
419	51812	51879	64	24
422	51878	51811	26	1
476	52027	52314	80	20
483	51942	51902	78	8
525	52029	52295	52	19
547	51959	52207	66	19
662	52178	52147	37	5
803	52264	52318	4	1
810	52326	52672	4	0
814	52370	52443	47	7
820	52405	52438	80	3
960	52466	52425	31	1
1028	52562	52884	3	2
1034	52525	52813	2	1
1037	52826	52878	1	0
1512	53035	53742	19	7

Table 2.1 (cont'd)

Plate Number	High-SNR MJD	Low-SNR MJD	Quasars	Variable Quasars
1670	53438	54553	41	19
1782	53383	53299	31	3
1905	53613	53706	21	5
1907	53265	53315	27	3
2009	53857	53904	44	3
2061	53405	53711	17	8
2252	53565	53613	0	0
2294	54524	53733	63	37
2394	54518	54551	0	0
2474	54333	54564	7	1
2858	54498	54464	1	1

2.2.2 Spectrophotometric Recalibration

We perform a wavelength-dependent spectrophotometric recalibration on all pairs of repeat quasar spectra on each plate, by first producing a 'recalibration spectrum' for each pair of observations based on the non-variable stars on each plate. This is done following WI05 with only minor modifications, to allow for faithful comparison to previous work. We note here that to facilitate our difference spectra analysis, we have resampled all spectra and their uncertainties onto a common wavelength grid of the form $\log_{10}\lambda = 2.602 + 0.001a$, for integers a from 0 to 1400 (λ in Å units). This is approximately a factor of 10 coarser than the actual SDSS spectral resolution, but appropriate for our investigation of the continuum properties

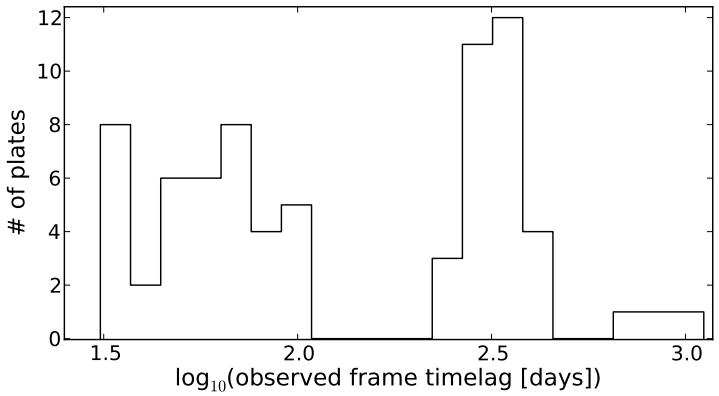

Figure 2.1: Distribution of the observed-frame time-lags between repeat observations of the 71 pairs of plate observations used in our sample (listed in Table 2.1).

of quasars. The resampling is done using a simple linear interpolation, and the resulting common wavelength grid covers 400 to 10,046Å, wide enough for all rest-frame spectra of the quasars in our sample. As part of the interpolation to the common wavelength grid, we mask out problematic pixels in the each spectrum which had SDSS pipeline flags set for NOPLUG, BADTRACE, BADFLAG, BADARC, MANYBADCOLUMNS, MANYREJECTED, NEARBADPIXEL, LOWFLAT, FULLREJECT, SCATTEREDLIGHT, NOSKY, BRIGHTSKY, COMBINEREJ, REDMONSTER (for details on these flags, see Stoughton et al., 2002). We consider only pairs of repeat spectra of objects for which <20% of pixels are rejected in both epochs.

For each pair of plate observations, all pairs of stellar spectra are selected by requiring the SDSS Spectro1d pipeline classification of both spectra to have CLASS = 'STAR' and their SUBCLASS classification to be identical between the two epochs. To remove the stars that have significantly varied between the two epochs, we integrate each pair of stellar spectra and calculate the relative change in flux of the star $\Delta f/f = |(f_1 - f_2)|/(0.5f_1 + 0.5f_2)$, where f_1 and f_2 are the integrated fluxes in the two epochs. Stars with large $\Delta f/f$ are unsuitable for use in the spectrophotometric recalibration due to their variability. Since

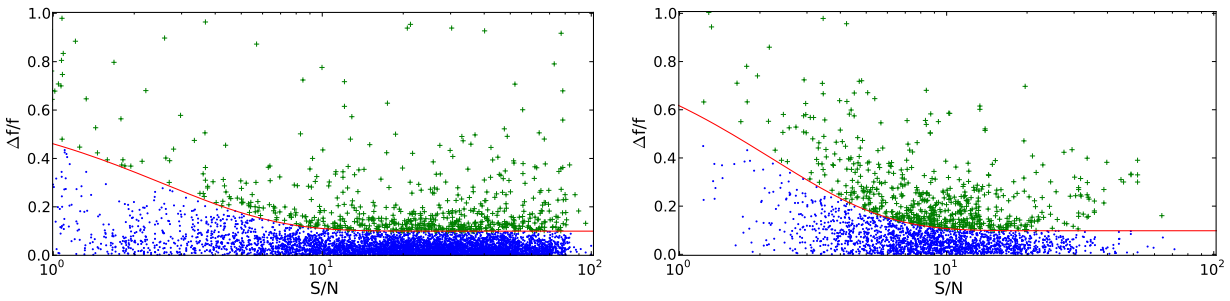

Figure 2.2: Left Panel: Relative flux change $\Delta f/f$ seen in repeat spectra of stars as a function of the SNR of the high-SNR epoch. The fitted exponential function (red solid line) divides stars deemed to be variable (green crosses) and non-variable (blue points). The non-variable stars are used to calculate a wavelength-dependent spectrophotometric recalibration for pairs of repeat spectra on each plate. Right Panel: $\Delta f/f$ as a function of SNR, similar to the top panel, but for known quasars after applying our spectrophotometric recalibration. The sample of variable quasars defined here is used to produce the composite spectra in Figure 2.5.

$\Delta f/f$ is dependent on the SNR of the spectra, we follow the procedure of WI05 to include the flux uncertainties on the spectra in the variability selection by placing a variability cut on $\Delta f/f$ as a function of the SNR; Figure 2.2 shows the distribution of $\Delta f/f$ against the SNR of high-SNR epoch spectra for all stars on the 71 plates. We bin the stars in Figure 2.2 into 13 equally-sized bins of SNR, and calculate the 90th percentile in $\Delta f/f$ in each bin. We then fit an envelope with these 13 points of 90th percentile $\Delta f/f$ to an exponential function of the form $\Delta f/f = 0.53\exp(\mathrm{SNR}/-0.57) + 0.10$. Stars with $\Delta f/f$ below this envelope are considered 'non-variable' (Figure 2.2), and are used in the subsequent spectrophotometric recalibration. There were 6327 stars in total over the 71 plates, 5615 of which were deemed to be non-variable. On a typical plate, a median of 47 non-variable stars were used in the spectrophotometric recalibration.

For each pair of non-variable stellar repeat spectra, we take the ratio of the lower-SNR

epoch spectrum to the higher-SNR epoch spectrum; for a non-variable star for which the two epochs of spectra are perfectly calibrated, this results in a flat ratio spectrum with ratio 1. However, plate-wide wavelength-dependent systematic calibration differences between the two epochs may be present. We take the median ratio spectrum of all non-variable stars on each plate and interpolate a 5th-order polynomial to reduce the effects of noise. Prior to the interpolation, we clip the top and bottom 3 percentile of pixels in the ratio spectrum to avoid skewing the interpolation from outlying pixels. The low-SNR epoch spectra of all quasars on each plate will be multiplied by this interpolated median ratio spectrum to match the calibration of the high-SNR epoch spectra. The interpolated median ratio spectra used in the spectrophotometric recalibration are generally a <5% correction at all wavelengths, and are almost all <10%, consistent with the findings of WI05.

To select all quasars in these 71 pairs of repeat plate observations, we match all spectra to the SDSS DR7 quasar catalog (Schneider et al., 2010) to find a total of 2,626 quasars, and apply the wavelength-dependent spectrophotometric recalibration for all quasars on each plate. Comparison of repeat spectra for objects that did not significantly vary between the two epochs will be dominated by noise, and so we place a SNR-dependent variability cut on the $\Delta f/f$ for each quasar, similar to the stars, but now to select variable quasars. After binning the quasars into 13 equal bins of SNR, we fit an exponential to the 75th percentile $\Delta f/f$ in each bin of the form $\Delta f/f = 0.81\exp(\mathrm{SNR}/-0.22) + 0.10$. We have used the 75th percentile $\Delta f/f$ in the variability cut rather than the 90th percentile used in the stellar case because quasars are known to be more strongly variable than stars in general (Sesar et al., 2007). Out of 2,626 quasars on the 71 plates, 626 are selected as spectroscopic variables. We note that by design, this sample of quasars we use to study spectral variability are those exhibiting the strongest variability; this is desirable for the present study to ensure high SNR of the spectral variability results.

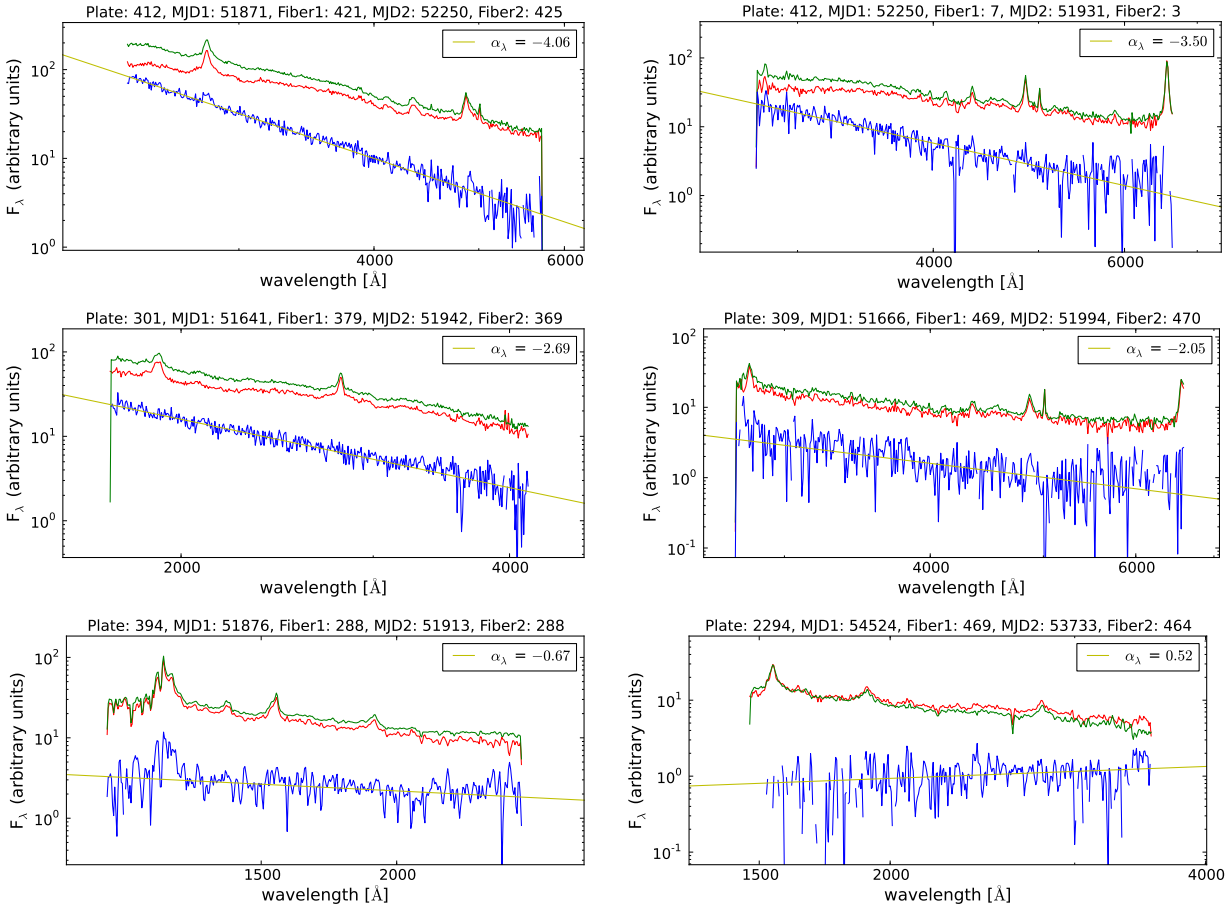

Figure 2.3: Examples of pairs of repeat variable quasar spectra (green and red), their difference spectra (blue), and best-fit power-laws to the difference spectra continuum (yellow), for a range of power-law indices of the difference spectrum. All spectra shown are corrected for Galactic extinction, and are scaled to arbitrary flux densities. The vast majority of the quasar repeat spectra in our sample show a strong bluer-when-brighter trend.

2.3 Quasar Difference Spectra

2.3.1 Difference Spectra and Their Properties

Before construction of difference spectra using the 626 pairs of variable quasar spectra selected in Section 2.3, we shift each spectrum to the rest-frame using visually-inspected red-

shifts from Schneider et al. (2010). To ensure that the resulting difference spectra are 'positive', we subtract the spectral epoch with the lower integrated flux from the higher, with uncertainties added in quadrature. The continuum of each difference spectrum should thus be bluer than either of the individual epochs if these quasars exhibit a bluer-when-brighter trend. We visually inspect all 626 pairs of spectra along with their difference spectra, and find that the continuum of the difference spectra are well-fit by power-laws, and indeed show the bluer-when-brighter trend in the vast majority of cases. In the visual inspection, we identify 11 pairs of spectra which show evidence for strong broad absorption lines (BALs). BAL quasars are known to have atypical continuum properties (e.g., Reichard et al., 2003; Gibson et al., 2009), and the BALs are know to exhibit intrinsic variability in their absorption line strengths over long timescales (e.g., Gibson et al., 2008, 2010; Capellupo et al., 2011, 2012; Filiz Ak et al., 2012, 2013). To avoid contamination, we remove these 11 BAL quasars from our sample. We also remove 11 additional quasars identified in the visual inspection for which the variability was clearly dominated by noise. The remaining sample of 604 quasar is the sample for which all further results from our analysis are reported.

We fit the continuum of each difference spectrum to a power-law using a simple χ^2 fit, incorporating the uncertainties in the difference spectra. Although broad emission lines are well-known to be less variable than the continuum (WI05), there is still evidence of emission line variability in our difference spectra. Thus, we mask out the following wavelength regimes dominated by broad emission lines in the continuum fitting: 1360-1446Å (Si IV, O IV]), 1494-1620Å (C IV), 1830-1976Å (C III], Fe III), 2686-2913Å (Mg II), 4285-4412Å (Hγ), 4435-4762Å (Fe II), 4760-4980Å (Hβ), 4945-4972Å ([O III]), 4982-5035Å ([O III]), and 5100-5477Å (Fe II), as well as wavelengths <1300Å to avoid Ly-α emission and absorption. The choice of these masked regions are informed by the composite SDSS quasar spectrum of Vanden Berk et al. (2004); the numerous other lines and line complexes present in quasar optical spectra which we do not mask out tend to be less prominent, and we do not find evidence that these other emission lines significantly affect the continuum fitting in our visual inspections. We clip the top and bottom 1 percentile of pixels in each spectrum after applying

these mask (but before the fitting) to avoid strong outliers. After the first power-law fit, we again clip the top and bottom 1 percentile of pixels away from the best-fit power-law, before refitting the final time.

Figure 2.3 shows a few examples of pairs of quasar spectra and their difference spectra from our sample, for a range in fitted power-law spectral indices α_λ (where $F_\lambda \propto \lambda^{\alpha_\lambda}$) of the difference spectra continua. The difference spectra show excellent fits to a simple power-law, and show a strong bluer-when-brighter trend. Figure 2.4 shows the distribution of the spectral indices of the difference spectra for all 604 quasars, with and without corrections for Galactic extinction using the extinction maps of Schlegel et al. (1998) and the reddening law of Cardelli et al. (1989). To compare the difference spectra to the underlying spectra, we also calculate power-law spectral indices of the continua from the high-SN epoch in each pair of repeat quasar spectra; this provides a relatively unbiased view of the general spectral properties of each quasar. The fitting of the continua of the spectra to a power-law is performed similar to the difference spectra, but with an additional wavelength region mask of all wavelengths >5800Å to avoid contamination from host-galaxy emission (Vanden Berk et al., 2004). As expected, Figure 2.4 shows that quasar difference spectra are generally bluer than single-epoch quasar spectra, and the addition of corrections for Galactic extinction causes the continuum spectral indices to become even bluer.

2.3.2 Composite Spectrum and Difference Spectrum

We construct a geometric mean composite spectrum for both the difference spectra as well as the high-SNR single-epoch spectra of the 602 quasar in our sample with corrections for Galactic extinction; the use of a geometric mean to construct the composite spectrum preserves the arithmetic mean power-law spectral indices and extinction of a sample of power-law spectra (Reichard et al., 2003), well-suited for our investigation of quasar continuum properties. The composite spectra are created by using our power-law fits to the high-SNR epoch and difference spectra for each pair of spectra, and scaling the flux density of the fitted power-laws at 3062Å (a relatively line-free wavelength and covered by nearly all of the spectra

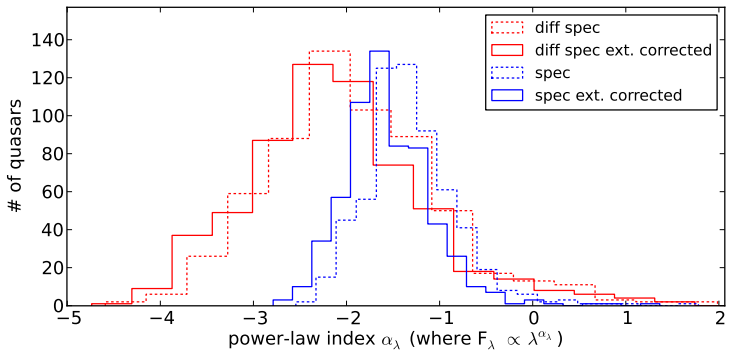

Figure 2.4: Distribution of fitted power-law spectral indicies α_λ for the high-SN epoch spectra of all variable quasars in our sample (blue dotted), and for their difference spectra (red dotted) without correcting for Galactic extinction. The distributions of the fitted indices for the same quasars after correcting for Galactic extinction are shown in solid. The median of these distributions are an excellent match to previous studies.

in our sample) to a fixed arbitrary flux density. The spectra and difference spectra themselves are then each rescaled by the same scaling factor as their fitted power-laws, and a geometric mean of all rescaled spectra and difference spectra in each wavelength bin is taken to produce the composites. The geometric mean composite spectrum and composite difference spectrum are shown in Figure 2.5. The 1σ uncertainties on the composite spectrum and difference spectrum is estimated by resampling all the pixel flux densities in each spectrum from a Gaussian with center at the measured flux density and width set to the uncertainty in the flux density. All 604 pairs of spectra are resampled 10^3 times, and 10^3 composite spectra and composite difference spectra are produced. The 1σ uncertainties shown are the 1σ spreads in these 10^3 resampled composites around the mean.

We fit the continuum of the composite spectrum and composite difference spectrum using the same broad emission line wavelength masks as before to find a power-law spectral index of $\alpha_{\lambda,comp} = -1.56 \pm 0.01$ for the composite spectrum, and $\alpha_{\lambda,diff} = -2.12 \pm 0.02$ for the composite difference spectrum. Without corrections to each spectrum for Galactic extinction

(not shown), the spectral indices are $\alpha_{\lambda,comp} = -1.38 \pm 0.01$ and $\alpha_{\lambda,diff} = -1.94 \pm 0.02$. We note that although the host-galaxy emission that dominates the composite quasar spectrum redward of ∼6000Å should not be time-variable, the composite difference spectrum seems to show some host-galaxy emission residuals. This is predominately due to noisy data and poorly-subtracted masked pixels at the red edge of the spectra, as well as the fact that the number of spectra contributing to the composite at wavelengths >6000Å is only ∼50 out of a total sample of 604. The composite difference spectrum is thus unreliable at >6000Å.

2.4 Comparison to Previous Studies

Our analysis thus far has closely followed the work of WI05, and in this section we compare our results to those from previous studies. For the composite quasar spectrum continuum, our calculated spectral index $\alpha_{\lambda,comp} = -1.56 \pm 0.01$ with corrections for Galactic extinction is an exact match to the results of Vanden Berk et al. (2004), while our $\alpha_{\lambda,comp} = -1.38 \pm 0.01$ without corrections for Galactic extinction is an excellent match to the $\alpha_{\lambda,comp} = -1.35$ calculated by WI05, all based on SDSS-I/II spectra in a similar range of wavelengths. For the composite quasar difference spectrum continuum, our calculated $\alpha_{\lambda,diff} = -1.94 \pm 0.02$ without corrections for Galactic extinction is also an excellent match to the $\alpha_{\lambda,diff} = -2.00$ from WI05. The minor discrepancy is likely due to differences in sample size, as our sample of 602 quasars is approximately a factor of two larger than the sample used in WI05 (although of course many objects are in common).

Pereyra et al. (2006) utilized the composite difference spectrum generated by WI05 and showed that it is well-fit by synthetic difference spectra generated from a thin disk model which has undergone some change in its global accretion rate. However, difference spectra are subject to both Galactic and intrinsic (host-galaxy) extinction; the composite difference spectrum of WI05 was not corrected for any extinction, and thus should not be directly compared to models. Although we have corrected each spectrum for Galactic extinction in our work, the intrinsic extinction of each quasar is much more difficult to take into account. Thus, our composite difference spectrum is subject to unknown amounts of intrinsic

extinction from each of the individual quasars in the sample.

To avoid issues with extinction and robustly compare our observed spectral variability to models, we instead consider the spectral variability *relative* to the underlying spectra of the quasars, by dividing the geometric mean composite difference spectrum by the geometric mean composite spectrum from Figure 2.5. The result, which we call the 'relative variability spectrum', is shown in Figure 2.6 and has power-law spectral index of $\Delta\alpha_\lambda \equiv \alpha_{\lambda,diff} - \alpha_{\lambda,comp} = -0.56 \pm 0.02$. The result of this division of geometric mean composite spectra is independent of any extinction with the reasonable assumption that the extinction does not significantly change between each pair of observations. We note that because broad emission lines are less variable than the continuum, the relative variability spectrum will have inverted emission lines; we have flipped the relative variability spectrum in Figure 2.6 in the vertical direction, centered on the best-fit continuum to aid in identifying continuum and emission features visually. The spectral variability of quasars relative to their underlying spectra was also investigated in WI05 using the ratio between composite difference spectra to composite spectra of their quasar sample, leading WI05 to conclude that quasars exhibited spectral variability only at wavelengths <2500Å. However, this was done by WI05 using arithmetic mean composites, which do not preserve the mean power-law indices of the spectra (making interpretation difficult), and is subject to the effects of extinction. In contrast to WI05, our relative variability spectrum avoids both these issues by using geometric mean composite spectra, facilitating robust comparison to models.

In Figure 2.6 (middle panel), we compare our observed relative variability spectrum to synthetic relative variability spectra generated from thin disk models in which the global accretion rate has increased by 5%, for a range in characteristic disk temperatures

$$T^* \equiv \left\{ \frac{3\dot{M}GM_{BH}}{8\pi r_i^3 \sigma_s} \right\}^{1/4} \tag{2.1}$$

(Frank et al., 2002). The range in T^* in Figure 2.6 (middle panel) is chosen to span the full range generated for thin disks with $\log_{10}L/L_{\rm Edd} = [-1.1, -0.8]$, and $\log_{10}M_{\rm BH} = [8.5, 9.5]$. These ranges in $\log_{10}L/L_{\rm Edd}$ and $\log_{10}M_{\rm BH}$ are representative of these values in our sample

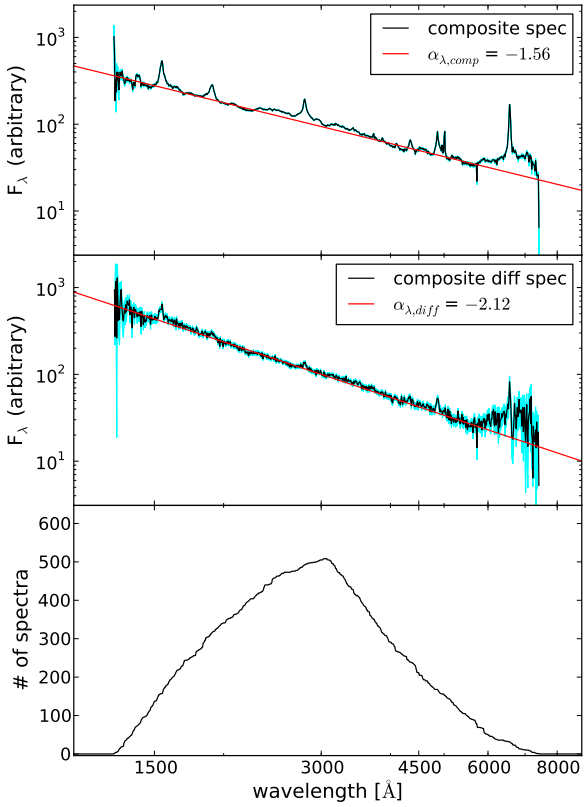

Figure 2.5: Top Panel: Geometric mean composite quasar spectrum of all high-SNR epoch spectra in our sample of 602 variable quasars, corrected for Galactic extinction, with 1σ uncertainties shown in light blue. The fitted power-law index of the continuum ($\alpha_{\lambda,comp} = -1.56$) is in excellent agreement with the composite SDSS quasar spectrum of Vanden Berk et al. (2004) for $\lambda < 5000$ Å, where host-galaxy light is minimal. Middle Panel: Geometric mean composite quasar difference spectrum for the pairs of variable quasars in our sample, corrected for Galactic extinction, also with 1σ uncertainties shown in light blue. The fitted power-law index of the continuum ($\alpha_{\lambda,diff} = -2.12$) is steeper than that of the composite spectrum, showing that the majority of quasars exhibit a bluer-when brighter trend. Bottom Panel: Number of spectra contributing to the composite spectrum and composite difference spectrum at each wavelength.

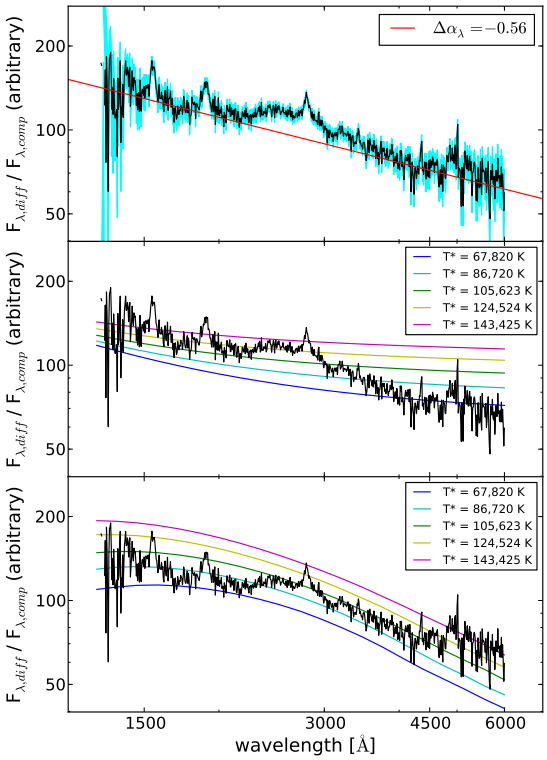

Figure 2.6: Top Panel: Observed composite relative variability spectrum, created by dividing the composite difference spectrum by the composite spectrum from Figure 2.5, with 1σ uncertainties shown in light blue. The best fit power-law to the continuum is shown (red), with relative spectral index $\Delta\alpha_\lambda \equiv \alpha_{\lambda,diff} - \alpha_{\lambda,comp} = -0.56$. We note that we have flipped this spectrum in the vertical direction around the best-fit power-law continuum (see text for details). Middle Panel: Comparison of the relative variability spectrum to that generated from changing the accretion rate in a thin disk model by 5%. The resulting synthetic relative variability spectra for a range of thin disk characteristic temperatures are shown; none are as steep as the observations, and thus do not display as strong of a bluer-when-brighter trend. Bottom Panel: Same as the middle panel, but instead comparing synthetic relative variability spectra generated from an inhomogeneous accretion disk with large temperature fluctuations. This model provides a good match to our observations in the optical.

of 604 quasars, which have median $\log_{10}L/L_{\rm Edd} = -0.89$ and median $\log_{10}M_{\rm BH} = 8.83$ $M_\odot$ from the catalog of Shen et al. (2011). From the spectral variability shown in Figure 2.6 (middle panel), it is clear that a scenario in which a thin disk changes its global accretion rate cannot account for the strong bluer-when-brighter trend observed in quasars, and it does not produce our observed power-law relative variability spectrum. Our spectral variability evidence against global accretion rate fluctuations as the cause of quasar flux variability is independently in agreement with the argument that quasar accretion disks are too large to vary coherently. We note that although we have shown in Figure 2.6 (middle panel) difference spectra of a thin disk in which the accretion rate changed by 5%, the shapes of difference spectra from thin disk models with accretion rate fluctuations are not particularly sensitive to the exact change in accretion rate (i.e. the fit will not significantly improve by increasing the change in accretion rate). Instead, the difference spectra from thin disk models depend mainly on the disk's characteristic temperature, for which we have shown a wide range in Figure 2.6 (middle panel). A similar conclusion was reached by Pereyra et al. (2006).

Aside from our results, the photometric quasar spectral variability study of SC12 also argued against global accretion rate changes as the sole driver in quasar spectral variability. We suggest that the source of the discrepancy between the conclusions of SC12 and Pereyra et al. (2006) may be due to their subtly different parameterizations of quasar spectral variability and its effects on the extinction. SC12 fitted linear relations to multi-epoch photometry of quasars in several filters in magnitude-magnitude space, and transformed the relation into color-magnitude space to investigate the variability in different filters. The spectral variability parameter that SC12 compared to models was the slope of the fit in color-magnitude space after the transformation; this slope was fit after all magnitudes for each quasar were normalized to its mean magnitudes for the different filters (see Equation 3 in SC12), and thus parameterizes the spectral variability of each quasar *relative* to its underlying color. This parameterization is similar to the power-law spectral index of the relative variability spectrum ($\Delta\alpha_\lambda$) we calculate, but for photometric colors, and is thus also independent of extinction. Although this subtlety was not discussed in SC12, this may be the source of the

conflicting results between SC12 and Pereyra et al. (2006) in comparing their observations to global accretion rate fluctuations in a thin disk.

Aside from a simple thin disk, SC12 also compared their spectral variability results to more sophisticated models presented in Davis et al. (2007), finding that their data cannot be explained by accretion rate changes in any of these disk models. SC12 suggested that ephemeral hotspots may be needed to match their observations; in the next section, we compare our observed results to one such time-dependent model of a simple inhomogeneous disk.

2.5 Disk Models with Localized Temperature Fluctuations

Dexter & Agol (2011) presented a simple analytic model of a time-dependent inhomogeneous disk, based on a thin disk radiating with independent zones undergoing temperature fluctuations and emitting locally as a blackbody. Aside from predictions of MHD turbulence in simulations of accretion disks, there is now also observational evidence for disks with time-dependent temperature fluctuations from microlensing disk-size measurements, the strong UV spectral continuum, and single-band variability characteristics. Dexter & Agol (2011) find that to satisfy these observational constrains, accretion disks must be *strongly* inhomogeneous, with large localized temperature fluctuations. These large temperature fluctuations in the disk inhomogeneities will likely cause the spectrum to be highly variable at short wavelengths, and produce distinct spectral variability with which we will compare our observations.

We set up the inhomogeneous accretion disk model of Dexter & Agol (2011), starting with a standard thin disk with an inner edge at the innermost stable circular orbit of a non-spinning black hole, and dividing its surface into n zones per factor of two in radius. The zones are roughly equally divided radially and azimuthally, although the exact setup does not noticeably affect the results in our tests. The logarithmic temperature $\log_{10}T$ in each zone independently fluctuates as a first-order continuous autoregressive (CAR(1)) process, motivated by studies of single-band variability characteristics (e.g., Kelly et al., 2009). The

mean temperature in each zone is set to the $\log_{10}T$ of the thin disk model at that radius, and the constant driving the $\log_{10}T$ fluctuations in the CAR(1) process is σ_T. The characteristic decay timescale of the temperature fluctuations is set to 200 days in the rest-frame, motivated by the observed timescales in Kelly et al. (2009) and MacLeod et al. (2010). Our spectral variability results are not sensitive to the choice of this timescale, although we note that if the decay timescale is significantly longer than the time-lag between repeat observations, the quasar will not appear to be significantly variable. All regions in the inhomogeneous disk are assumed to emit locally as a blackbody, and no relativistic effects are considered in this simple model.

We run the inhomogeneous disk model, sampling its spectrum in the wavelength range of 1300-5800Å at 50 day intervals in the rest-frame, after an initial 'burn in' time of 500 days to allow the disk to become inhomogeneous. To faithfully compare to our observations, we calculate the change in observable flux between successive time-steps by integrating the spectrum, and calculate the difference spectrum between any two successive time-steps in which the total flux changed by more than 10%, similar to the variability cut placed on the observed spectra in Figure 2.2. We run the model until we produce 5×10^3 synthetic difference spectra, and produce a synthetic geometric mean composite spectrum and composite difference spectrum, by renormalizing each spectrum in the same way as our SDSS spectra.

Figure 2.7 shows synthetic relative difference spectra generated from the inhomogeneous disk model over a range in independent zones n and temperature fluctuations σ_T, for the same disk temperatures as shown in Figure 2.6. The inhomogeneous disk produces relative variability spectra with a characteristic shape that is a power-law at optical wavelengths, which flattens at shorter wavelengths in the UV. For increasing n and σ_T in Figure 2.7, the relative variability spectra remains power-law-like further into the UV before flattening (the physical cause of this is discussed in Section 2.6.1). Thus, to produce the observed power-law spectral variability in Figure 2.6 (top panel), the inhomogeneous disk needs to have many independent zones (large n) with large temperature fluctuations (large σ_T).

An example comparison of our observed relative variability spectrum to that from the

inhomogeneous disk, using parameters $n = 10^{2.7}$ and and $\sigma_T = 0.45$, is shown in Figure 2.6 (bottom panel). The large temperature fluctuations and number of fluctuating zones required of inhomogeneous disks to provide such good fits to our observations is in excellent agreement with the $n = 10^{2.5-3}$ and $\sigma_T = 0.35 - 0.5$ range found by Dexter & Agol (2011) to simultaneously satisfy independent observational constraints from microlensing disk-size measurements, their strong UV spectral continuum, and single-band variability characteristics of quasars. This independent result based on spectral variability adds to the mounting evidence for large temperature fluctuations in strongly inhomogeneous quasar accretion disks. We note that because the relative variability spectrum is constructed from composite spectra and composite difference spectra of many quasars, each with different Eddington ratios and disk temperatures, the fit of the inhomogeneous disk relative variability spectrum is likely to improve with a more complete consideration of these variations.

2.6 Discussion

2.6.1 The Connection Between Disk Properties and Resultant Spectral Variability

Our success of modeling quasar spectral variability in the previous section can be understood as the result of the confluence of large temperature fluctuations in a strongly inhomogeneous disk emitting locally as a blackbody. A flare in a portion of the disk causes the variable part of its optical spectrum to be due to the blackbody emission from the flaring region. For very high-temperature flares, the blackbody spectrum of the flaring region peaks well into the UV, and thus the difference spectrum is dominated by its power-law Rayleigh-Jeans tail. This is the cause of the trend in Figure 2.7 where the power-law portion of the model relative variability spectrum increasingly extends into the UV as σ_T increases. We note that for small σ_T, the turnover in the UV is a flattening rather than a sharp peak because it is the superposition of the blackbody peaks of numerous flaring regions.

Aside from the large temperature fluctuations, the disk must also be strongly inhomogeneous, with a large number of independently fluctuating regions (i.e. a disk with large n).

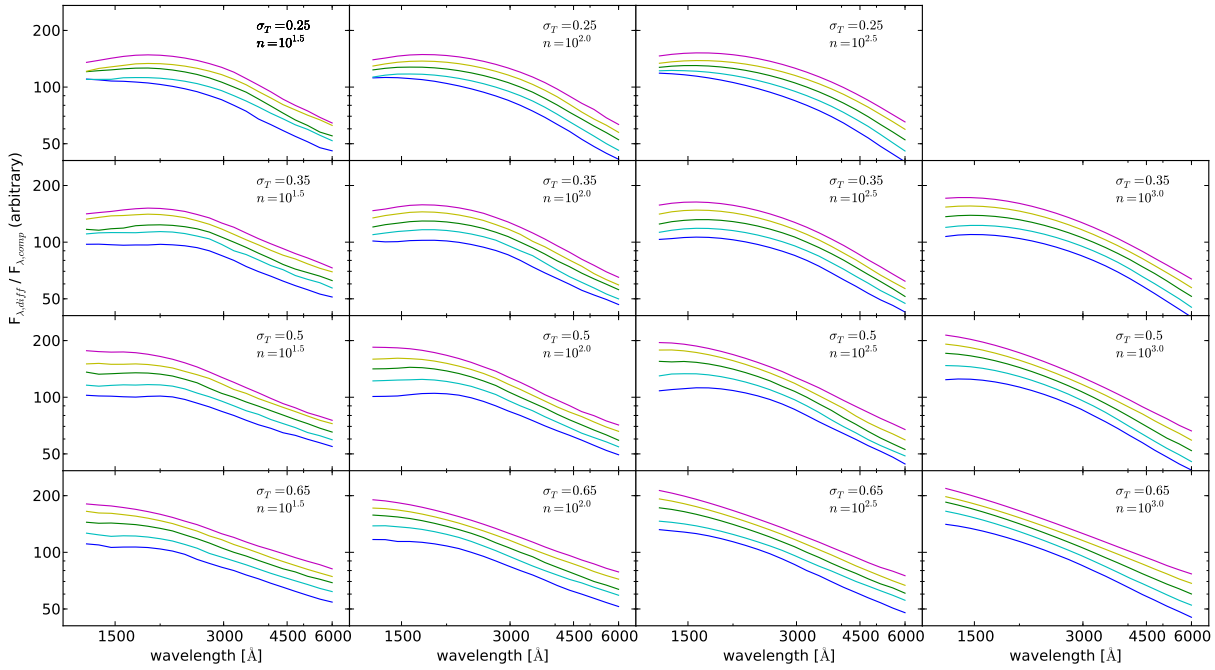

Figure 2.7: Synthetic relative variability spectra generated form the inhomogeneous disk over disk parameters σ_T and n (see Section 2.5 for details). The range in disk temperatures shown for each panel is the same as in Figure 2.6 (middle panel). These synthetic relative variability spectra are power-laws in the optical, with a flattening in the UV. The turnover occurs further into the UV with both increasing σ_T and n (see Section 2.6.1 for discussion). Note that we do not show results for larger n and smaller σ_T because disks with these parameters are not variable enough in flux to produce difference spectra that pass our 10% flux change cut.

This is due to the fact that the total flux variability amplitude of the disk scales as N^{-1}, where N is number of independently varying zones (Dexter & Agol, 2011); as n increases and the disk becomes more strongly inhomogeneous, the total flux variability decreases. In the case of a disk with small n, the difference spectra will be dominated by smaller, lower-temperature flares with blackbody peaks in the optical rather than the UV, and thus the spectral variability will not be dominated by the Rayleigh-Jeans spectrum. Conversely, for

large n, the disk does not exhibit strong overall flux variability, and only very large, high-temperature flares are actually observable. Thus, the observed flux variability in strongly inhomogeneous disks will be dominated by the Rayleigh-Jeans spectrum, naturally producing power-law spectral variability. This effect causes the power-law portion of the model relative variability spectrum in Figure 2.7 to extend further into the UV with increasing n. We emphasize that this line of evidence for large temperature fluctuations in strongly inhomogeneous disks is independently in excellent agreement with other observational constraints from microlensing disk sizes, their strong UV spectral continuum, and single-band variability properties.

We note that because the temperatures in each independently fluctuating zone is damped in the CAR(1) process and thus cannot increase infinitely, the inhomogeneous disk predicts a flattening in the relative variability spectrum in the UV (e.g. as seen in Figure 2.7). This flattening is not seen in our difference spectra, which appears to be well-fit by a power-law down to $\sim$1300Å, although the SNR decreases dramatically below $\sim$1500Å. Broadband studies of quasar UV variability have shown that quasars are indeed generally more variable in the UV than optical (Gezari et al., 2013). However, a more careful investigation of quasar spectral variability from optical to the UV will require contemporaneous optical-UV observations, and will be a fruitful test of the inhomogeneous disk model. We also note that in the simple inhomogeneous disk model of Dexter & Agol (2011), the global accretion rate is assumed to be constant. This may not be entirely justified, as processes causing the large temperature fluctuations such as the MRI are likely to also induce fluctuations in the accretion rate (e.g. by causing the viscosity to change locally). Although we have ruled out accretion rate fluctuations as the sole driver of quasar spectral variability in Section 2.4, the observed difference spectra in Figure 2.5 (middle panel) may still be affected by changes in the accretion rate. In particular, because Figure 2.6 (middle panel) shows that accretion rate changes produce spectral variability that is particularly strong in the UV, the addition of accretion rate changes to the inhomogeneous disk model may cause difference spectra to become power-law like well into the far UV, further improving the match to the observed

UV spectral variability.

2.6.2 Other Possibilities for Difference Spectra

The disk models we have considered all assume that the disk emits locally as a blackbody; while this may be a good approximation for the underlying disk spectrum, it is not entirely justified for difference spectra, which instead isolate the variable part of the spectrum. It is possible that the observed power-law difference spectrum is instead at least partially due to non-thermal emission, which could dominate the variable portion of quasar optical/UV spectra. For example, disk inhomogeneities from the photon bubble instability in the magnetized atmosphere of a radiation pressure-dominated disk (Arons, 1992; Gammie, 1998; Turner et al., 2005) may cause the spectrum during flaring epochs to become non-thermal, due the shorter paths in the low gas-density bubbles for photons to diffuse to the photosphere (Gammie, 1998), or due to an increase in free-free emission in the high photon-density bubbles (Davis et al., 2009). Radio-loud quasars have long been suspected to harbor weak or unresolved jets, and the highly-variable jet synchrotron emission can also produce power-law difference spectra in the optical/UV. Future observations of quasar spectral variability across multiple wavelength regimes contemporaneously can help constrain these possibilities.

2.6.3 Variability Correlations with M_{BH} and Luminosity

Finally, we note that our findings that quasar spectral variability cannot be driven purely by global accretion rate changes in a thin disk is not at odds with the trends between variability amplitude, black hole mass, and luminosity that many studies have found, and which suggest that the Eddington ratio may be driving these trends. It is still possible that differences in the mean Eddington ratio among different quasars drive their variability properties, a conclusion also reached by SC12. Notably, MacLeod et al. (2010) also found that the scaling relation between these quantities is much shallower than that predicted from the Eddington ratio, suggesting additional physics may be necessary to explain the observed trend. Modeling of these trends using inhomogeneous disk models awaits future investigation.

2.7 Conclusions

The characteristic flux variability of quasars reflects complex processes in the accretion disk, yet the cause of the variability is still unknown. Aside from single-band variability characteristics, the spectral variability of quasars provides an additional, independent constraint on models of the variability mechanism. Using repeat spectra of quasars in SDSS-I/II, we investigate the optical spectral variability of quasars, which are known to show a bluer-when-brighter trend. After a wavelength-dependent spectrophotometric recalibration of the quasar spectra using non-variable stars observed on the same plates, we construct difference spectra of 602 variable quasars in our sample, thus isolating the variable part of the spectrum. We compare our observations to synthetic difference spectra generated from a thin disk model in which the accretion rate has varied, as well as a simple inhomogeneous disk model with localized temperature fluctuations. In particular, we find the following:

1. Quasar difference spectra appear to be power-laws with spectral indices steeper than their single-epoch spectra, indicating that the vast majority of quasars show a bluer-when-brighter trend. We measure quasar spectral variability using the relative variability spectrum, which is independent of any extinction. We find that accretion rate fluctuations in a thin disk model cannot produce the strong bluer-when-brighter trend observed. This is contrary to the results of some previous investigations, and may be due to the effects of intrinsic and Galactic extinction that were not accounted for in those previous studies.

2. A time-dependent inhomogeneous disk model can produce spectral variability that provides a good match to our observations over optical wavelengths if the disk is strongly inhomogeneous, with large temperature fluctuations. The difference spectra produced by such inhomogeneous disks are dominated by the Rayleigh-Jeans spectrum from the hot 'flaring' regions in the optical, and are thus naturally power-laws. The large temperature fluctuations and large number of zones in the disk required to match our

observed spectral variability is in excellent agreement with independent observational constraints from quasar microlensing disk-sizes, their strong UV spectral continuum, and single-band flux variability characteristics.

Our spectral variability constraints suggests that future quasar disk models should be time-dependent, and include large temperature fluctuations. Improved global GRMHD simulations of radiative disks will help inform more sophisticated inhomogeneous disk models to compare to observations. Observationally, future time-domain photometric and spectroscopic observations from the Large Synoptic Survey Telescope (Ivezic et al., 2008) and the Time-Domain Spectroscopic Survey portion of SDSS-IV will help better constrain these models.

2.8 Acknowledgements

JJR thanks Yusra AlSayyad and James R. A. Davenport for helpful discussions about processing SDSS spectra. Support for JJR was provided by NASA through Chandra Award Numbers AR9-0015X, AR0-11014X, and AR2-13007X, issued by the Chandra X-ray Observatory Center, which is operated by the Smithsonian Astrophysical Observatory for and on behalf of NASA under contract NAS8-03060. Support for EA was provided by NASA through a grant from the Space Telescope Science Institute, which is operated by the Association of Universities for Research in Astronomy, Inc., under NASA contract NAS 5-26555

Funding for the SDSS and SDSS-II has been provided by the Alfred P. Sloan Foundation, the Participating Institutions, the National Science Foundation, the U.S. Department of Energy, the National Aeronautics and Space Administration, the Japanese Monbukagakusho, the Max Planck Society, and the Higher Education Funding Council for England. The SDSS Web Site is http://www.sdss.org/.

The SDSS is managed by the Astrophysical Research Consortium for the Participating Institutions. The Participating Institutions are the American Museum of Natural History, Astrophysical Institute Potsdam, University of Basel, University of Cambridge, Case Western

Reserve University, University of Chicago, Drexel University, Fermilab, the Institute for Advanced Study, the Japan Participation Group, Johns Hopkins University, the Joint Institute for Nuclear Astrophysics, the Kavli Institute for Particle Astrophysics and Cosmology, the Korean Scientist Group, the Chinese Academy of Sciences (LAMOST), Los Alamos National Laboratory, the Max-Planck-Institute for Astronomy (MPIA), the Max-Planck-Institute for Astrophysics (MPA), New Mexico State University, Ohio State University, University of Pittsburgh, University of Portsmouth, Princeton University, the United States Naval Observatory, and the University of Washington.

Chapter 3

THE NATURE OF TRANSITION BLAZARS

Blazars are AGN with relativistic jets aligned along the line of sight, and are amongst the most persistently variable sources in the sky due to relativistic effects. Blazars are classically divided into the BL Lac (BLL) and Flat-Spectrum Radio Quasar (FSRQ) subclasses, corresponding to radiatively inefficient and efficient accretion regimes, respectively, largely based on the equivalent width (EW) of their optical broad emission lines (BEL). However, EW-based classification criteria are not physically motivated, and a few blazars have previously 'transitioned' from one subclass to the other. In this chapter, I present the first systematic search for these transition blazars in a sample of 602 unique pairs of repeat spectra of 354 blazars in SDSS, finding six clear cases. These transition blazars have bolometric Eddington ratios of $\sim$0.3 and low-frequency synchrotron peaks, and are thus FSRQ-like. I show that the strong EW variability (up to an unprecedented factor of $>$60) is due to swamping of the BELs from variability in jet continuum emission, which is stronger in amplitude and shorter in timescale than typical blazars. Although these transition blazars appear to switch between FSRQ and BLL according to the phenomenologically-based EW scheme, I show that they are most likely rare cases of FSRQs with radiatively efficient accretion flows and especially strongly-beamed jets. These results have implications for the decrease of the apparent BLL population at high-redshifts, and may add credence to claims of a negative BLL redshift evolution.

Material from this chapter was previously published in collaboration with Scott F. Anderson, Richard R. Plotkin, William N. Brandt, Toby H. Burnett, Adan D. Myers, and Donald P. Schneider in the December 2014 edition of the Astrophysical Journal (Ruan et al., 2014b), and has been reproduced here with permission of the American Astronomical Society.

3.1 Introduction

Blazars are a relatively rare class of Active Galactic Nuclei (AGN) in which a jet is aligned closely along the observed line of sight (Blandford & Rees, 1978). These jets are relativistically beamed, leading to unique multi-wavelength properties from the radio through the γ-rays (Antonucci, 1993; Urry & Padovani, 1995). Classically, blazars have been divided into the Flat-Spectrum Radio Quasar (FSRQ) and BL Lac (BLL) subclasses based on whether any optical broad emission lines (BELs) have rest-frame equivalent widths (EWs) above (in the case of FSRQs) or below (in the case of BLLs) 5Å (e.g. Stickel et al., 1991; Stocke et al., 1991; Perlman et al., 1996; Plotkin et al., 2010). These two subclasses of blazars also show systematic differences in Eddington ratios (Dai et al., 2007), γ-ray properties (Ackermann et al., 2011), and the luminosities and frequencies of their synchrotron and inverse-Compton peaks of their spectral energy distributions (Padovani & Giommi, 1995; Sambruna et al., 1996; Fossati et al., 1998; Abdo et al., 2010a), amongst many other differences.

The physical distinction between FSRQs and BLLs is suspected to stem from the divergent natures of their underlying accretion flows around the central supermassive black holes (Maraschi & Tavecchio, 2003; Ghisellini & Tavecchio, 2008). FSRQs are believed to harbor geometrically-thin, optically-thick accretion disks that are accreting rapidly, with Eddington ratios $\gtrsim$0.1, similar to (and perhaps systematically higher than) typical Type 1 quasars (Shaw et al., 2012). The existence of broad emission lines in their optical spectra from high-velocity gas clouds, as well as strong emission in the infrared from dusty torii, are well-described by the standard radio-loud unification scheme of AGNs (Urry & Padovani, 1995). In contrast, BLLs are thought to have geometrically-thick, optically-thin accretion disks (at least in their inner regions), where the accretion is radiatively inefficient (Narayan & Yi, 1994), with Eddington ratios generally $\lesssim$0.01 (Wang et al., 2002; Davis et al., 2007). Their lack of broad emission lines and dust emission suggests that the properties of accretion flow and structure of the surrounding gas in BLLs are physically different from FSRQs.

The classical EW-based classification of blazars between FSRQs and BLLs is not physi-

cally motivated, and a handful of blazars have been previously reported to transition between these two classes in repeat spectroscopic observations due to variability in their BEL EWs (e.g., Ghisellini et al., 2011; Shaw et al., 2012). These rare 'transition' blazars ironically include the namesake BL Lacertae object, in which the rest-frame Hα EW has been reported to vary between approximately 0 to $\sim$7Å (Vermeulen et al., 1995; Corbett et al., 1996). Analysis of long-term spectroscopic monitoring of BL Lacertae by Corbett et al. (2000) demonstrated that this variability in the BEL EW is anti-correlated with the continuum luminosity, suggesting that the strongly-variable jet continuum emission is swamping the BEL flux, leading to the transition blazar phenomena. More recent reports of *Fermi*-detected transition blazars by Shaw et al. (2012) have provided observational motivation for investigations into the mysterious nature of these objects (see also Isler et al., 2013). Ghisellini et al. (2011) showed that many *Fermi*-detected BLLs with γ-ray properties similar to FSRQs also have SEDs and BEL luminosities that are FSRQ-like, thus suggesting that some BL Lacs may actually be FSRQs with particularly strong jet continuum emission. Based on their findings, Ghisellini et al. (2011) also suggested an improved classification scheme based on the Eddington ratio calculated from the BEL luminosities; this approach is more physically-motivated and particularly helpful for transition blazars (also see Giommi et al., 2012; Sbarrato et al., 2012).

Correct classification of transition blazars is critical not only for studies of the different properties of FSRQs and BLLs (e.g., along the 'blazar sequence', Fossati et al., 1998), but also has important implications for their redshift evolution. For example, BLLs are more commonly found at lower redshifts, leading to many reports of apparent negative redshift evolution (Maccacaro et al., 1984; Wolter et al., 1994; Rector et al., 2000; Beckmann et al., 2003), although this interpretation has been often disputed (Caccianiga et al., 2002; Padovani et al., 2007; Marchã & Caccianiga, 2013). Misclassifications of blazars can artificially lead to an apparent lack of high-redshift BLLs, significantly affecting evolutionary scenarios of the blazar sequence (e.g., Böttcher & Dermer, 2002) and the blazar contributions to the cosmic γ-ray background (e.g., Abdo et al., 2010b). These issues of correct classification

face the further challenge of obtaining correct redshifts from the often featureless spectra of blazars; strong BEL EW variability in transition blazars can be used to determine or constrain redshifts in repeat spectra during epochs in which the EWs are large (Shaw et al., 2013b).

In this paper, we present the first systematic search for transition blazars in a large sample of repeat spectra of known blazars in the Sloan Digital Sky Survey (SDSS, York et al., 2000). Many previous reports of transition blazars have been based on comparison to EW classifications in the literature; the homogeneous nature of SDSS spectra will allow a more robust measurement of their variable spectral properties over timescales of over a decade in the observed frame. To complement the repeat optical spectra in our study, we also adopt a multi-wavelength approach to investigate the γ-ray, optical variability, and SED properties of these rare objects, tying our findings to the many recent investigations of blazar properties in these domains.

The outline of this chapter is as follows. In Section 3.2, we present our sample of repeat blazar spectra and spectral analysis to identify transition blazars. In Section 3.3, we discuss the spectral and multi-wavelength properties of the transition blazars in our sample. In Section 3.4, we comment on the individual transition blazars in our sample. In Section 3.5, we discuss the nature of these transition blazars based on their properties. We summarize and conclude in Section 3.6. Throughout the paper, EW refers to the equivalent width calculated in the rest-frame. We assume a standard ΛCDM cosmology with $\Omega_M = 0.3$, $\Omega_\Lambda = 0.7$, and $H_0 = 70$ km s^{-1} Mpc^{-1}, consistent with the WMAP 9-year results of Hinshaw et al. (2013).

3.2 Data and Search for Transition Blazars

3.2.1 Analysis of SDSS Spectra

Our data are taken from the SDSS-III (Gunn et al., 2006; Eisenstein et al., 2011) Data Release 10 (DR10, Ahn et al., 2014), which is publicly available and also includes all data from the

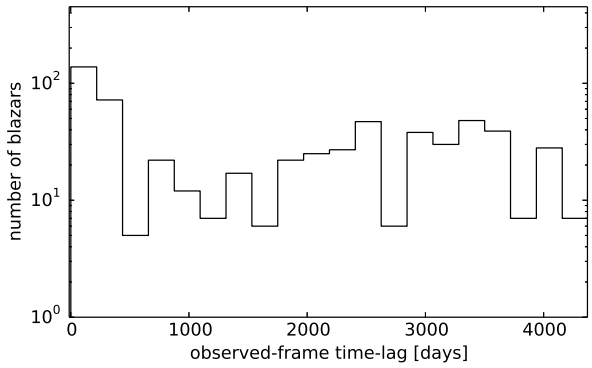

Figure 3.1: Histogram of the observed-frame time-lags between each pair of repeat blazar spectra in our sample of 602 unique pairs. The median redshift of blazars with measured redshifts is 1.05, although this value is strongly biased towards FSRQs, which have systematically higher redshifts than BL Lacs.

SDSS-I/II portions of the survey. DR10 includes $\sim 4\times10^6$ optical spectra over approximately 14,000 deg^2 of sky, including $\sim 1.6\times10^5$ quasars (Pâris et al., 2014), selected primarily from the imaging portion of the survey in a variety of science programs (Ross et al., 2012). In our investigation, we include all optical spectra taken from the primary survey portion of SDSS-I/II on the SDSS spectrograph, as well as spectra from the BOSS spectrograph used in SDSS-III (spectral resolution $R \sim 2000$). Due to differences between the spectrographs, fiber system, and spectral reduction pipeline between these phases of the SDSS survey (see Bolton et al., 2012; Smee et al., 2013), some small differences in absolute flux calibration may be present in spectra taken at different epochs (Dawson et al., 2013). These differences do not strongly affect our results, which are primarily based on spectral properties which are normalized to the continuum (e.g. equivalent widths).

Occasionally, repeat spectra of the same objects in SDSS were taken, either due to low signal-to-noise ratios in the first epoch, or as part of the survey plan. To create a sample of known blazars with repeat spectra in SDSS-III, we match all objects with repeat spectra

available in DR10 to the 3,149 blazars in the ROMA-BZCAT[1] catalog of Massaro et al. (2009). This comparison results in a sample of 354 blazars with repeat observations, including a few with more than two epochs. Since the classical EW-based classification is based on whether any BELs in the observed optical spectrum are above or below 5Å, we will compare the BEL EWs in pairs of repeat spectra of each blazar to identify cases where the BEL crossed this EW threshold. For blazars with more than two epochs of spectra, we will compare all unique pairs, leading to a total of 602 unique pairs of repeat spectra of the 354 blazars. Blazars are known to be highly variable even in intra-night observations, and the timescales on which blazars can transition between the FSRQ and BLL subclasses is not known; we thus place no cuts on the time-lag between repeat observations for our sample, which range from intra-night to approximately 12.5 years in the observed frame. The distribution of time-lags for our sample is shown in Figure 3.1.

We correct all repeat blazar spectra in our sample for Galactic extinction, using the maps of Schlegel et al. (1998) and the Milky Way reddening law of Cardelli et al. (1989). We also shift the repeat spectra of each blazar into the rest-frame using redshifts provided by the ROMA-BZCAT catalog, cognizant of the fact that the redshifts of many blazars in this catalog are missing, uncertain, or occasionally incorrect. To ensure that these redshifts we use are not obviously incorrect, we visually inspect all 602 unique pairs of repeat blazar spectra in our sample. In the visual inspection, we mask pixels in each spectrum with SDSS flags set for NOPLUG, BADTRACE, BADFLAG, BADARC, MANYBADCOLUMNS, MANYREJECTED, NEARBADPIXEL, LOWFLAT, FULLREJECT, SCATTEREDLIGHT, NOSKY, BRIGHTSKY, COMBINEREJ, REDMONSTER (for details on these flags, see Stoughton et al., 2002). Due to this spectrum quality mask, 16 of the 602 unique pairs of repeat blazar spectra in our sample were removed.

As expected, the visual inspection reveals that the overwhelming majority of blazars appear to have spectra that are either featureless (canonical BLLs) or have moderately-strong

[1]http://www.asdc.asi.it/bzcat/

BELs (canonical FSRQs). Some outliers include BLLs that possessed strong host-galaxy contributions (e.g., misaligned BLLs), blazars with intrinsic and line-of-sight absorption features, as well as a small handful in which the emission lines strongly varied in EW between the different spectral epochs. To quantitatively identify blazars which have transitioned from FSRQs to BLLs (or vice versa) in our sample, we measure the properties of the C IV λ1546, C III] λ1906, Mg II λ2800, and Hα λ6565 broad emission lines (in vacuum wavelengths), where possible.

Table 3.1. SDSS spectral properties of all broad emission lines present in each of the transition blazars in our sample.

SDSS Object	z	Emission Line	MJD	EW [Å]	$\log_{10}L_{\rm line}$ [erg s^{-1}]	FWHM [km s^{-1}]	$\log_{10}M_{\rm BH}$ [M$_\odot$]	$\log_{10}(L_{\rm bol}/L_{\rm Edd})$	$\log_{10}(L_{\rm BLR}/L_{\rm Edd})$
J083223.22+491321.0[a]	0.548[b]	Mg II	51873	0.9 ± 0.7	41.52 ± 0.02				
			55277	1.3 ± 0.3	41.47 ± 0.01				
			55290	2.3 ± 0.5	41.59 ± 0.01	2126 ± 332	6.84 ± 0.15	-0.76 ± 0.23	-2.14 ± 0.15
J083353.88+422401.8	0.249[c]	Hα	52266	5.1 ± 0.6	41.63 ± 0.05	809 ± 228	6.33 ± 0.26	0.18 ± 0.48	-1.94 ± 0.26
			54524	4.8 ± 0.8	41.71 ± 0.07				
			55924	2.1 ± 0.3	41.68 ± 0.06				
J101603.13+051302.3	1.714[c]	C IV	52347	1.8 ± 0.2	43.12 ± 0.04				
			52355	14.8 ± 0.4	43.91 ± 0.01				
			52356	43.4 ± 1.6	43.94 ± 0.01				
			52366	19.56 ± 5.3	43.70 ± 0.09				
			55653	116.8 ± 4.3	43.76 ± 0.01	3267 ± 50	8.44 ± 0.22	-0.54 ± 0.61	-1.83 ± 0.22
		C III]	52347	1.0 ± 0.1	42.75 ± 0.05				
			52355	4.0 ± 0.4	42.26 ± 0.04				
			52356	3.3 ± 0.4	42.83 ± 0.04				
			52366	10.8 ± 0.8	43.33 ± 0.03				

3.2.2 BEL Fitting and the Transition Blazar Sample

The details of our BEL fitting closely follow Shen et al. (2011, hereafter SH11), to allow for comparison of the BEL properties of our transition blazars to the general SDSS quasar population. The primary difference in our fitting in comparison to SH11 is that we opt not to fit templates for Fe emission since the continuua in transition blazars are strongly dominated by jet emission, and thus the Fe line complexes are not well-detected in their spectra. For C IV, Mg II, and Hα, we fit a power-law to the continuum wavelength windows used by SH11; the flux densities in the BEL wavelength windows (also the same as in SH11) are then normalized by the fitted continuum and integrated to find the EW. For C III], which was not analyzed in SH11, we use continuum windows of 1810-1830Å and 1976-1996Å, and the BEL window is 1830-1976Å. The choice of these wavelength windows for C III] is informed by the SDSS composite quasar spectrum of Vanden Berk et al. (2001).

For each BEL, we fit both a broad and narrow component, each using a Gaussian with the same line center fixed to their lab vacuum wavelengths. However, the higher-ionization C IV line is well-known to exhibit intrinsic blueshifts (Gaskell, 1982; Richards et al., 2002b, 2011), and so we allow the line center (assumed to be the same for both broad and narrow components) to be a single free parameter. The FWHM of the narrow component is constrained to be $<$1200 km s^{-1}, and the amplitudes of all components are constrained to be positive. For Hα, we fit additional Gaussians for the narrow [N II] $\lambda\lambda$6548, 6584 lines, as well as [S II] $\lambda\lambda$6717, 6731. We visually inspect the fit of each emission line and continuum region to ensure that it was not strongly affected by problematic pixels or absorption features. The statistical uncertainties on all quantities derived from the fitting (notably the EWs, luminosities, and FWHMs) are estimated by simulating the noise in each spectrum, by resampling each pixel from a Gaussian distribution with σ set to the uncertainty in the pixel flux density. All pixels in each spectrum are resampled in this fashion and refitted with the above procedure 10^3 times; the uncertainties on the fitted quantities are then based on their 1σ range in the simulated spectra. Several studies have indicated a likely dependence

Table 3.1 (cont'd)

SDSS Object	z	Emission Line	MJD	EW [Å]	$\log_{10}L_{\rm line}$ [erg s^{-1}]	FWHM [km s^{-1}]	$\log_{10}M_{\rm BH}$ [M$_\odot$]	$\log_{10}(L_{\rm bol}/L_{\rm Edd})$	$\log_{10}(L_{\rm BLR}/L_{\rm Edd})$
			55653	55.2 ± 3.0	43.32 ± 0.02				
		Mg II	52347	1.7 ± 0.1	42.85 ± 0.03				
			52355	5.3 ± 0.3	43.30 ± 0.02				
			52356	15.8 ± 1.7	43.39 ± 0.05				
			52366	8.6 ± 0.6	43.16 ± 0.03				
			55653	72.9 ± 4.6	43.37 ± 0.03	2739 ± 224	8.18 ± 0.10	-0.30 ± 0.20	-1.70 ± 0.10
J125032.57+021632.1	0.959[b]	Mg II	52024	3.6 ± 0.4	42.29 ± 0.05				
			55631	8.2 ± 0.2	42.54 ± 0.01	4360 ± 213	8.06 ± 0.08	-1.01 ± 0.19	-2.41 ± 0.08
J130823.70+354637.0	1.055[c]	Mg II	55335	8.5 ± 1.2	42.46 ± 0.06	2250 ± 718	7.43 ± 0.29	-0.46 ± 0.34	-1.86 ± 0.30
			55597	4.9 ± 0.7	42.74 ± 0.06				
J143758.67+300207.1	1.230[b]	Mg II	53757	0.4 ± 0.2	42.14 ± 0.02				
			55277	25.6 ± 0.5	42.76 ± 0.01	3829 ± 281	8.08 ± 0.09	-0.81 ± 0.19	-2.21 ± 0.09
J220643.28-003102.5	1.051[d]	Mg II	52937	9.9 ± 1.5	42.81 ± 0.06	4189 ± 1683	8.19 ± 0.36	-0.87 ± 0.40	-2.27 ± 0.36
			55481	4.9 ± 0.8	42.61 ± 0.07				

[a] This blazar did not transition, but is likely to be a transition blazar (see Section 3.4). [b] New redshift. [c] Redshift from Massaro et al. (2009). [d] Redshift from Shaw et al. (2013a).

of quasar BEL FWHMs on orientation (Wills & Browne, 1986; Jarvis & McLure, 2006; Fine et al., 2011; Runnoe et al., 2013), which may bias our FWHM measurements and black hole mass estimates due to the strong jet-alignment of blazars. However, this bias cannot be significantly larger than the $\lesssim$0.2 dex dispersion in the log-normal distribution of BEL FWHMs of quasars (Shen et al., 2008), and thus cannot account for the 1-2 dex difference in the Eddington ratio between our transition blazars (see Section 3.3.1) and that typical of radiatively inefficient accretion.

We identify six blazars for which any BEL in the spectrum crossed the 5Å EW threshold in the rest-frame, transitioning between the canonical BLL and FSRQ classifications (or vice versa). The properties of these transition blazars are listed in Table 3.1 (and discussed in Section 3.3), and Figures 3.2 to 3.7 show their multi-epoch spectra, the fitting of the continuum-normalized BEL region in each of the epochs, as well as their long-term photometric light curves (discussed in Section 3.3.4). The observed changes in the EW in the six blazars across the 5Å threshold vary wildly, up to a factor of >60 for SDSS J101603.13+051302.3. Due to the small sample size, we will not attempt to investigate the incidence of these blazar subclass transitions in our current study, and instead focus on understanding the nature of this phenomenon.

Since transition blazars intermittently show small BEL EWs by definition, redshifts can be difficult to obtain from spectra. Indeed, for two of these transition blazars as well as one additional blazar (SDSS J083223.22+491321.0) which did not transition, no previous redshifts have been reported. We report new secure redshifts from the SDSS pipeline using the spectral epochs where the BELs have the largest EWs (are thus most well-detected). Although SDSS J083223.22+491321.0 did not transition, we nevertheless show its spectra and BEL fits in Figure 3.2 due to its newly-determined redshift and its special implications for transition blazars (discussed in Section 3.5). We discuss the properties of each of these individual blazars in more detail in Section 3.4.

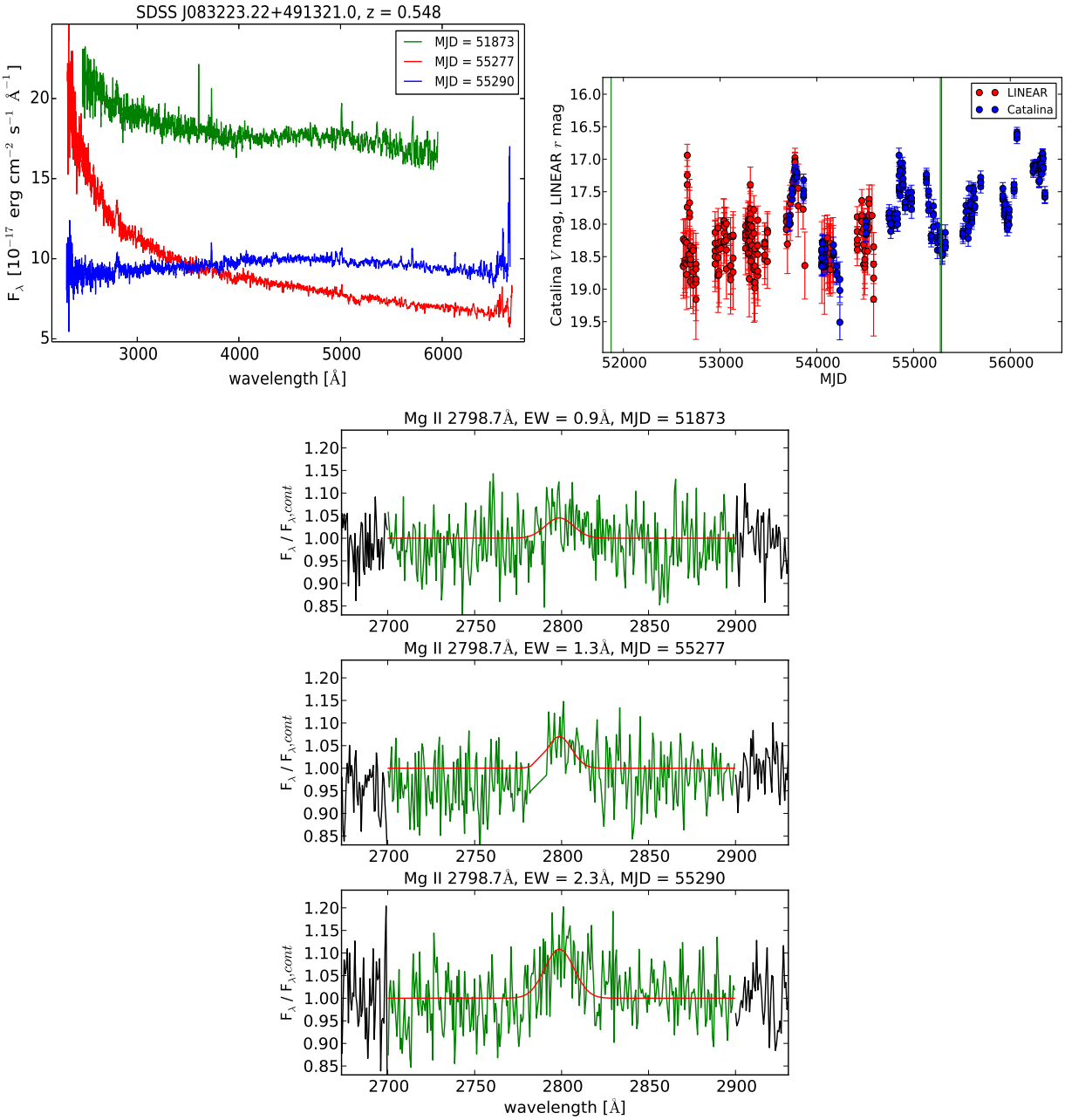

Figure 3.2: SDSS J083223.22+491321.0: multi-epoch observed-frame SDSS spectra, rest-frame broad emission line fitting, and photometric light curve. The dates of the spectroscopic epochs are indicated by the green lines in the light curve.

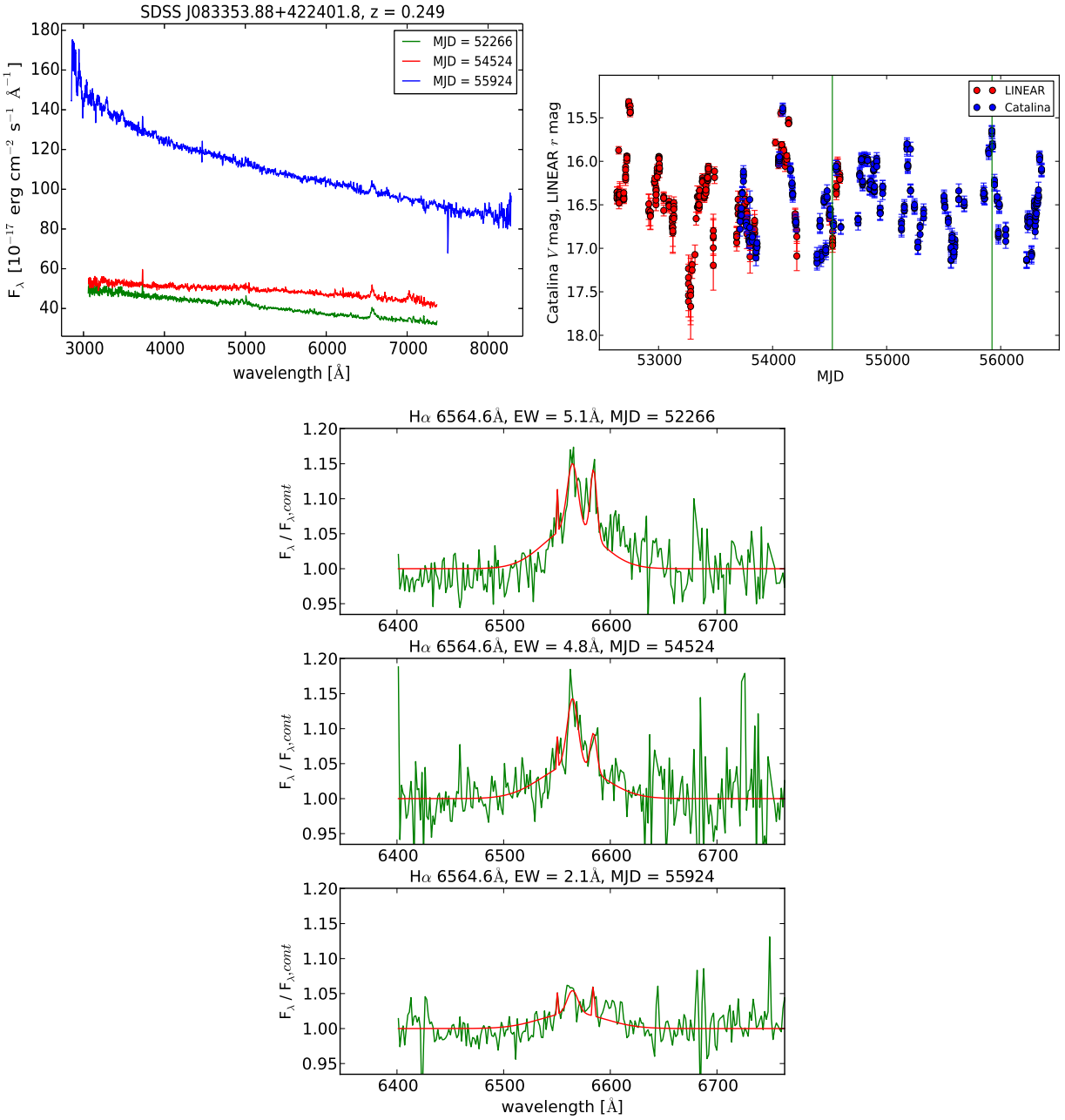

Figure 3.3: SDSS J083353.88+42241.8, similar to Figure 3.2.

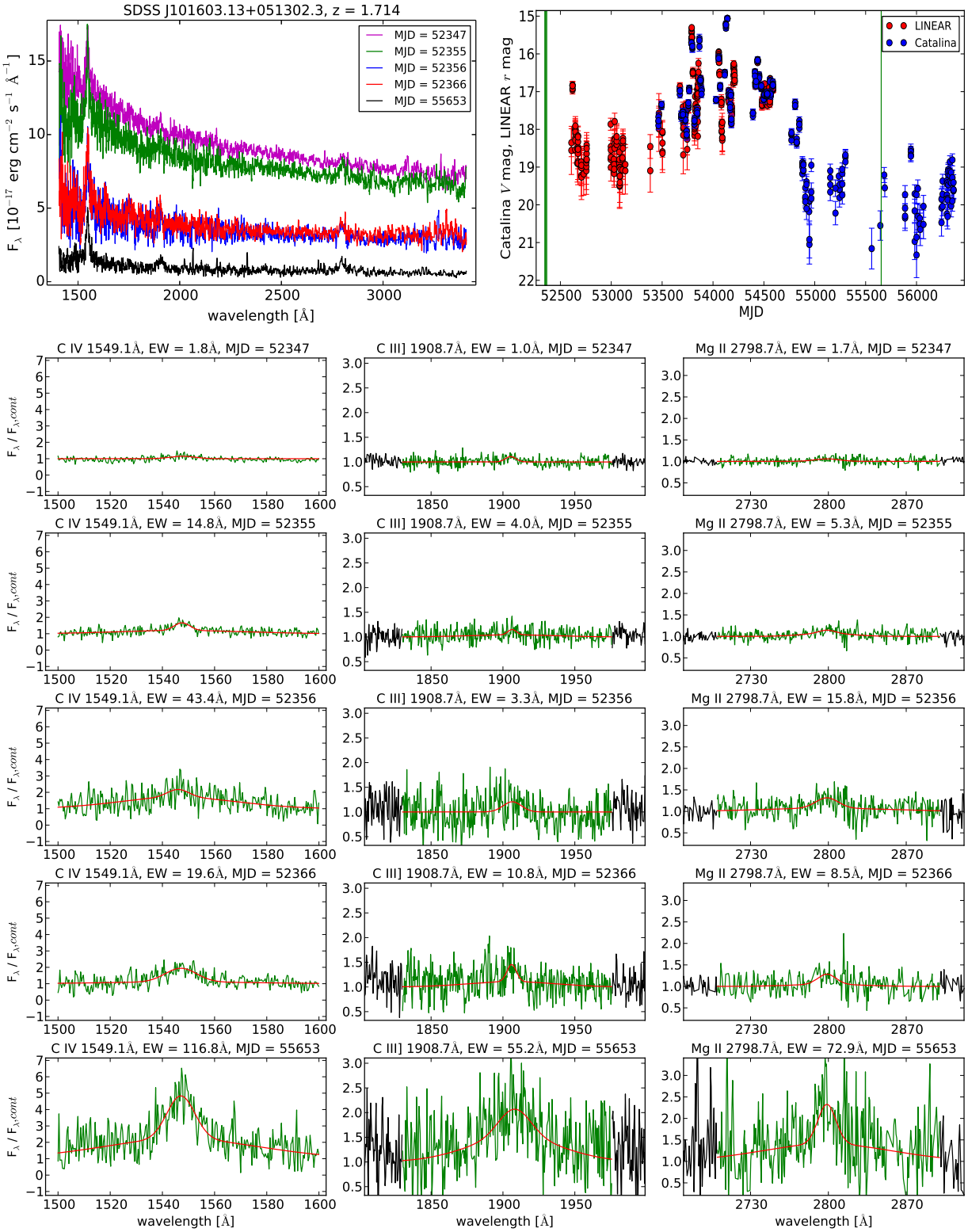

Figure 3.4: SDSS J10163.13+05132.3, similar to Figure 3.2.

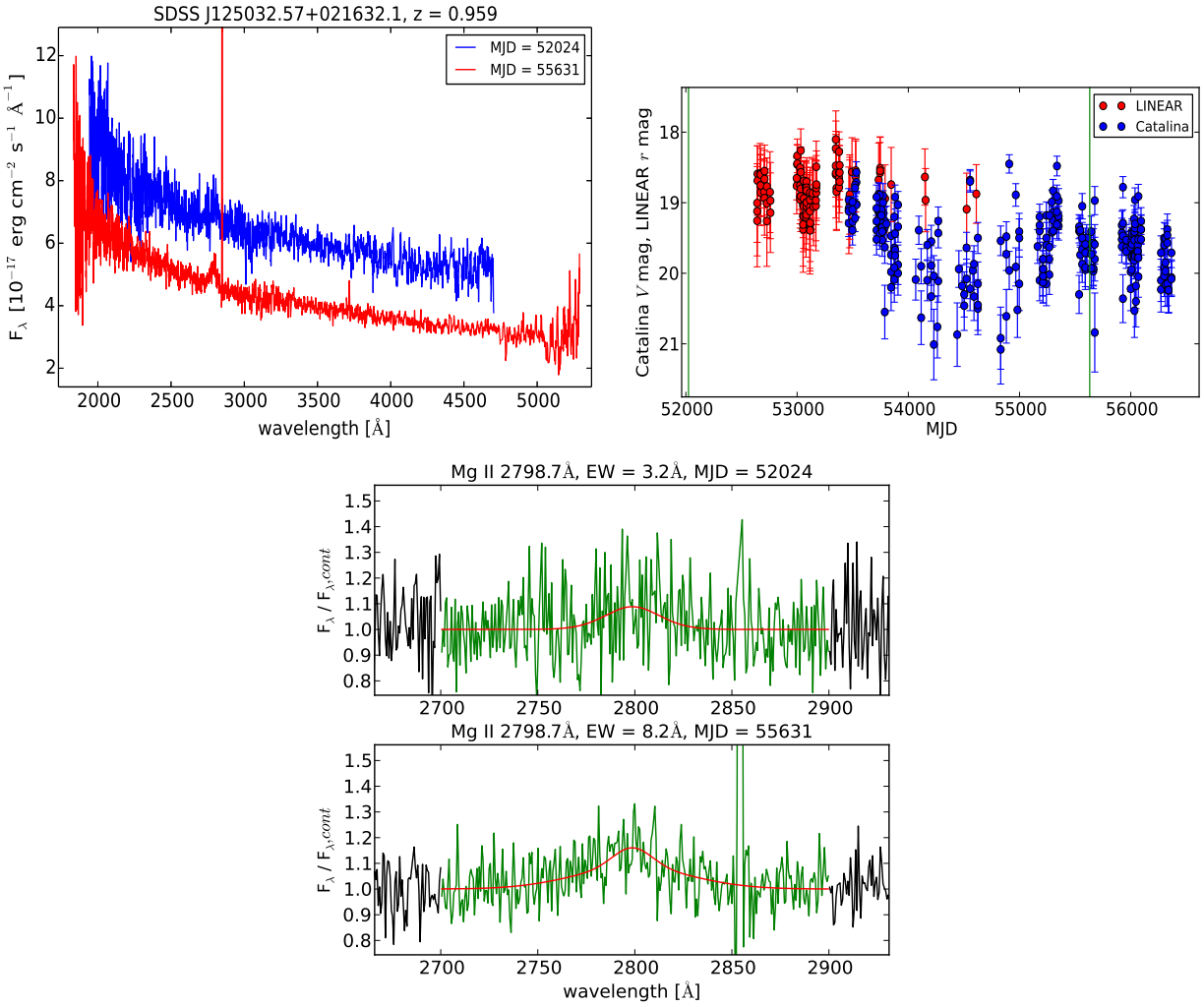

Figure 3.5: SDSS J125032.57+021632.1, similar to Figure 3.2.

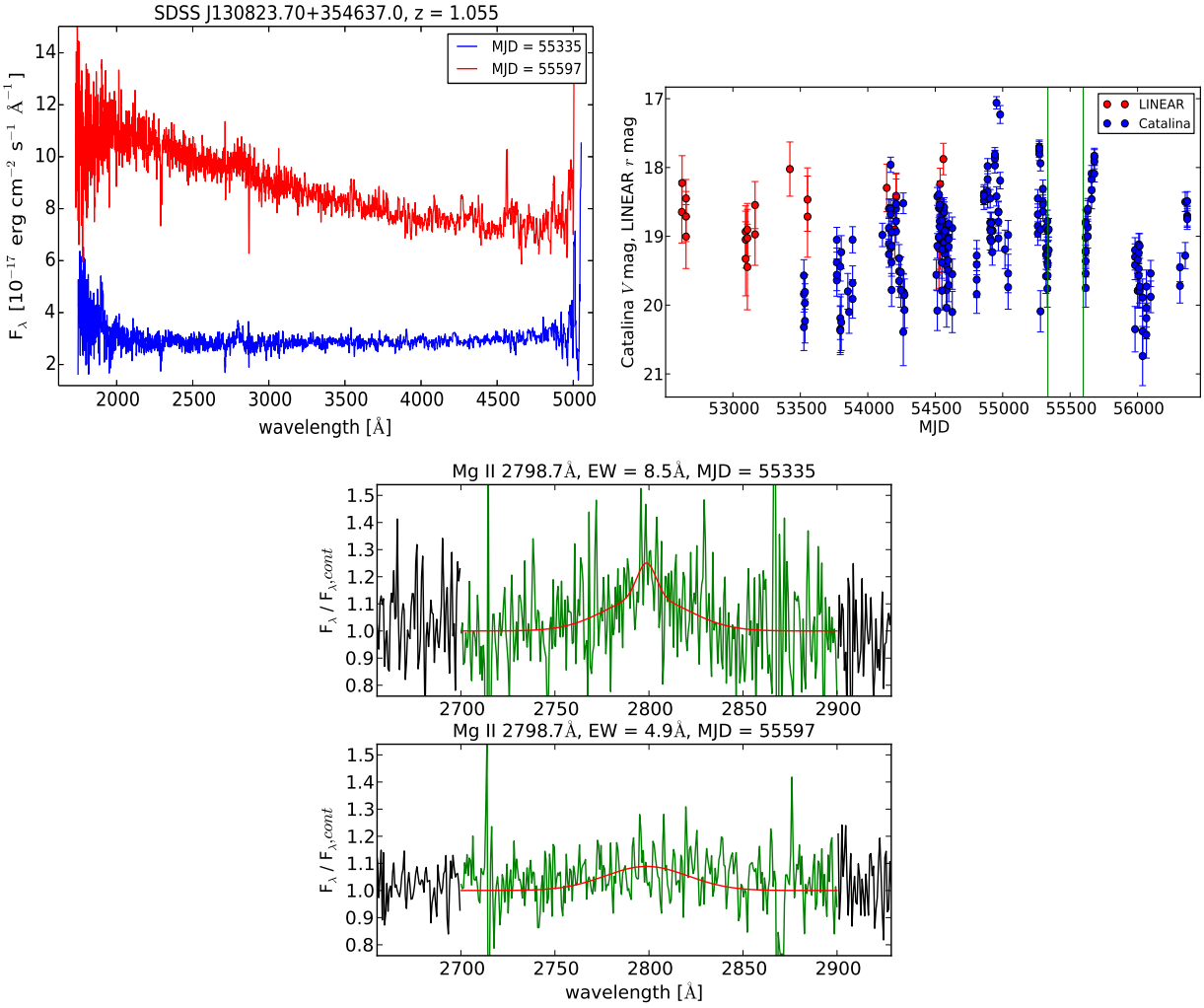

Figure 3.6: SDSS J130823.70+354637.0, similar to Figure 3.2.

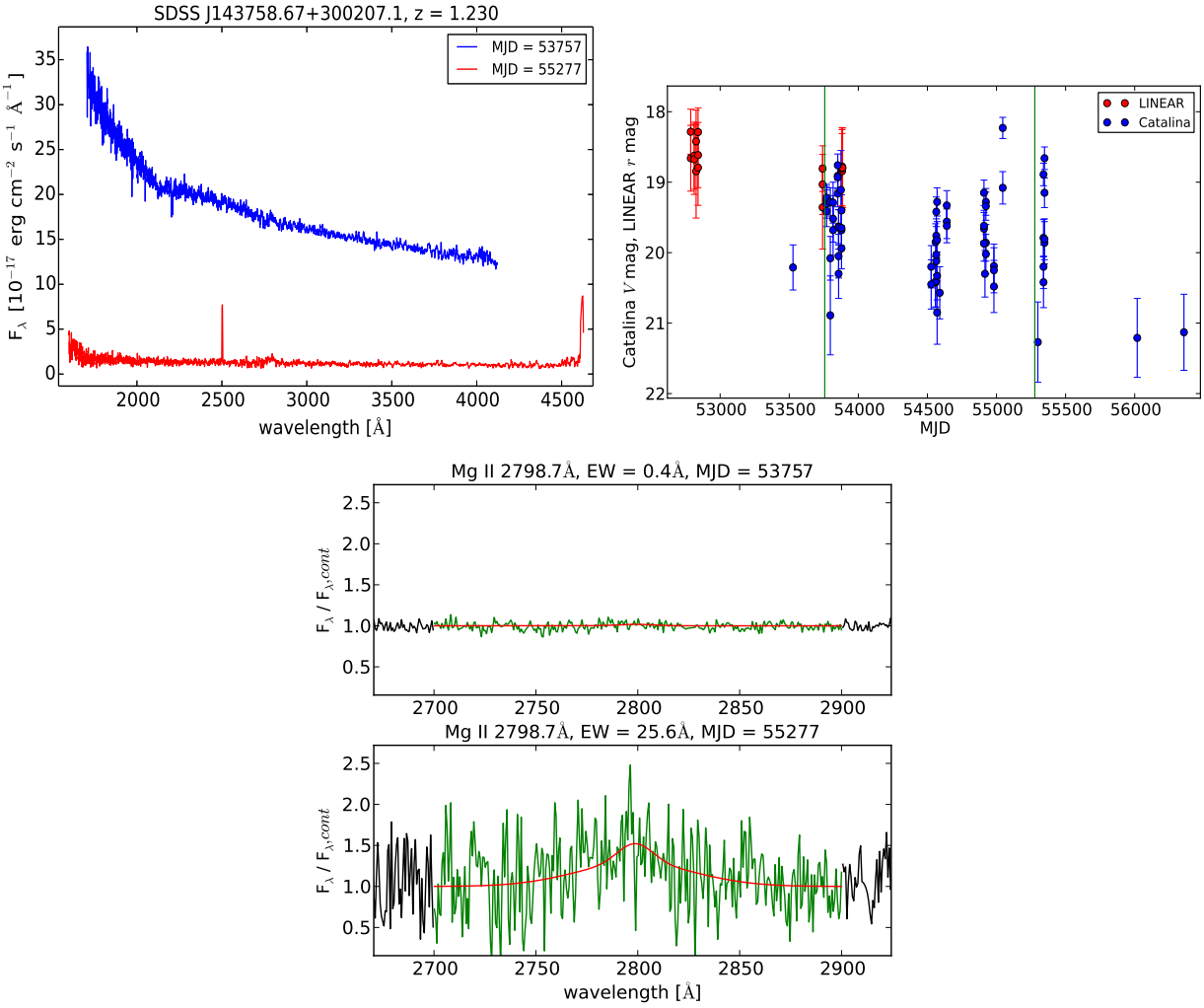

Figure 3.7: SDSS J143758.67+30027.1, similar to Figure 3.2.

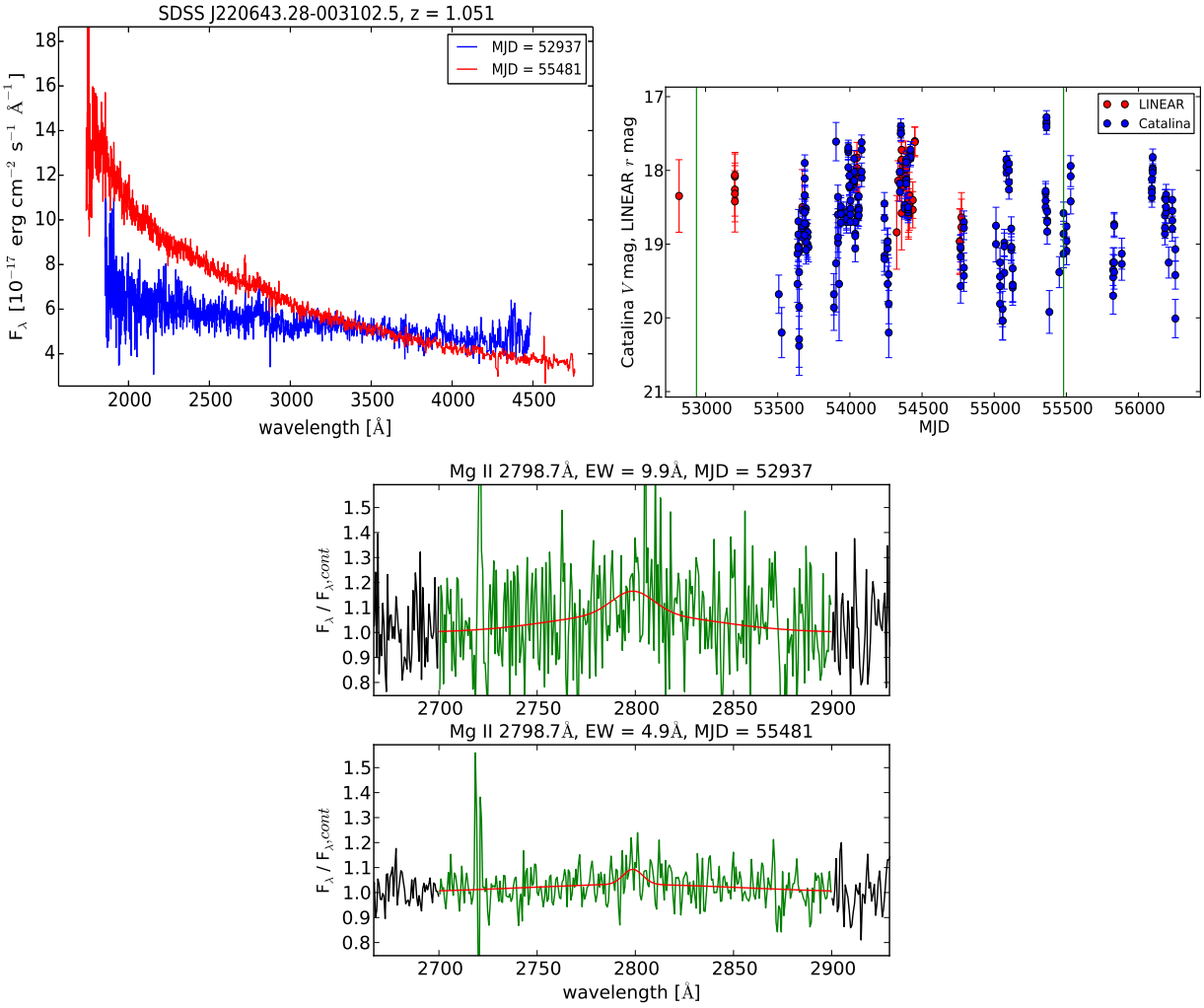

Figure 3.8: SDSS J220643.28-00312.5, similar to Figure 3.2.

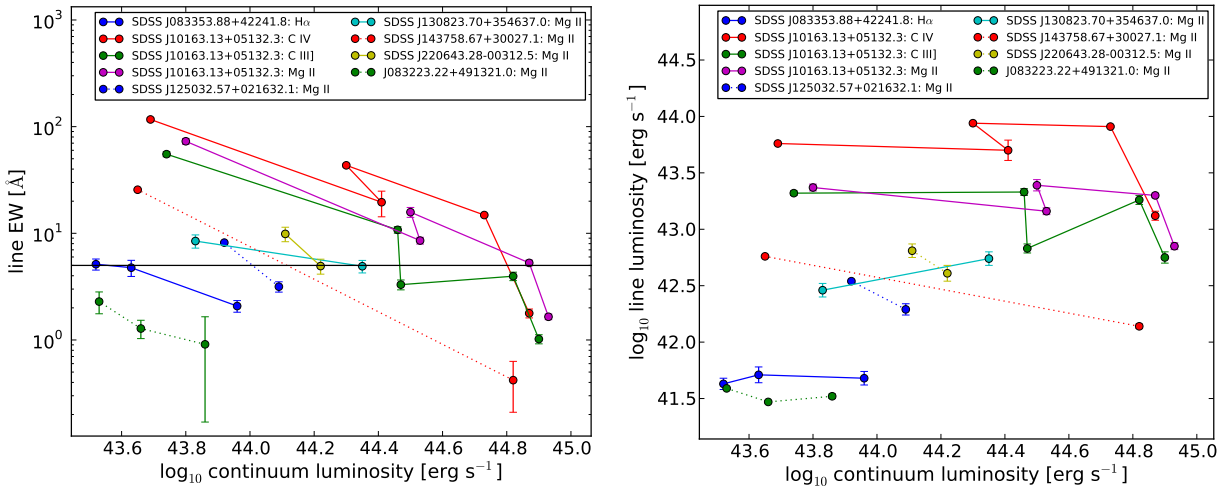

Figure 3.9: Left: The broad emission line rest-frame equivalent width versus the fitted continuum luminosity at the line, for all lines present in the six transition blazars and one additional blazar in our sample. Measurements from all spectral epochs for each line are shown, and connected in temporal order. The distinct anti-correlation strongly indicates that changes in the equivalent width of the lines are primarily due to swamping from the highly variable continuum. Right: Similar to the left panel, but for the line luminosity versus the continuum luminosity at the line. The line luminosities also show variability, possibly due to variability in the ionizing continuum from a radiatively-efficient accretion disk.

3.3 Properties of Transition Blazars

3.3.1 Emission Line Properties

The homogeneous nature of SDSS spectra allows us not only to identify a sample of transition blazars with well-determined redshifts, but also to characterize robustly their emission line properties. Using the BEL fits described in Section 3.2.1, we calculate their intrinsic line luminosities over their corresponding BEL wavelength windows; these line luminosities are also listed in Table 3.1. Figure 3.10 (left panel) shows the BEL EW versus the fitted continuum luminosities in the BEL wavelength windows, for all epochs of the BELs of each

transition blazar in temporal order. A clear anti-correlation is present across different BELs and in each of the different blazars, for nearly all epochs. This anti-correlation strongly suggests that the EW variability causing the transition blazar phenomenon in our sample is primarily due to swamping of the emission lines by the jet continuum emission, which is highly variable due to Doppler boosting. However, the emission lines themselves can also have intrinsic variability in their luminosities, which could contribute to their observed EW changes. Figure 3.10 (right panel) shows the line luminosity versus the continuum luminosity of the same lines as the left panel. The lines are variable up to $\gtrsim$0.5 dex in luminosity; in some instances (e.g. SDSS J125032.57+021632.1), the BEL luminosities appear to show an additional anti-correlation with the continuum luminosity (i.e. the lines become more luminous as the continuum luminosity decreases), further increasing the EW variability. Variations in luminosity of BELs of 0.6 dex have also been previously observed in the namesake BL Lac object (Corbett et al., 1996), which is a known transition blazar.

We use the line luminosities to estimate the bolometric Eddington ratio ($L_{\rm bol}/L_{\rm Edd}$), as well as the Eddington ratio of the broad line emission ($L_{\rm BLR}/L_{\rm Edd}$). These two quantities which probe the accretion state are often used to investigate blazar subclasses in large samples (e.g., Ghisellini et al., 2011; Shaw et al., 2012), allowing us to place the accretion state of our transition blazars in a broader context. We calculate $L_{\rm bol}/L_{\rm Edd}$ of the transition blazars in our sample following the method of Shaw et al. (2012), largely based on the results of SH11. We first estimate the unbeamed thermal continuum luminosity at 3000Å using its correlation with the Mg II line luminosity determined by SH11 from a large sample of quasars,

$$\log\left(\frac{L_{\rm cont}}{\rm erg\ s^{-1}}\right) = a \cdot \log\left(\frac{L_{\rm line}}{\rm erg\ s^{-1}}\right) + b, \tag{3.1}$$

where $a = 1.016 \pm 0.003$ and $b = 1.22 \pm 0.11$ for the Mg II BEL. We use this correlation to estimate the continuum luminosity rather than a direct measurement because the continuum emission in blazars is often dominated by non-thermal jet emission. The bolometric luminosity is estimated by multiplying the continuum luminosity at 3000Å from Equation

3.1 by the bolometric correction of $L_{\rm bol}/L_{3000} = 5.15$ from Richards et al. (2006). Using the luminosity and the fitted FWHMs of the Mg II lines, we estimate black hole masses $M_{\rm BH}$ using the relation

$$\log\left(\frac{M_{\rm BH}}{M_\odot}\right) = c + d \cdot \log\left(\frac{L_{\rm line}}{10^{44}{\rm erg\ s^{-1}}}\right) + 2\,\log\left(\frac{\rm FWHM}{\rm km\ s^{-1}}\right), \tag{3.2}$$

where $c = 1.70 \pm 0.07$ and $d = 0.63 \pm 0.00$, also determined by SH11.

For the low-z blazar SDSS J083353.88+422401.8, Mg II is not in the observed spectral wavelength range, and so the Eddington ratio must be calculated using other BELs. Hα is the only measurable BEL in this blazar, as Hβ is too weak to be discernible from the continuum, even in the low continuum luminosity epochs. We thus estimate $M_{\rm BH}$ using its relation with the Hα line luminosity and FWHM, determined by SH11 (their Equation 10) and based on Greene & Ho (2005). Because SH11 did not measure correlations between continuum and line luminosities for Hα, we estimate the continuum luminosity L_{5100} by first estimating the FWHM of Hβ (not observable) using its correlation with the Hα FWHM determined in SH11. We can then estimate L_{5100} from its relation with the $M_{\rm BH}$ and the Hβ FWHM, using Equation 5 from Shaw et al. (2012) with their constants $a = 0.672$ and $b = 0.61$, determined by McLure & Dunlop (2004). Finally, the bolometric luminosity is calculated using $L_{\rm bol}/L_{5100} = 9.26$ (Richards et al., 2006).

We estimate the $M_{\rm BH}$ and $L_{\rm bol}/L_{\rm Edd}$ of each blazar using the spectral epochs for which the BELs have the largest EWs; these values are also listed in Table 3.1. All uncertainties on these derived quantities include the propagated statistical uncertainties from the spectral line fitting, as well as the reported statistical and systematic uncertainties of the constants in each of the scaling relations. We are also able to estimate $L_{\rm bol}$ and $M_{\rm BH}$ for SDSS J101603.13+051302.3 using C IV independently in addition to Mg II; this calculation is performed using $a = 0.863 \pm 0.009$ and $b = 7.66 \pm 0.41$ in Equation 3.1 (SH11), where the line luminosity is for C IV and the continuum luminosity is for 1350Å, and using a bolometric correction of $L_{\rm bol}/L_{1350} = 3.81$ (Richards et al., 2006). The $M_{\rm BH}$ based on C IV

is then calculated by setting $c = 1.52 \pm 0.22$ and $d = 0.46 \pm 0.01$ in Equation 3.2 (SH11). The $M_{\rm BH}$ and $L_{\rm bol}/L_{\rm Edd}$ are calculated independently from C IV and Mg II in this object are consistent to within the uncertainty.

We also estimate the total luminosity of the broad line emission to estimate the Eddington ratio of the BELs ($L_{\rm BLR}/L_{\rm Edd}$). This calculation is done similar to the method of Celotti et al. (1997), who found that the ratio of the total luminosity of all BELs to the line luminosities ($L_{\rm BLR}/L_{\rm line}$) for Hα, Mg II, and C IV are 555.76/77, 555.76/34, 555.76/63, respectively, based primarily on BEL flux ratios in the quasar composite spectrum of Francis et al. (1991). Using these factors, we calculate $L_{\rm BLR}$ for each of our transition blazars at the spectral epoch with largest EW, similar to that done for $L_{\rm bol}/L_{\rm Edd}$ above. For SDSS J101603.13+051302.3, the $L_{\rm BLR}$ independently based on C IV is also highly consistent with Mg II. Although a single measurement of $L_{\rm bol}/L_{\rm Edd}$ is most helpful for classification in cases where multiple BEL are available (e.g. by averaging estimates derived from multiple lines), we opt to use the estimate from Mg II as the fiducial $L_{\rm bol}/L_{\rm Edd}$ for J101603.13+051302.3 due to its smaller scatter in the $M_{\rm BH}$ scaling relations we use in comparison to that of C IV, which instead serves as a helpful consistency check. Figure 3.10 presents the bolometric Eddington ratio of the transition blazars against the Eddington ratio of the BELs for the transition blazars in our sample, as well as for the blazar which did not transition. The Eddington ratios of these blazars are similar to the Eddington ratios of typical FSRQs (and much larger than those from radiatively inefficient accretion flows in BLLs); we discuss our interpretation of these results in Section 3.5.

3.3.2 Spectral Energy Distribution Properties

Blazars are well-known to emit strongly at a wide range of wavelengths, and their SEDs are dominated by synchrotron emission at radio up to soft X-ray wavelengths, and inverse-Compton emission at hard X-ray to γ-ray wavelengths. The peaks of the synchrotron and inverse-Compton emission tend to occur at lower frequencies for FSRQs than for BLLs in general, although BLLs have often been further subdivided into low-, intermediate-, and

high-synchrotron peaked BLLs, leading to the idea of a possible continuous 'blazar sequence' of SEDs (Fossati et al., 1998; Ghisellini & Tavecchio, 2008). We compile SEDs for the transition blazars in our sample using the ASI Science Data Center Virtual Observatory SED builder[2] (Stratta et al., 2011), conveniently linked to all blazars in the ROMA-BZCAT catalog. The archival multi-wavelength data available are most complete at radio to optical wavelengths, and visual inspection of the SEDs of our sample of transition blazars shows that the synchrotron peak is well-determined for all but one (SDSS J143758.67+300207.1), which has few data points in its SED.

We estimate the frequency and luminosity of the synchrotron peak of the transition blazars (except for SDSS J143758.67+300207.1) by fitting a third-order polynomial to the synchrotron emission in the SEDs. In the fitting, we have purposely excluded data points at frequencies $>10^{17}$ Hz to avoid inverse-Compton emission. The estimated synchrotron peak frequencies and luminosities are listed in Table 3.2. These order of magnitude estimates are approximate since we are not fitting a physically-motivated model to the SED, and the archival SED data points are not contemporaneous. However, the SED peaks are reasonably well-determined, and sufficient for classification of SED type. All the measured peak frequencies of these transition blazars are similar to the 10^{13-14}Hz range of low-synchrotron peaked blazars, and their luminosities are also consistent with the $>10^{43}$ erg s^{-1} luminosities of blazars in this SED class. This result is in strong contrast to the $\sim 10^{14-16}$ Hz and $\sim 10^{16-18}$ Hz synchrotron peak frequencies of intermediate- and high-synchrotron peaked blazars, respectively (Abdo et al., 2010a). Thus, the SED properties of these transition blazars (as well as SDSS J083223.22+491321.0) are consistent with FSRQs and low-synchrotron peaked BLLs.

[2]http://tools.asdc.asi.it/SED/

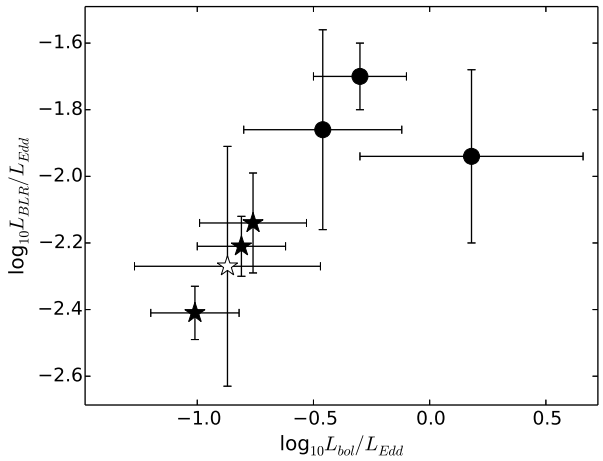

Figure 3.10: The bolometric Eddington ratio versus the Eddington ratio of the total broad emission line luminosity for the six transition blazars in our sample (filled symbols), and the additional blazar which did not transition (open star). These values are listed in Table 3.1. Blazars with *Fermi* detections are shown with stars, and without are shown with dots. These Eddington ratios are much larger than the $L_{\rm bol}/L_{\rm Edd} \sim 0.01$ typical of radiatively inefficient accretion flows in BLLs, and are instead consistent with those of classical thin accretion disks in FSRQs.

Table 3.2. γ-ray and long-term photometric variability properties of the transition blazars in our sample.

SDSS Object	$\log_{10}L_\gamma$ [a] [erg s^{-1}]	α_γ [b]	$\log_{10}\nu^{c}_{peak}$ [Hz]	$\log_{10}L^{d}_{peak}$ [erg s^{-1}]	$\log_{10}\mathrm{SF}_\infty$ [e] [mag]	$\log_{10}\tau$ [f] [days]
J083223.22+491321.0			13.12	45.51	−0.14	1.33
J083353.88+422401.8	45.22	2.33	14.11	44.80	−0.21	1.38
J101603.13+051302.3	47.99	2.08	13.27	45.94	0.31	0.79
J125032.57+021632.1			13.74	45.49	0.05	1.76
J130823.70+354637.0	46.89	2.28	12.88	45.89	−0.09	0.81
J143758.67+300207.1					0.13	0.93
J220643.28−003102.5	46.61	2.16	13.04	46.02	−0.06	0.78

[a]0.1 - 100 GeV luminosity from Nolan et al. (2012)

[b]0.1 - 100 GeV photon number power-law index from Nolan et al. (2012)

[c]Estimated frequency of the synchrotron peak in the SED.

[d]Estimated luminosity of the synchrotron peak in the SED.

[e]Optical photometetric variability amplitude on long timescales.

[f]Characteristic timescale of optical photometric variability in the rest-frame.

3.3.3 γ-ray Properties

The Large Area Telescope (Atwood et al., 2009) aboard *Fermi*'s has surveyed the γ-ray sky to unprecedented depth, thus far detecting 1,873 γ-ray sources in the 2-year 2FGL catalog (Nolan et al., 2012), including 1,121 AGN in the 2nd *Fermi* AGN catalog (Ackermann et al., 2011). The overwhelming majority of *Fermi*-detected AGN are blazars, approximately evenly divided between FSRQs and BLLs. Analysis of these *Fermi* blazars has revealed that BLLs tend to have γ-ray luminosities $L_\gamma \lesssim 10^{46}$ erg s^{-1} and γ-ray spectral indices $\alpha_\gamma \lesssim 2.2$ in the 0.1 - 100 GeV band, while FSRQs exceed these values. However, there is significant overlap in these γ-ray properties between the two subclasses (Ackermann et al., 2011), likely due to some combination of large measurement uncertainties and misclassification, in addition to astrophysical origins.

We match our transition blazars to the *Fermi* 2FGL catalog to investigate their γ-ray properties. Four of the blazars in our sample are matched to 2FGL sources that have association probabilities >95% (i.e. the blazar is highly likely to be the optical counterpart of the γ-ray source); their γ-ray luminosities and spectral indices are also listed in Table 3.2. None of the four transition blazars in our sample detected by *Fermi* can be clearly classified based on their γ-ray properties, and all lie in the area occupied by FSRQs and low-to-intermediate synchrotron peaked BLLs. Ghisellini et al. (2011) argued that for such objects, a better classifier to use is the Eddington ratio based on the BEL ($L_{\rm BLR}/L_{\rm Edd}$), with a dividing value of $\sim 5\times10^{-4}$. We note that although synchrotron peak frequencies and luminosities of these transition blazars (where determined) are similar, not all are detected in γ-rays.

3.3.4 Optical Variability Properties

Blazars are well-known to be among the most variable extragalactic objects detected in large-scale optical time-domain surveys (Bauer et al., 2009b). An investigation of long-term optical light curves recalibrated by Sesar et al. (2011) from the Lincoln Near-Earth Asteroid

Research (LINEAR, Stokes et al., 2000) survey by Ruan et al. (2012) revealed that the jet synchrotron-dominated continuum emission in blazars is systematically more variable than the thermal disk-dominated continuum in typical Type 1 quasars. In particular, Ruan et al. (2012) found that blazars have typical optical variability amplitudes of $\sim$0.5 mag in the r-band on rest-frame timescales greater than $\sim$100 days; below this characteristic timescale, the optical variability is self-correlated and smaller in amplitude. The strong variability amplitudes and short variability timescales observed in comparison to typical quasars was interpreted by Ruan et al. (2012) as due to the effects of Doppler boosting in the relativistic jet of blazars.

We compile publicly-available optical light curves of the transition blazars in our sample from the LINEAR and Catalina Sky Survey/Catalina Real-Time Transient Survey (Drake et al., 2009) databases to investigate their optical variability properties. The optical light curves constructed using these two surveys are also shown in Figures 3.2 to 3.7; they are well-sampled, with 98 - 978 epochs (median of 444 epochs) spread over $\sim$11 years in the observed-frame. All transition blazars in our sample display strong optical variability, with maximum amplitude on the range of $\sim$1.5 to 6 mags in the data.

To compare the optical variability properties of these transition blazars to the large sample of FSRQs and BLLs from Ruan et al. (2012), we fit each of these light curves to a first-order continuous autoregressive model (i.e., a damped random walk) using the method of Kozłowski et al. (2010), and discussed in detail in MacLeod et al. (2010). Figure 3.11 compares the rest-frame characteristic timescale of variability τ, and the variability amplitude on long timescales (when the variability is uncorrelated and strongest) SF_∞, of these seven blazars to the large sample of 60 bright blazars from Ruan et al. (2012). The seven blazars in our sample have larger variability amplitudes and shorter timescales of variability than typical blazars. A two-sample Kolmogorov-Smirnov test between the distributions of τ and SF_∞ in Figure 3.11 for our transition blazars and the blazar sample of Ruan et al. (2012) results in a p-value of 3.1×10^{-3} for τ, and 5.6×10^{-4} for SF_∞.

Although the light curves we construct use data from both LINEAR and the Catalina

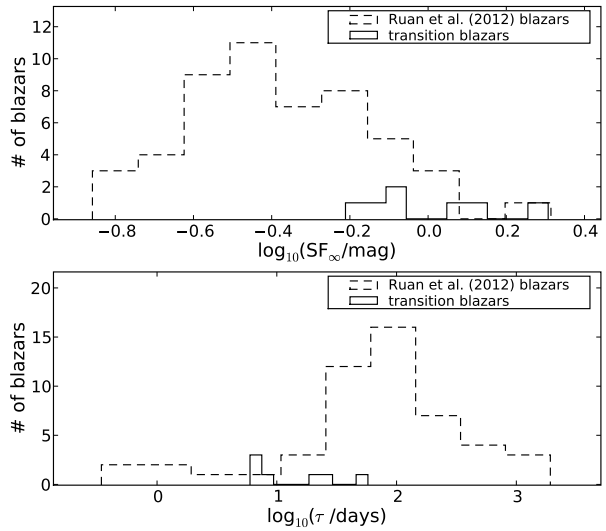

Figure 3.11: Top: Histogram of the variability amplitude on long timescales for the long-term photometric light curves of the seven blazars in our sample modeled as a damped random-walk, as well as for a sample of 60 blazars from Ruan et al. (2012). Bottom: Similar to the top panel, but for the characteristic timescale of variability in the rest-frame. The seven blazars in our sample have significantly larger variability amplitudes and shorter timescales of variability than typical blazars, supporting the interpretation that the jet emission is particularly strongly-beamed.

surveys, the filters and calibrations are not exact between these two surveys; this issue will lead to a systematic offset between their measured magnitudes. However, both surveys used white-light filters and the systematic offset in magnitude is small (<0.1 mag), especially in comparison to the several-magnitude variability observed in our transition blazar light curves. Thus, any differences in calibration between the two surveys are dwarfed by the intrinsic variability of transition blazars, and do not significantly affect our analysis.

3.4 Notes on Individual Objects

SDSS J083223.22+491321.0: The Mg II line EW of this blazar is <5Å in all three available epochs of spectra (Figure 3.2), and thus this blazar appears to be a canonical BLL and was included in our analysis for completeness due to its newly-determined redshift of $z = 0.548$. However, despite its small Mg II EW and under-luminous Mg II emission relative to the FSRQs in Shaw et al. (2012), its high bolometric Eddington ratio instead strongly suggests that it is in fact a FSRQ, and would transition with further spectroscopic monitoring. This blazar is not *Fermi*-detected.

SDSS J083353.88+422401.8: The Hα line is visible in this low-redshift blazar in all three available epochs of spectra (Figure 3.3), although its EW is small in even the largest-EW epoch. Giommi et al. (2012) suggested that blazars with BELs that transition in their optical spectra likely have highly luminous Hα emission in the observed-frame infrared with EWs that remain >5Å. However, this blazar is an example in which even the Hα emission transitions. The $M_{\rm BH}$ and Hα luminosity we calculate for this blazar are smaller than typical of FSRQs in the sample of Shaw et al. (2012), though this may be affected by our indirect method of estimating the continuum luminosity through correlations between the Hα and the unobserved Hβ BELs (see Section 3.3.1). To verify our $M_{\rm BH}$ estimate, we also fit the Hα FWHM in the second-largest EW spectral epoch (MJD = 54524) for this blazar, and compare to the largest EW epoch. The FWHMs of both epochs are highly consistent, and thus our relatively small $M_{\rm BH}$ estimate appears to be reliable. This blazar is *Fermi*-detected, and its optical light curve is exceptionally well-sampled, showing variability up to $\sim$2 magnitudes.

SDSS J101603.13+051302.3: The C IV, C III], and Mg II BELs all show strong variability in EW (up to a factor of >60) over five available epochs of SDSS spectra (Figure 3.4). The decrease in continuum luminosity in these spectra causes the BELs to transition nearly in unison. This strong EW variability is not particularly surprising, as the long-term continuum variability probed by the the broadband optical light curve varies up to $\gtrsim$5 magnitudes. This blazar is a bright *Fermi* source, and its bolometric Eddington ratio determined from Mg II

(more robust than that from C IV) shows it is accreting even more rapidly than typical FSRQs.

SDSS J125032.57+021632.1: Although this blazar did not previously have a redshift in the ROMA-BZCAT catalog, the Mg II line is well-detected in both epochs of spectra (Figure 3.5), and we determine a new robust redshift of $z = 0.959$. This blazar is not *Fermi* detected, and has an Eddington ratio of $\sim$0.1, more similar to typical quasars than FSRQs.

SDSS J130823.70+354637.0: The two epochs of spectra for this blazar are observed during dramatic dimming and flaring events in its optical light curve (Figure 3.6). These dramatic flares of $\sim$2 magnitudes appear to be a frequent occurrence for this blazar, on timescales as short as days to weeks. The Mg II line is well-detected in both epochs, and this blazar is *Fermi*-detected.

SDSS J143758.67+300207.1: The Mg II line in this blazar is weak in both epochs of spectra (Figure 3.7), but the strong continuum variability causes its EW to increase by a factor of $>$60. The redshift for this blazar ($z = 1.230$) is new, and this blazar is not *Fermi* detected. Although the optical light curve is sparsely sampled, large variations of up to $\sim$3 magnitudes are evident.

SDSS J220643.28-003102.5: This *Fermi*-detected blazar's Mg II line is much more clearly detected in the fainter-continuum epoch (Figure 3.8). The optical light curve shows strong variability, with large ($\sim$2 magnitude) flares on timescales of days to weeks. Its characteristic timescale of variability of 6 days in the rest-frame is the shortest among the transition blazars in our sample. This blazar is in the Stripe 82 multi-epoch imaging portion of SDSS, and its SDSS optical light curve is among the most variable of all quasars in MacLeod et al. (2010).

3.5 Discussion

In the previous sections, we have explored the spectral, temporal, and multi-wavelength properties of our sample of transition blazars; in this section, we will piece together these properties to understand the nature of these objects. The Eddington ratios of the transition blazars in our sample calculated in Section 3.3.1 (and shown in Figure 3.10) are more than an

order of magnitude above the approximate $L_{\rm bol}/L_{\rm Edd} \sim 0.01$ value that typically separates the radiatively efficient and inefficient accretion regimes in AGN, and are even higher than the $L_{\rm bol}/L_{\rm Edd} \sim 0.1$ typical of Type 1 quasars in SDSS (SH11). This result strongly suggests that the transition blazars in our sample are actually rapidly-accreting FSRQs, which have been found to have systematically large bolometric Eddington ratios of $L_{\rm bol}/L_{\rm Edd} \sim 0.1$ to 1 in a large *Fermi*-selected sample (Shaw et al., 2012). The $L_{\rm BLR}/L_{\rm Edd}$ of these transition blazars are correspondingly also well above the $\sim 5 \times 10^{-4}$ divide suggested by Ghisellini et al. (2011) to separate FSRQs from BLLs. We emphasize that our estimates of $L_{\rm bol}/L_{\rm Edd}$ for each transition blazar are not strongly affected by contamination from jet emission since the continuum luminosities (without jet contamination) are not directly measured in the spectrum, but rather indirectly estimated based on scaling relations with the BEL luminosities as discussed in Section 3.3.1.

Our FSRQ-like interpretation of these blazars is further supported by the strong variability observed in the BEL luminosities of up to $\sim$0.5 dex (Figure 3.10, left panel). This effect is likely due to the strong flux variability of the ionizing thermal continuum from radiatively-efficient thin accretion disks that are thought to exist in FSRQs, in contrast to the radiatively-inefficient accretion flows in BLLs, since variations in the jet continuum only weakly correlates with BEL flux variability (Isler et al., 2013). The FSRQ nature of these transition blazars is also supported by our investigation of their SEDs (Section 3.3.2), which revealed that their synchrotron peaks are at frequencies of $\sim 10^{12-13}$ Hz, and luminosities of 10^{45-46} erg s^{-1}; these SED properties are similar to FSRQs and low synchrotron-peaked BLLs, although the underlying accretion state is difficult to discern from the SED alone.

Although swamping of BELs by the jet continuum in transition blazars as suggested by the observed anti-correlation between the line EWs and continuum luminosities (see Figure 3.10) may be expected in FSRQs, the results of our systematic search reveals that such cases are instead uncommon. Our investigation suggests that the transition phenomenon occurs in rare FSRQs with particularly strongly-beamed jets, oriented at extremely small angles along the line of sight. The particularly strong beaming in such objects would lead to

correspondingly strong jet dominance of the optical spectra, as well as strong flux variability. This interpretation is supported by our investigation of the long-term optical variability of these transition blazars in Section 3.3.4: they show larger amplitudes and shorter timescales of variability (Figure 3.11) than typical blazars. This uniquely strong variability in transition blazars suggests that the jet beaming is especially strong in these objects, with large Lorentz factors.

The transitional nature of the BEL EWs in these blazars may lead to misclassifications if the subclass classification is based solely on EWs in single-epoch spectra as traditionally done. Although transition blazars are rare, misclassification can still significantly affect investigations of blazar redshift evolution at high redshifts due to their rarity. Our findings suggest that some BL Lacs may actually be strongly-beamed FSRQs, thus decreasing the apparent BL Lac population, especially at the higher redshifts of FSRQs and partially due to the high luminosities of these particularly strongly-beamed blazars. This effect can decrease the small sample sizes of high-redshift BL Lacs used in investigations of their redshift evolution, and may even add credence to claims of a BL Lac negative redshift evolution. Since the SEDs of the transition blazars in our sample are ambiguous between FSRQs and low synchrotron-peaked BLLs despite their unambiguously large accretion rates, classification based on SEDs can also lead to incorrect results. Even when multi-epoch spectra are available (thus allowing for identification of transition blazars), some studies have incorrectly assumed that transitional blazars in which all BELs have EW < 5Å in *any* epoch are BLLs (e.g., Shaw et al., 2012, 2013a). In contrast, our investigation reveals that these transition blazars are instead likely to be FSRQs.

Similar to the arguments presented in Ghisellini et al. (2011), we strongly recommend that classification of ambiguous blazars be based on Eddington ratios, especially through the use of multi-epoch spectra so that the BEL properties can be robustly determined from the large-EW spectral epochs. This Eddington ratio-based classification is useful for not only transition blazars, but also for blazars such as SDSS 083223.22+491321.0 (Figure 3.2), which does not have BEL EW > 5Å in any of the observed epochs. Although this blazar

appears to be a canonical BLL, its Eddington ratio of $L_{\rm bol}/L_{\rm Edd} \sim 0.17$ instead clearly reveals it to be a FSRQ with extreme swamping of the BELs. Additionally, the large EW variations in transition blazars observed in multi-epoch spectroscopy also aids robust redshift determinations.

Finally, despite the strong beaming in their jets that cause strong photometric variability and EW changes in the BELs, it is puzzling that not all of these transition blazars are γ-ray detected. The synchrotron peak frequencies and luminosities in SEDs of the transition blazars in our sample are all in a similar range, without any clear distinction between the γ-ray loud and quiet blazars. It is possible that the γ-ray luminosity in these jets with extreme beaming may be suppressed due to strong $\gamma\gamma$ attenuation from pair production (Becker & Kafatos, 1995a; Blandford & Levinson, 1995) or Klein-Nishina effects in the electron Compton cooling (e.g. Moderski et al., 2005). Many of the transition blazars in our sample have detections in *GALEX*, *Swift*, and *ROSAT* in addition to *Fermi*; future investigations of the high-energy inverse-Compton SED peaks of these blazars will be able to shed light on this problem. Future studies of γ-ray variability in these transition blazars will also be able probe the physical mechanism of transitions between jet-dominated and disk-dominated states (Chatterjee et al., 2013).

3.6 Conclusions

Using a large sample of 602 pairs of repeat blazar spectra of 354 blazars from SDSS, we present a systematic search for blazars that have transitioned between the BLL and FSRQ subclasses based on the EW of the BELs. These repeat spectral observations span timescales from intra-night to $\sim$12.5 years in the observed-frame, and are selected by a variety of multi-wavelength properties. We find six clear cases of transition blazars which show dramatic variability in their BEL EWs; the strong BEL EW variability allows us to determine new redshifts for two of the transition blazars in our sample, as well as one additional blazar. We investigate the SDSS spectral, γ-ray, SED, and optical variability properties of these transition blazars to understand their nature as probed by these methods. Our key results

are as follows:

1) EWs of BELs in transition blazars can vary dramatically, with observed variations up to factors of >60. Transition blazars have high accretion rates, with bolometric Eddington ratios typical of FSRQs. A clear anti-correlation between the continuum luminosity and BEL EWs strongly suggests that the transitional phenomenon is primarily due to swamping of the BELs by the highly variable jet continuum. However, the luminosities of the BELs are also variable, further supporting the existence of radiatively efficient thin accretion disks in these objects.

2) The swamping of the BELs in transition blazars occurs when the jet continuum is strongly-beamed, placing transition blazars as rare cases of FSRQs with particularly strongly-beamed jets. This interpretation is supported by analysis of their long-term photometric light curves, which display larger amplitudes and shorter timescales of variability than typical blazars, consistent with the effects of strongly-beamed jet continuum emission.

3) The SEDs of these transition blazars show low-frequency, luminous synchrotron peaks, similar to FSRQs and low-peaked BLLs. Their γ-ray properties (where detected) are also ambiguous between these two classes. Since classification based on BEL EWs, SEDs, and γ-ray properties of these objects is difficult, we suggest the use of Eddington ratios.

Although transition blazars are rare, correct classification will impact studies of the divergent properties of BLLs and FSRQs, especially regarding their redshift evolution. Future directions for investigation of these rare transition blazars can focus on understanding the nature of the strong beaming using radio observations, and study of their high-energy inverse-Compton SED peaks to understand why only some of these strongly-beamed FSRQs are γ-ray loud. Future surveys such as the Time-Domain Spectroscopic Survey (Green et al., 2014) of SDSS-IV will include more repeat spectra of blazars, and will uncover many more such transitional cases.

3.7 Acknowledgments

JJR thanks James R. A. Davenport for helpful discussions. Support for JJR was provided by NASA through Chandra Award Numbers AR9-0015X, AR0-11014X, and AR2-13007X, issued by the Chandra X-ray Observatory Center, which is operated by the Smithsonian Astrophysical Observatory for and on behalf of NASA under contract NAS8-03060. Support for WNB was provided by NSF grant AST-1108604 and NASA ADP grant NNX10AC99G.

Funding for SDSS-III has been provided by the Alfred P. Sloan Foundation, the Participating Institutions, the National Science Foundation, and the U.S. Department of Energy Office of Science. The SDSS-III web site is http://www.sdss3.org/.

SDSS-III is managed by the Astrophysical Research Consortium for the Participating Institutions of the SDSS-III Collaboration including the University of Arizona, the Brazilian Participation Group, Brookhaven National Laboratory, Carnegie Mellon University, University of Florida, the French Participation Group, the German Participation Group, Harvard University, the Instituto de Astrofisica de Canarias, the Michigan State/Notre Dame/JINA Participation Group, Johns Hopkins University, Lawrence Berkeley National Laboratory, Max Planck Institute for Astrophysics, Max Planck Institute for Extraterrestrial Physics, New Mexico State University, New York University, Ohio State University, Pennsylvania State University, University of Portsmouth, Princeton University, the Spanish Participation Group, University of Tokyo, University of Utah, Vanderbilt University, University of Virginia, University of Washington, and Yale University.

The LINEAR program is sponsored by the National Aeronautics and Space Administration (NRA No. NNH09ZDA001N, 09-NEOO09-0010) and the United States Air Force under Air Force Contract FA8721-05-C-0002. Opinions, interpretations, conclusions, and recommendations are those of the authors and are not necessarily endorsed by the United States Government.

The Catalina Sky Survey is funded by the National Aeronautics and Space Administration under Grant No. NNG05GF22G issued through the Science Mission Directorate Near-Earth

Objects Observations Program. The CRTS survey is supported by the U.S. National Science Foundation under grants AST-0909182.

Part of this work is based on archival data, software or on-line services provided by the ASI Science Data Center (ASDC).

Chapter 4

TOWARDS AN UNDERSTANDING OF CHANGING-LOOK QUASARS

The peak of cosmic quasar activity occurs at redshift $z \sim 2$, after which quasars turn off and thus transform into the low-luminosity AGN or quiescent galaxies we observe in the local Universe. The shutoff of accretion in individual quasars is expected to occur over timescales of $\sim 10^{4-5}$ years, and has thus not been directly observed previously. However, the recently-discovered 'changing-looking' quasar phenomenon – in which a luminous quasar dims significantly to a quiescent state in repeat spectroscopy over $\sim$10 year timescales – may present unexpected challenges to our understanding of quasar accretion. In this chapter, I take a first step to better understand this phenomenon by building a sample of changing-look quasars with a systematic but simple archival search for these objects in the Sloan Digital Sky Survey Data Release 12. By leveraging the >10 year baselines for objects with repeat spectroscopy, I uncover two new changing-look quasars, and a third discovered previously. Decomposition of the multi-epoch spectra and analysis of the broad emission lines suggest that the quasar accretion disk emission dims due to rapidly decreasing accretion rates (by factors of $\gtrsim$2.5), while disfavoring changes in intrinsic dust extinction for the two objects where these analyses are possible. Broad emission line energetics also support intrinsic dimming of quasar emission as the origin for this phenomenon rather than transient tidal disruption events or supernovae. Although my search criteria included quasars at all redshifts and transitions from either quasar-like to galaxy-like states or the reverse, all of the clear cases of changing-look quasars discovered were at relatively low-redshift ($z \sim 0.2 - 0.3$) and only exhibit quasar-like to galaxy-like transitions.

Material from this chapter was previously published in collaboration with Scott F. Ander-

son, Sabrina L. Cales, Michael Eracleous, Paul J. Green, Jessie C. Runnoe, Yue Shen, Tessa D. Wilkinson, Michael R. Blanton, Tom Dwelly, Antonis Georgakakis, Jenny E. Greene, Stephanie E. Lamassa, Andrea Merloni, and Donald P. Schneider in the August 2016 edition of the Astrophysical Journal (Ruan et al., 2016a), and has been reproduced here with permission of the American Astronomical Society.

4.1 Introduction

The quasar phenomenon is thought to be a relatively brief stage of galaxy evolution involving rapid accretion onto the central supermassive black hole (SMBH; e.g., Salpeter, 1964; Lynden-Bell, 1969; Rees, 1978). Observational constraints on lifetimes show that quasar phases in galaxies generally last for a total of 10^{7-8} years (Martini & Weinberg, 2001; Kelly et al., 2010), after which the accretion rate drops dramatically and the active nucleus transitions to a low-luminosity active galactic nucleus (AGN) or quiescent galaxy state (Churazov et al., 2005). Cosmological simulations of galaxy formation that include sub-grid models of SMBH growth and feedback have suggested that the accretion history of SMBHs may be episodic, where luminous quasar phases are regulated by quasar feedback processes (e.g., Di Matteo et al., 2005; Hopkins et al., 2005; Springel et al., 2005). Although the exact characteristics of quasar light curves over cosmic time are difficult to infer observationally, indirect arguments based on AGN populations (Schawinski et al., 2015) and properties of their host-galaxies (Hickox et al., 2014) have also suggested that AGNs dramatically 'flicker' in luminosity between luminous quasar and quiescent galaxy phases. However, direct observations of such transitions in luminous quasars have thus far been scarce.

It has been suggested that the transition from quasars to low-luminosity AGN or quiescent galaxies may not be observable in individual objects due to the long timescales expected for this process. Such dramatic changes in the accretion state are commonly observed in X-ray binaries, which can undergo spectral state transitions between the high-luminosity/soft-spectrum and low-luminosity/hard-spectrum states in the X-rays (e.g., Homan & Belloni, 2005). Scaling the hours-long timescales observed for these spectral state transitions in X-

ray binaries to $\sim 10^8$ $M_\odot$ SMBHs predicts transition timescales in quasars of $\sim 10^{4-5}$ years (Sobolewska et al., 2011). Indirect evidence for a luminous quasar transition in an individual object was previously provided by observations of Hanny's Voorwerp, a serendipitously discovered ionized emission-line gas cloud lying $\sim$20 kpc away from the quiescent galaxy IC2497 (Lintott et al., 2009). Based on multi-wavelength observations, it is argued that this gas cloud could only have been ionized by an AGN continuum with luminosity $\gtrsim 10^{45}$ erg s^{-1}; this implies that the nearby quiescent galaxy was recently in a quasar state, with a transition timescale of $\sim 10^4$ years and consistent with expectations (Schawinski et al., 2010; Keel et al., 2012a). Since this discovery, many other candidate fading AGNs with extended emission-line regions have been found and investigated, resulting in similar inferred transition timescales (e.g., Keel et al., 2012b, 2015).

Previously, transitions of Seyfert 1 galaxies to Seyfert 1.8/1.9 (and/or vice versa) have been directly observed in repeat optical spectroscopy over timescales of $\sim$10 years (Goodrich, 1995; Shappee et al., 2014; Denney et al., 2014). Goodrich (1995) showed that the origin of the observed transition in some of these AGNs are consistent with intrinsic changes in the AGN continuum emission, while variations in dust obscuration along the line of sight is favored for others, although these two effects may occur in concert if dust is embedded in the narrow-line region gas (Netzer & Laor, 1993). Similar behavior has also been previously observed in the X-ray spectra of Seyfert galaxies (termed "changing-look AGN"), also interpreted as being due to either dramatic changes in obscuration or intrinsic changes in the nuclear emission (e.g., Guainazzi, 2002; Matt et al., 2003; Puccetti et al., 2007; Risaliti et al., 2009; Marchese et al., 2012). The recent discovery of the first changing-look (CL) quasar by LaMassa et al. (2015) extends this transitional phenomenon to AGNs in new luminosity and redshift regimes (see Figure 1 of LaMassa et al. 2015). Repeat optical spectroscopy of this luminous quasar (SDSS J015957.64+003310.5, hereafter J0159+0033) shows a dramatic decrease in the quasar continuum emission, accompanied by disappearance of the broad Hβ line and strong dimming of the broad Hα line, showing that a simple orientation-based view of AGN unification is incomplete. Surprisingly, the observed transition in this CL quasar

occurred over rest-frame timescales of $\sim$7 years; this is much shorter than the $\sim 10^4$ year timescales expected for this transition to occur from previous arguments based on X-ray binaries and extended emission line regions surrounding quiescent galaxies.

The origin of changing-look behavior in luminous quasars is uncertain. LaMassa et al. (2015) demonstrated that the observed dimming of the quasar continuum in J0159+0033 coincides with broadening of the broad Balmer emission lines, such that the derived black hole mass (estimated through single-epoch spectroscopic black hole mass methods) is preserved. This behavior is consistent with intrinsic dimming of the quasar continuum emission, while a scenario in which the continuum and emission line dimming is caused by an increase in dust extinction is disfavored through modeling of the spectral changes. Furthermore, LaMassa et al. (2015) also argue that obscuration by a dust cloud outside the broad line region in a circular Keplerian orbit is unlikely since its crossing time across the broad line region would be much longer than the observed transition timescale.

If the dimming of quasar emission in CL quasars is intrinsic, then the observed behavior can be caused by dramatic changes in the accretion flow, which may occur during transitions between radiatively efficient and inefficient accretion regimes (Ichimaru, 1977; Rees et al., 1982; Narayan & Yi, 1994). Thermal and dynamical instabilities in the accretion disk may also produce strong changes in the disk emission on even shorter timescales (Lin & Shields, 1986; Siemiginowska et al., 1996). Merloni et al. (2015) argued that the LaMassa et al. (2015) CL quasar may instead be a transient stellar tidal disruption event (TDE) near the central SMBH (see also Eracleous et al., 1995), which would cause a luminous nuclear flare, followed by a slow dimming over the few-years timescales observed. This scenario is supported by their image-differencing light curves of this CL quasar, which show that the time evolution of the broadband nuclear emission is consistent with that expected from TDEs. In any of these scenarios, CL quasars represent an intriguing new phenomenon that can provide unique insights to AGN accretion and structure, and warrant additional investigation.

Since the discovery of LaMassa et al. (2015), at least two more spectroscopic CL quasars have been serendipitously discovered (Runnoe et al., 2016), primarily through visual inspec-

tion of early spectroscopic data from the Time-Domain Spectroscopic Survey (Morganson et al., 2015) in the Sloan Digital Sky Survey IV (SDSS IV). These results suggest that CL quasars may be surprisingly common, and can be found by mining spectral data sets with large numbers of repeat quasar and galaxy spectra over a sufficiently long baseline. Motivated by these results, we present a simple archival search for CL quasars in SDSS-I/II/III Data Release 12 (DR12, Alam et al., 2015), which includes a total of $\sim 4 \times 10^6$ optical/near-IR spectra over $\sim$10,000 deg^2 of sky. This data set includes a significant number of repeat spectra spanning a $\gtrsim$10 year baseline, and many of its various science programs specifically targeted quasars and galaxies. We aim to cast a wide net in this investigation, and include quasar and galaxies at all redshifts while remaining impartial in our search with regard to whether each object transitions from a quasar-like to galaxy-like state or vice versa; this approach could not only yield a sample of CL quasars, but also potentially a spectroscopic transition from quiescent galaxy to luminous quasar, which would have intriguing implications for their origin.

The outline of this paper is as follows: Section 4.2 presents the data sets and criteria used in our search. In Section 4.3, we describe the changing look quasars found in our search and modeling of their broad emission lines. Section 4.4 evaluates evidence from our sample favoring various scenarios for the origin of CL quasars. We summarize and conclude in Section 4.5. Throughout this paper, we assume a standard ΛCDM cosmology with $\Omega_{\rm m} = 0.309$, $\Omega_\Lambda = 0.691$, and $H_0 = 67.7$ km s^{-1} Mpc^{-1}, consistent with the *Planck* full-mission results of Planck Collaboration et al. (2015).

4.2 An Archival Spectroscopic Search

4.2.1 Search Criteria

We utilize the list of all 4,355,202 spectra in SDSS (York et al., 2000) DR12, and perform the selection cuts detailed below to produce a final sample of 117 CL quasar candidates. These spectra were taken by the SDSS 2.5m telescope (Gunn et al., 2006) using the SDSS-I/II and

Table 4.1. Measured SDSS spectral properties of the changing-look quasars in our sample.

SDSS Object	z	MJD	Hα FWHM[a] [km s^{-1}]	$\log_{10}L_{\mathrm{H}\alpha}$[a] [erg s^{-1}]	Hβ FWHM[a] [km s^{-1}]	$\log_{10}L_{\mathrm{H}\beta}$[a] [erg s^{-1}]	$\log_{10}\lambda L_{5100}$ [erg s^{-1}]
J015957.64+003310.5[b]	0.312	51871	3788 ± 163	42.36 ± 0.04	4714 ± 682	41.88 ± 0.63	43.52 ± 0.05
		55201	5954 ± 857	41.72 ± 0.11	....	<41.32[c]	43.27 ± 0.06
J012648.08−083948.0	0.198	52163	4121 ± 223	42.00 ± 0.04	4297 ± 1165	41.55 ± 0.20	43.43 ± 0.03
		54465	....	<40.20[d], <40.51[e]	...	<40.17[f], <40.28[g]	<42.30[c]
J233602.98+001728.7	0.243	52096[h]	6289 ± 1180	41.86 ± 0.20	6993 ± 2271	41.28 ± 0.20	43.04 ± 0.09
		55449	7209 ± 1367	41.48 ± 0.22	...	<40.60[c]	42.56 ± 0.18

[a]These measurements of the luminosities and widths are for the broad components of these Balmer lines.

[b]Changing-look quasar previously found by LaMassa et al. (2015) and also disused in Merloni et al. (2015).

[c]5σ upper limit assuming FWHM predicted from Hα, see Section 4.3.2.

[d]5σ upper limit assuming FWMH of 7960 km s^{-1}, see Section 4.3.2.

[e]5σ upper limit assuming FWMH of 4121 km s^{-1}, see Section 4.3.2.

[f]5σ upper limit assuming FWMH of 8920 km s^{-1}, see Section 4.3.2.

[g]5σ upper limit assuming FWMH of 4297 km s^{-1}, see Section 4.3.2.

[h]This MJD is the mean of four closely-spaced epochs of spectra that have been stacked (see discussion in Section 4.3.1).

Table 4.2. Inferred SDSS spectral properties of the changing-look quasars in our sample.

SDSS Object	MJD	$\log_{10} M_{\mathrm{BH,H}\alpha}$ $[M_\odot]$	$\log_{10} M_{\mathrm{BH,H}\beta}$ $[M_\odot]$	$\log_{10}(L_{\mathrm{bol}}/L_{\mathrm{Edd,H}\alpha})$	$\log_{10}(L_{\mathrm{bol}}/L_{\mathrm{Edd,H}\beta})$
J015957.64+003310.5[a]	51871	7.93 ± 0.10	8.02 ± 0.33	-1.6 ± 0.1	-1.7 ± 1.3
	55201	8.20 ± 0.26	....	-2.1 ± 1.6	....
J012648.08−083948.0	52163	7.96 ± 0.10	7.89 ± 0.84	-1.7 ± 0.4	-1.7 ± 0.7
	54465	....	....	....	....
J233602.98+001728.7	52096[b]	8.13 ± 0.29	8.11 ± 0.53	-2.3 ± 0.4	-2.3 ± 0.7
	55449	8.00 ± 0.30	...	-2.7 ± 2.6	...

[a]Changing-look quasar previously found by LaMassa et al. (2015) and discussed in Merloni et al. (2015).

[b]This MJD is the mean of four closely-spaced epochs of spectra that have been stacked (see discussion in Section 4.3.1).

Baryon Oscillation Spectroscopic Survey (BOSS, Eisenstein et al., 2011; Dawson et al., 2013) spectrographs (Smee et al., 2013), and compiled in the 'spAll' files produced by the SDSS spectroscopic reduction pipeline (Bolton et al., 2012). For a CL quasar to show a convincing transition, its multi-epoch spectra must clearly possess quasar-like spectral features in one epoch (power-law continuum and broad emission lines), and galaxy-like features in another epoch (absorption spectra and narrow emission lines if star-formation or nuclear activity is present). While a sophisticated method of detecting this transition in repeat spectra of each object is likely to be more sensitive to subtle changes, our current goal is to search only for the most obvious and convincing cases of CL quasars. Thus, our simple approach relies on the automated SDSS pipeline to classify each spectrum as quasar-like or galaxy-like. Specifically, using the `CLASS` spectral classification provided for each spectrum in our sample (which is based on fitting to a set of galaxy, quasar, and stellar eigenspectra, see Bolton et al. 2012), we create two subsamples: a galaxy-like sample of 2,510,060 spectra where `CLASS = 'GALAXY'`, and a quasar-like sample of 587,306 spectra where `CLASS = 'QSO'`. In both these subsamples, sky fibers have been removed using the `sourcetype` targeting keyword. Although it is well-known that these automated pipeline classifications occasionally fail to accurately classify the observed spectra, we emphasize that we are focusing on the most obvious and convincing CL quasars, for which the pipeline classifications will suffice for this initial archival search.

For each spectrum in our galaxy-like sample, we positionally match to the quasar-like sample using a 1" matching radius to identify objects with repeat spectra and disparate classifications. We impose additional quality-control conditions on this search: the difference in the pipeline redshifts between the two epochs must be $|\Delta z| < 0.01$, and the absolute value of the rest-frame time lag between the two epochs is $|\Delta t_{\rm rest-frame}| > 4$ years. These conditions remove a significant number of false-positives in which the pipeline catastrophically fails to fit the spectrum in one of the epochs. This search results in 180 pairs of repeat spectra of 117 unique objects (a few objects have more than two epochs of spectra), and we visually inspect all spectra of each of these CL quasar candidates.

From the visual inspection, we find three clear cases of CL quasars (listed in Table 4.1), which include the LaMassa et al. (2015) CL quasar (J01595+0033) and two additional new convincing cases (J01264−0839 and J2336+00172). All of these CL quasars exhibit quasar-like to galaxy-like transitions, and are at relatively low redshifts of $z \sim 0.2-0.3$ in comparison to the parent sample of SDSS quasars, which are overwhelmingly at $z > 1$ (e.g. see Figure 2 in Pâris et al., 2014). In all three of the CL quasars discovered in our search, the broad Hβ emission disappears while the broad Hα emission dims significantly (and disappears in J01264−0839), accompanied by dimming of blue quasar UV/optical continuum emission. The median seeing during the exposures of these three CL quasar candidates ranged from 1.43" to 1.93", consistent with typical values for SDSS spectra (i.e. these exposures are not strong outliers). Small differences in the seeing between exposures at this level are not responsible for the observed spectral variability (including broadening of the broad emission lines, see Section 4.3.2). We additionally find one ambiguous CL quasar where the latest epoch of SDSS spectra appears to show a galaxy-like spectrum at blue wavelengths, but is corrupted at the redder wavelengths. In Appendix A, we present additional recent non-SDSS spectroscopy which demonstrates that this object does not transition to a galaxy-like state at the epoch of the latest spectrum; this behavior instead likely stems from known instrumental issues affecting the particular fiber of the corrupted SDSS spectrum.

In the visual inspection of the multi-epoch spectra, the vast majority of the false-positives from our search were cases where the pipeline switched between `CLASS = 'GALAXY'` and `CLASS = 'QSO'` classifications in repeat spectra despite little change in the spectral properties. Often, this occurs for AGN at redshifts of $z \simeq 0.4$ in which the broad Hα emission line is redward of the smaller wavelength coverage of the SDSS spectrograph in the earlier epoch (leading to a `CLASS = 'GALAXY'` classification), but visible in the later epoch from the BOSS spectrograph due to its slightly larger wavelength coverage (leading to a `CLASS = 'QSO'` classification). As part of the visual inspection, the fiber plugging positions and targeting flags for each pair of repeat spectra were compared to ensure that there is no offset in the fiber position between the two spectra, artificially leading to more host-galaxy

emission in the SDSS spectrum. This offset can occur since some SDSS fibers were part of a SDSS program to test the redshift recovery of the spectroscopic pipeline in SDSS-III relative to that in SDSS-I/II, and are identified using the `PROGRAM = 'APBIAS'` target flag in the spectra as well as their disparate fiber plugging positions in repeat spectra. One of these objects was recovered in our search, and was removed from our sample. Aside from this offset object and the three CL quasars, all the remaining 113 candidates were rejected because our visual inspection of their repeat spectra did not reveal dramatic disappearance or appearance of broad emission lines. In Appendix B, we further discuss and show examples of the CL quasar candidates rejected in our visual inspection.

4.3 Spectral Properties of Changing-Look Quasars

In this section, we describe our decomposition of the multi-epoch spectra of our three CL quasars into host-galaxy and quasar components. We then fit the broad emission lines in the quasar components and analyze their properties. Although single-epoch broadband imaging of our CL quasars is available through SDSS, we do not compare the multi-epoch spectra to their photometry in our analysis. This is primarily because our CL quasars are spatially extended (i.e. resolved) in the imaging, and the SDSS fibers may have different diameters depending on epoch. This causes the stellar contamination in the imaging photometry to vary with aperture, complicating comparisons between the imaging and the multi-epoch spectra. Our approach to investigating the nuclear emission of our CL quasars instead relies on decomposition of the spectra to remove contamination from the host galaxy. We note that the LaMassa et al. (2015) CL quasar recovered in our search lies in the SDSS Stripe 82 footprint; image differencing light curves of its nuclear emission are presented and discussed in Merloni et al. (2015).

4.3.1 Spectral Decomposition

We decompose the quasar and host-galaxy components in the spectra from both epochs for each of the three CL quasars found in our search. For the spectral decomposition, we

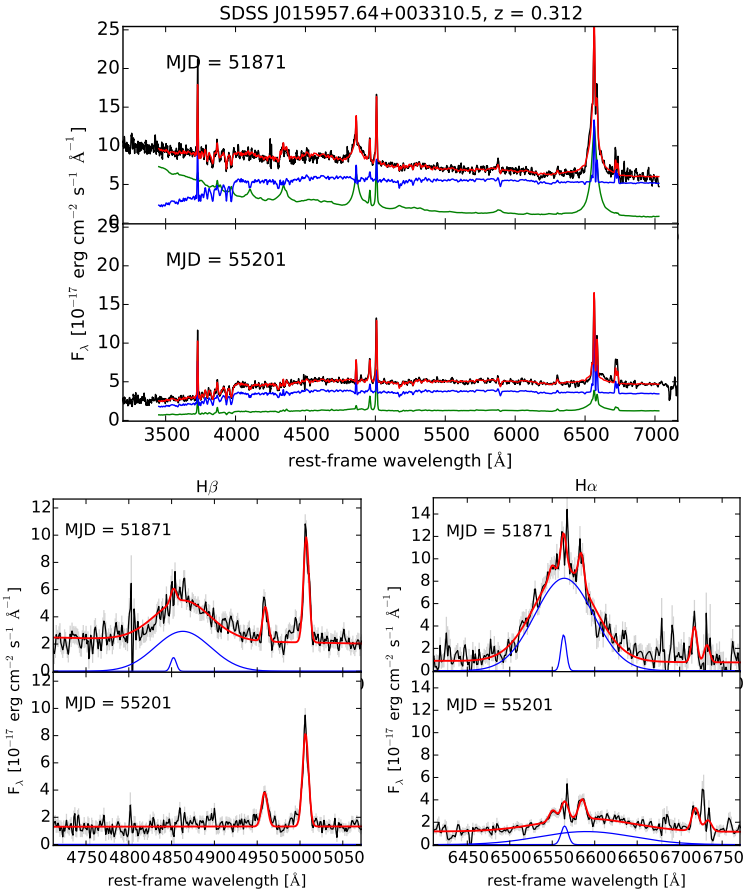

Figure 4.1: Top: Spectral decomposition for the two epochs of spectra of SDSS J015957.64+003310.5 (see LaMassa et al. 2015), in the rest-frame. The black lines are the observed spectra, and the green and blue lines are the reconstructed quasar and host-galaxy spectra from the eigenspectra decomposition, respectively. The best-fit model to the observed spectrum from the decomposition (i.e. sum of the green and blue lines) is the red line. Bottom left: Fitting of the Hβ line region in the decomposed quasar spectrum, for the two epochs of spectra. The decomposed quasar spectra are the black lines, the best-fit broad and narrow Hβ emission lines are the blue lines, and the total fits to the decomposed quasar spectra (including quasar continuum and all emission lines) are shown in red. Bottom right: Similar to the bottom left panels, but for the Hα emission lines.

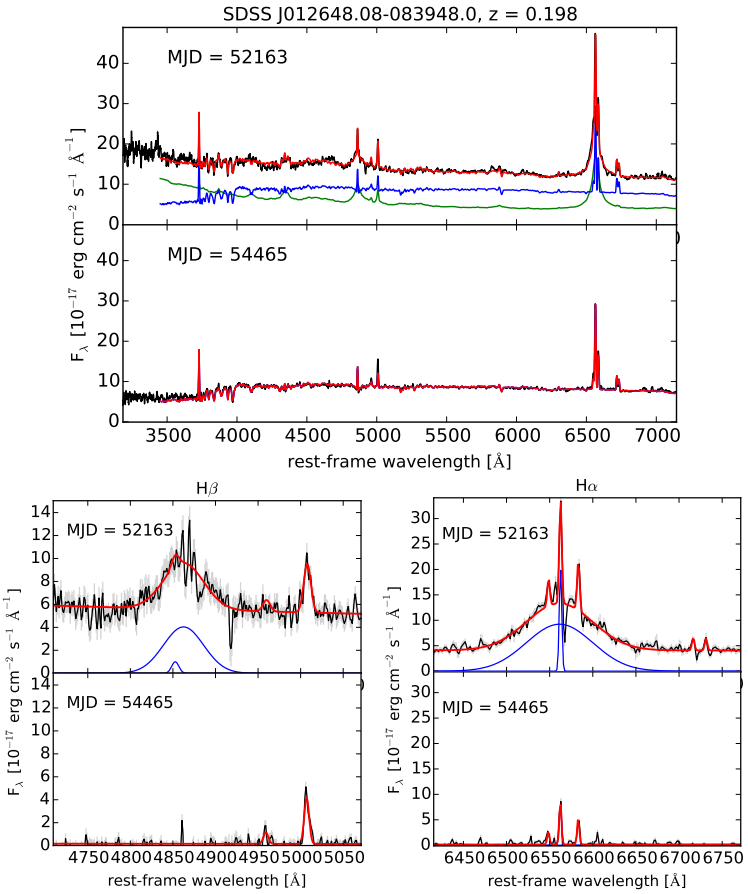

Figure 4.2: Spectral decomposition for the two epochs of spectra of SDSS J012648.08-083948.0 in the rest-frame, same format as Figure 4.1.

follow the general method of Vanden Berk et al. (2006) and Shen et al. (2015c), with only minor modifications, which is based on fitting quasar and galaxy eigenspectra. Specifically, the CL quasar spectra are each fitted using a mix of quasar and galaxy eigenspectra that are created from a principal component analysis of large samples of SDSS quasar and galaxy spectra. This decomposition method using eigenspectra differs from the approach of LaMassa et al. (2015), who instead fit a model of power-law quasar continuum emission, host-galaxy emission generated from a stellar population synthesis model, and emission lines to the multi-epoch spectra. The main advantage of our approach is that the continuum emission

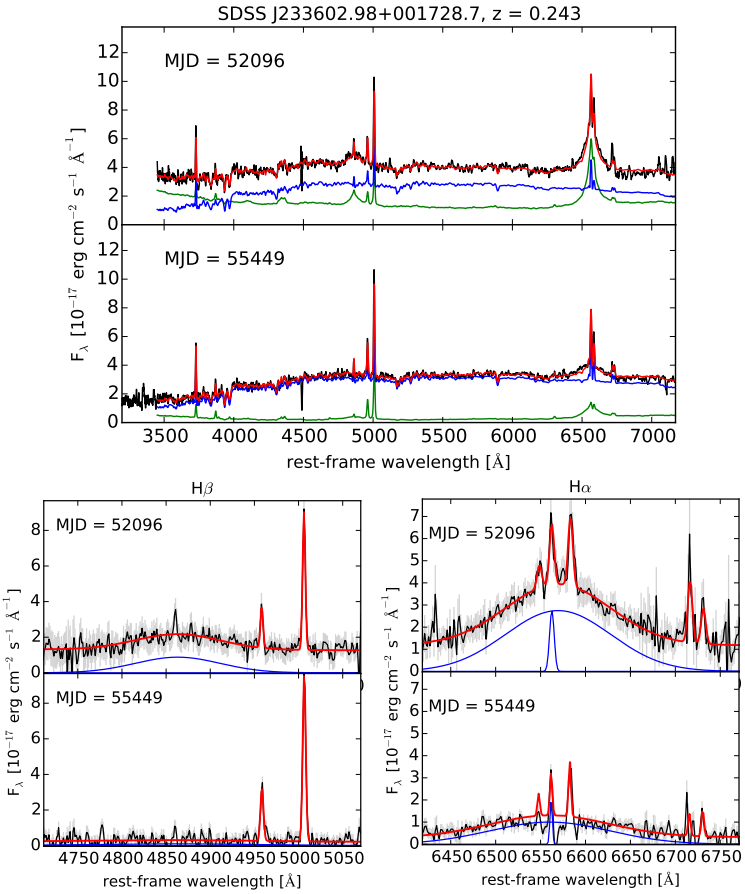

Figure 4.3: Spectral decomposition for the two epochs of spectra of SDSS J233602.98+001728.7 in the rest-frame, same format as Figure 4.1.

is fitted and decomposed empirically without having to rely on the accuracy of a power-law and stellar population synthesis models. For example, a mixture of eigenspectra can more accurately describe a galaxy spectrum consisting of stars with a continuous range of ages in comparison to the simple star formation histories assumed by stellar population synthesis models. The primary disadvantage of our approach is that because narrow emission lines are present in both the quasar and galaxy eigenspectra, separating the narrow line emission from the continuum emission is less straightforward (this does not adversely affect the broad emission lines). Although the CL quasar J0159+0033 recovered in our search was previously

discovered and analyzed by LaMassa et al. (2015), we nevertheless include it in our analysis below to demonstrate whether our independent spectral decomposition and broad emission line fitting for this object produces results that are consistent with their published values.

We first correct all spectra in our sample for Galactic extinction, using the maps of Schlafly & Finkbeiner (2011) and the Milky Way reddening law of Cardelli et al. (1989). To facilitate the spectral decomposition, we resample all our spectra and the eigenspectra to a common wavelength grid of the form $\log_{10}\lambda = 3.35 + 0.001a$, for integer a from 0 to 5,914. The wavelength coverage of this common grid is wide enough to accommodate all spectra in our sample, and is similar to the native SDSS resolution. For our spectral decomposition, we utilize the eigenspectra from the principal component analysis of ∼17,000 SDSS quasar spectra from Yip et al. (2004a), and 170,000 SDSS galaxy spectra from Yip et al. (2004b), respectively. Specifically, we fit combinations of the first five quasar and first five galaxy eigenspectra, with their amplitudes (i.e., PCA coefficients) as 10 free parameters. These fits are performed through a simple χ^2 minimization. Yip et al. (2004a,b) demonstrated that the first five eigenspectra in their PCA analysis captured 98.29% and 98.37% of the variance in their quasar and galaxy spectra samples, respectively. Not surprisingly, we find that extending the spectral decomposition to the first 10 quasar and galaxy eigenspectra did not noticeably improve the resulting fits to the observed spectra, and so we only utilize the first five in our analysis for simplicity.

Since the Petrosian radius measured in SDSS imaging for our three CL quasars are between 1.45" to 2.58", they are spatially extended (i.e. resolved). The host-galaxy and quasar contributions in each resulting SDSS spectrum are thus dependent on the fiber diameter. SDSS-I/II spectra were obtained using 3" diameter fibers, while SDSS-III (BOSS) spectra were acquired using 2" diameter fibers. For J0159+0033, we decompose the spectra from the two epochs separately because the earlier spectrum was obtained with a 3" fiber, while the later spectrum was obtained with a 2" fiber. In contrast, both spectra of J0126−0839 were obtained with 3" fibers, therefore the host-galaxy contribution should be constant between the two spectra. For this object, we decompose both epochs of spectra simultaneously and

impose the additional constraint of constant galaxy parameters between the spectra from the two epochs. Finally, for J2336+0017, a total of five epochs of SDSS spectra are available, including four early epochs (with 3" fibers) within a 2-year timespan in the observed frame during its quasar-like phase (MJD of 51783, 51877, 52199, 52525), and an epoch 9 years later with a 2" fiber. Since the spectral changes in the four early epochs of this object are relatively small, we simply use the mean spectrum of these four epochs in our spectral decomposition to achieve higher signal-to-noise, and our quoted MJD of 52096 is thus actually the mean MJD of the four early epochs. To accommodate the different fiber diameter of the early and later spectra, the galaxy parameters in the fitting are allowed to vary between the mean earlier spectrum and the later spectrum. In Section 4.4.2, we discuss the evolution in the continuum luminosity of this object over its five separate spectroscopic epochs.

The results of our spectral decomposition for each of the three CL quasars are shown in Figures 4.1 to 4.3, which display both observed epochs of each CL quasar, as well as their best-fit quasar and galaxy components from eigenspectra. Following previous conventions, we refer to the fitted quasar and galaxy spectra shown in Figures 4.1 to 4.3 as the 'reconstructed' quasar and galaxy spectra, while the 'decomposed' quasar spectra (not shown) are the original spectra with their corresponding reconstructed galaxy spectra subtracted. All of our broad emission line analysis in Section 4.3.2 is performed on the decomposed quasar spectra rather than the reconstructed quasar spectra, since this allows us to use the uncertainties on the flux densities from the original spectrum.

4.3.2 Broad Emission Line Analysis

Using our decomposed quasar spectra in both epochs for each of our CL quasars, we measure the properties of the Hα and Hβ broad emission lines to estimate black hole masses $M_{\rm BH}$ and bolometric Eddington ratios $L_{\rm bol}/L_{\rm Edd}$. Our broad emission line fitting procedure generally follows the method of Shen et al. (2011), in which the single-epoch virial $M_{\rm BH}$ estimates are based on the broad emission line Full-Width Half Maximum (FWHMs), as well as a radius-luminosity relation for the broad line region from reverberation mapping of low-redshift

AGNs. We emphasize that the narrow emission lines in the decomposed quasar spectra (observed spectrum minus the best-fit galaxy spectrum) we use for the broad emission line fitting are not equivalent to those in the original observed spectrum. This is because narrow emission lines are also present in the galaxy eigenspectra (and thus the best-fit host-galaxy spectrum), which is subtracted to obtain the decomposed quasar spectra. However, we include the narrow emission lines in our analysis below to avoid biases in fitting the broad emission lines.

For the Hα region of each object, we use the decomposed quasar spectrum and fit the local continuum emission in the wavelength windows of [6400, 6500]Å and [6800, 7000]Å to a power-law. In the Hα line wavelength window of [6500, 6800]Å, we fit for the narrow Hα component, the [N II] $\lambda\lambda$6548,6584 doublet, and the [S II] $\lambda\lambda$6717,6731 doublet, using a single Gaussian for each emission line. The redshifts of the narrow lines are constrained to be the same, and their widths are constrained to be <1200 km s^{-1}. The broad component of the Hα emission is fit with a Gaussian with width constrained to be >1200 km s^{-1}, with its central wavelength as a free parameter.

Similarly, for the Hβ region, we fit a local power-law to the continuum wavelength windows of [4435, 4700]Å and [5100, 5535]Å, and we fit emission lines in the Hβ line wavelength window of [4700, 5007]Å. In the continuum wavelength window, we include the optical Fe II template of Boroson & Green (1992) in the fit. However, for each of our three CL quasars in the dimmer galaxy-like epoch and two in the brighter quasar-like epoch (J012648.08-083948.0 and J233602.98+001728.7) , the Fe II emission is weak and the template fit is poorly constrained. Thus, the Fe II template is included in the continuum fit only for J0159+0033 in its brighter quasar-like spectral epoch. For the narrow lines, we fit single Gaussians for the narrow component of Hβ and the [O III] $\lambda\lambda$4959,5007 doublet, with widths constrained to be <1200 km s^{-1} and redshifts constrained to be the same. The broad Hβ component is fit with a single Gaussian with width >1200 km s^{-1}, and its central wavelength is a free parameter.

The above spectral fitting produced the FWHM and luminosities of the broad Hα and

Hβ components, as well as the quasar continuum luminosity at 5100Å λL_{5100}, for each epoch of our CL quasars. These measured properties of the broad emission lines are tabulated in Table 4.1, and the spectral fits are also presented in Figures 4.1 to 4.3. All uncertainties are calculated through 10^3 Monte Carlo realizations of each spectrum based on their 1σ flux density uncertainties. The spectral fitting procedure is performed for each resampled spectrum, and the uncertainties quoted for each parameter are thus the 1σ spread in the resulting distributions of resampled parameters.

Using the Hα broad emission line FWHM and luminosities from our fits (where detected), single-epoch black hole masses $M_{\mathrm{BH,H}\alpha}$ are estimated using the relation from Greene et al. (2010) of

$$M_{\mathrm{BH,H}\alpha} = 9.7 \times 10^6 \left[\frac{\mathrm{FWHM(H}\alpha)}{1000 \text{ km s}^{-1}}\right]^{2.06} \left[\frac{\lambda L_{5100}}{10^{44} \text{ erg s}^{-1}}\right]^{0.519} M_\odot, \tag{4.1}$$

based on the radius-luminosity relation of Bentz et al. (2009). To verify these Hα-based estimates, we also estimate single-epoch black hole masses based on our Hβ broad emission line fits $M_{\mathrm{BH,H}\beta}$ using the relation from Vestergaard & Peterson (2006) of

$$M_{\mathrm{BH,H}\beta} = 10^{6.91} \left[\frac{\mathrm{FWHM(H}\beta)}{1000 \text{ km s}^{-1}}\right]^{2} \left[\frac{\lambda L_{5100}}{10^{44} \text{ erg s}^{-1}}\right]^{0.5} M_\odot. \tag{4.2}$$

For J0159+0033 and J2336+0017, the broad Hβ component is not detected in the fainter galaxy-like spectrum. We provide 3σ upper limits on the broad Hβ luminosities for these two objects in Table 4.1. These upper limits are estimated in the fainter galaxy-like epoch by refitting the Gaussian broad Hβ line in 10^3 Monte Carlo resamplings of the spectrum, with the FWHM of the broad Hβ component fixed to the width predicted from the observable Hα FWHM using Equation 9 from Shen et al. (2011).

For J0126−0839, neither broad Balmer emission nor quasar continuum emission are detected in the fainter galaxy-like spectral epoch, and thus the origin of the dimming in this object is poorly-constrained. We provide a 5σ upper limit on the continuum luminosity λL_{5100} in Table 4.1, through 10^3 Monte Carlo resamplings of the spectrum. To obtain limits for the luminosities of the Balmer emission lines, we must first assume a FWHM. Therefore,

we report here the results for two different assumptions: (a) the FWHM in the dim state is the same as that in the bright state, and (b) the FWHM increases as the continuum luminosity drops in order to preserve the black hole mass, as prescribed by Equations 4.1 and 4.2 above. Since the continuum is not detected in the dim state, we can only obtain upper limits on the FWHM of Hα and Hβ of 7960 and 8920 km s^{-1}, respectively. Thus, we assume these (fixed) values of the FWHM in order to obtain upper limits on the line luminosities. The limits we obtain for cases (a) and (b) are given in Table 4.1. We emphasize that since neither the continuum nor the lines are detected in the dim state, we cannot constrain the dimming mechanism for this object as well as did for the other two objects. Therefore, neither the intrinsic dimming nor the reddening hypothesis can be excluded for J0126−0839.

We estimate the bolometric luminosity $L_{\rm bol}$ of our quasars by multiplying the continuum luminosity measured from the decomposed quasar spectra at 5100Å, λL_{5100}, by the bolometric correction factor of 8.1 from Runnoe et al. (2012). The Eddington ratio is then $L_{\rm bol}/L_{\rm Edd}$ $= L_{\rm bol}/(1.3 \times 10^{38} M_{\rm BH})$, for $M_{\rm BH}$ in units of $M_{\odot}$, and $L_{\rm bol}$ in units of erg s^{-1}. These inferred quantities are tabulated for both epochs of our CL quasars in Table 4.2. The $M_{\rm BH}$ and $L_{\rm bol}/L_{\rm Edd}$ values derived for each epoch of spectra from Hα and Hβ are consistent to within the uncertainties, validating our broad emission line fits.

4.4 Discussion

In this section, we investigate the origin of the CL quasar phenomenon using our sample. In particular, we will focus on evidence for and against variable dust obscuration, tidal disruption events, Type IIn supernovae, and intrinsic dimming of quasar emission, based on a variety of approaches. We conclude from these investigations that CL quasars are likely to be due to intrinsic dimming of the nuclear emission, as a result of rapidly decreasing accretion rates.

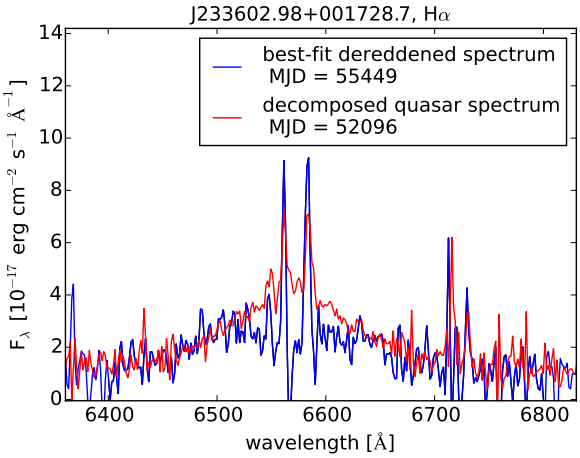

Figure 4.4: Decomposed quasar spectrum of J2336+0017 in the Hα region from the earlier, quasar-like epoch (red), compared to the dereddened decomposed quasar spectrum from the later, galaxy-like epoch (blue). Although changes in dust extinction can reasonably explain the dimming of the continuum emission in this changing-look quasar, the extinction required cannot explain the strong changes in the broad emission line (see discussion in Section 4.4.1), disfavoring an extinction origin for changing-look quasars.

4.4.1 A Dust Extinction Origin?

We assess whether extinction by an intervening dust cloud along the line of sight outside the broad line region can cause the dimming in the continuum and broad emission lines observed in our CL quasars. Following the method of LaMassa et al. (2015), we deredden the decomposed quasar spectrum in the galaxy-like epoch to match the continuum in the quasar-like epoch to assess whether the broad emission line variability can be also be explained by extinction. LaMassa et al. (2015) reported that while the dimming of the quasar continuum emission in J0159+0033 (recovered in our search) can reasonably be modeled as due to an increase in dust extinction, the changes in the broad emission lines are poorly fit by the same extinction model. While this analysis cannot be performed on J0126−0839 since the quasar continuum dimmed completely and is not observed in the galaxy-like spectral epoch,

we perform a similar analysis on the CL quasar J2336+0017.

We deredden the decomposed quasar spectrum from the galaxy-like epoch of J2336+0017, and fit an $E(B-V)$ value for which the continuum of the dereddened spectrum best matches the decomposed quasar spectrum from the earlier, quasar-like epoch of this object. This fitted value of $E(B-V) = 0.43$ is determined by minimizing the χ^2 between the two spectra (incorporating all uncertainties) in the wavelength regions outside the Hα and Hβ wavelength windows discussed in Section 4.3.2. A Cardelli et al. (1989) reddening law for the dust extinction in the host galaxy is assumed, with $R_V = 3.1$. Figure 4.4 compares the best-fit dereddened quasar spectrum from the later epoch in the Hα region to that from the decomposed quasar spectrum from the earlier epoch. Similar to the findings of LaMassa et al. (2015) for J0159+0033, it is clear that if the dimming of the continuum emission between the two spectral epochs of J2336+0017 is caused purely by dust extinction, the change in extinction required is not consistent with the observed changes in the Hα emission. Furthermore, the profile of the broad Hα component in Figure 4.4 broadens between the two epochs of spectra. In an extinction scenario, broadening of the Hα profile implies that the emission from the outer, lower-velocity regions of the broad-line region is attenuated more than emission from the inner portions. However, given that the quasar continuum from the central accretion disk is also obscured, such a configuration of the obscuring material is unlikely. These results thus disfavor a dust extinction origin for the CL quasar behavior in J2336+0017.

4.4.2 Narrow Emission Line Properties

Merloni et al. (2015) suggested that the CL quasar J0159+0033 may be a TDE that was observed serendipitously during and after a luminous flare, producing the quasar-like and galaxy-like spectra, respectively. This scenario is supported by their analysis of the long-term optical light curve of this CL quasar, which appears to show temporal evolution consistent with TDEs. However, they also present several issues with this interpretation stemming from the strong broad and narrow emission lines observed in the SDSS spectrum. Specifically, the

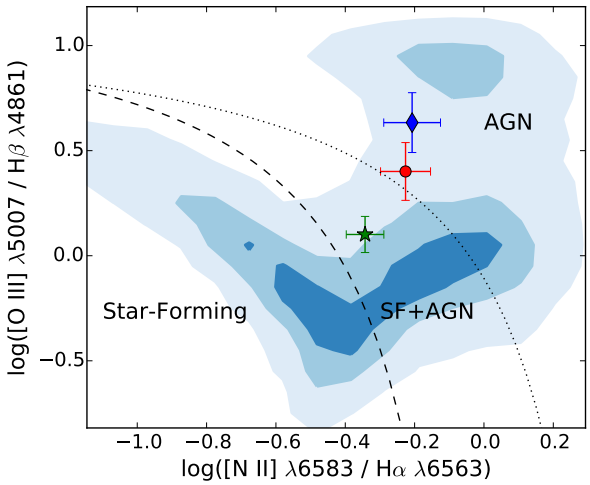

Figure 4.5: BPT diagram of the three changing-look quasars in our sample, based on the emission line ratios measured in their latest SDSS spectrum. The line ratios for SDSS J015957.64+003310.5 (red circle), SDSS J012648.08-083948.0 (green star), SDSS J233602.98+001728.7 (blue diamond), and their 1σ uncertainties are shown along with all emission line galaxies in SDSS-III DR12 (blue contours) for comparison. The BPT diagram classification schemes of Kauffmann et al. (2003) (dashed line) and Kewley et al. (2001) (dotted line) are shown. The changing-look quasars appear to exhibit emission line ratios that are consistent with AGN-like or composite (AGN and stellar) ionizing continuum emission rather than powered purely by star formation alone.

mass of gas in the broad line region inferred by Merloni et al. (2015) from the spectrum (of order $\gtrsim$100 $M_{\odot}$) is significantly more than could be provided from TDE debris. Furthermore, the possible TDE in this galaxy is unlikely to have ionized the gas producing the observed narrow lines, since the light travel time to the narrow line region (distances of kpc scales, e.g. Liu et al. 2013; Hainline et al. 2013) is $\sim 10^{3-4}$ years. Interestingly, the narrow line ratios of this CL quasar are not consistent with stellar photoionization, leaving a long-lived AGN as the most plausible power source. Here, we examine the narrow line properties for the three CL quasars in our sample, and compare them to those from AGN and TDE spectra.

Our eigenspectra-based spectral decomposition method in Section 4.3.1 does not allow a clean separation of the narrow emission lines from the underlying stellar and quasar continuum emission. We therefore utilize the stellar population and emission line fits to SDSS DR12 spectra by Thomas et al. (2013)[1] to examine our CL quasars on a classic BPT (Baldwin et al., 1981) diagram. These fits are performed using the Gas and Absorption Line Fitting (GANDALF) software described in Sarzi et al. (2006), and include Gaussian fits to a variety of emission lines to obtain line fluxes. We specifically use the [N II] λ6583 to Hα and [O III] λ5007 to Hβ narrow line ratios measured for the latest SDSS spectrum of our CL quasars (during the fainter, galaxy-like state), as shown in the BPT diagram in Figure 4.5. Figure 4.5 also indicates these line ratios for all galaxies in SDSS-III DR12 that have all four emission lines detected at $>3\sigma$ significance, as well as the BPT classification scheme of Kauffmann et al. (2003) and Kewley et al. (2001), which distinguishes galaxies with emission lines ionized by an AGN-like, stellar-like, and composite (AGN and stellar) continuum. These line ratios for J0159+0033 published by Thomas et al. (2013) are consistent with those independently determined by LaMassa et al. (2015) and Merloni et al. (2015) for the latest SDSS spectrum. Figure 4.5 demonstrates that the emission lines in our sample of CL quasars are ionized at least in part by an AGN-like continuum, disfavoring a TDE scenario. For J0126−0839, the line ratios appear to be composite, which may be due to strong star-formation in its host galaxy.

We also examine the fluxes of the narrow emission lines, focusing on the strongest narrow line, [O III] λ5007. Line fluxes reported for [O III] λ5007 from Thomas et al. (2013) for the three CL quasars in our sample range from (1.2 - 1.7) $\times$ 10^{-15} erg s^{-1} cm^{-2}, which correspond to luminosities of (1.7 - 5.3) $\times$ 10^{41} erg s^{-1} in the rest-frame. This is in strong contrast to narrow line emission observed in spectra of UV/optical TDEs, which show no or significantly fainter [O III] λ5007 emission (e.g. Gezari et al., 2006, 2009, 2012; Holoien et al., 2014; Chornock et al., 2014), further disfavoring a TDE explanation for CL quasars.

[1] www.sdss.org/dr12/spectro/galaxy_portsmouth/#kinematics

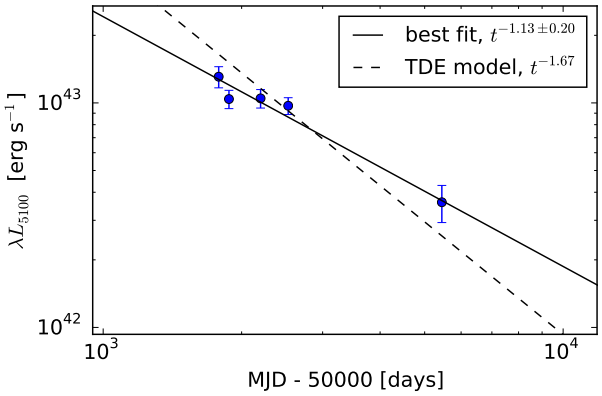

Figure 4.6: The light curve of the continuum luminosity in the decomposed quasar spectra of SDSS J233602.98+001728.7. The best-fit power-law model is shown as a black solid line, and the best-fit power-law model with spectral index fixed to the $-5/3$ value expected from tidal disruption events is shown as a black dashed line.

The faint [O III] λ5007 lines detected in these TDEs also have ratios relative to other lines that are consistent with star formation rather than AGN photoionization; this may not be surprising given the long light-travel times (10^{2-3} years) for the ionizing TDE continuum to reach the narrow line region gas. Thus, the combination of timescale arguments, narrow emission line luminosities, and emission line ratios in our sample of CL quasars all suggest that CL quasars are linked to quasar activity rather than TDEs.

4.4.3 The Nuclear Light Curve of J2336+0017

The CL quasar J2336+0017 in our sample has a total of five epochs of spectra, including four early epochs in its quasar-like state over approximately 2 years in the observed frame, and one later epoch in its galaxy-like state. Although we stacked the four early epochs of spectra in our earlier spectral analysis since the broad emission lines did not show noticeable evolution, here we decompose separately all five epochs of spectra to study the time-evolution of the quasar continuum emission. A $t^{-5/3}$ temporal evolution of the decaying continuum

luminosity is often taken to be an observational signature of TDEs, since it is the theoretical rate at which the tidal debris is expected to fall back towards the SMBH (Rees, 1988; Lodato et al., 2009; Strubbe & Quataert, 2009), although the luminosity evolution may not necessarily follow this rate (Lodato & Rossi, 2011). To test the TDE explanation further, we compare the quasar light curve from the five epochs of spectra to the expected TDE luminosity evolution.

Using the same decomposition method as described in Section 4.3.1, we measure the continuum luminosity at 5100Å λL_{5100} of the decomposed quasar spectrum for the five spectroscopic epochs of J2336+00172. Figure 4.6 presents the light curve, along with the best-fit power-law of $t^{-1.13\pm0.20}$, and the best-fit TDE $t^{-5/3}$ model. The uncertainty on this power-law index is calculated by 10^3 Monte Carlo resamplings of each point on the light curve from a Gaussian based on their 1σ uncertainties, to produce 10^3 resampled light curves. Each resampled light curve is refit, and the quoted 1σ uncertainty on the power-law index is the 1σ spread from the resampled light curves. The light curve's best-fit power-law index of -1.13 ± 0.20 is statically shallower than the $-5/3$ model predicted for TDEs, although this only weakly disfavors the TDE model due to the sparse light curve sampling and uncertainties in the models for temporal evolution of TDE luminosity.

4.4.4 A Type IIn Supernovae Origin?

Type IIn supernovae (SNe) frequently display broad H Balmer emission and blue UV continuum emission in their optical/UV spectra, which can appear qualitatively similar to AGN spectra during certain phases of their evolution (Filippenko, 1989). Thus, it may be possible that our CL quasars are actually serendipitously discoveries of Type IIn SNe. This possibility is ruled out for two of our CL quasars (J0159+0033 and J2336+0017) because broad Hα emission is still detected in their later galaxy-like spectra approximately 7 years later in the rest-frame. Furthermore, the narrow line ratios for these two objects are clearly AGN-like (see Figure 4.5), indicating the presence of nuclear activity. For J0126−0839, no broad emission lines or quasar continuum emission is detected in the later galaxy-like spectral epoch,

leaving this dimming timescale poorly constrained. Furthermore, the narrow line ratios for this object fall in the 'composite' rather than the AGN region of the relevant diagnostic line ratio diagrams, making a Type IIn SN explanation for this object somewhat more plausible at first glance. However, the Hα luminosity of J0126-0839 in the bright state ($10^{42.0}$ erg s^{-1} from Table 4.1) is approximately 1-2 orders of magnitude more than the peak Hα luminosities normally observed in Type IIn supernovae (e.g. see Figure 14 of Taddia et al., 2013). The strong Hα emission observed in Type IIn supernovae emerges several months after their light curve peaks, when the continuum emission has dimmed by several magnitudes and is red (Filippenko, 1997). In contrast, the strong Hα emission observed in the bright-state spectrum of J0126-0839 is coincident with highly-luminous and blue continuum emission. P Cygni profiles and other asymmetries often observed in the Hα line of Type IIn SNe are also not seen in our CL quasars. For these reasons, we disfavor the Type IIn supernovae scenario for J0126−0839, but this possibility cannot be conclusively ruled out because the nature of our search for CL quasars using a large data set may preferentially uncover such rare phenomena. Follow-up X-ray and radio observations of the nucleus of J0126−0839 may be useful to confirm its AGN nature.

4.4.5 Infall Timescales

Our investigations above generally disfavor TDEs, Type IIn SNe, and dust obscuration as the origin of CL quasars, and instead suggest that this phenomenon is due to intrinsic dimming of the quasar emission from rapidly decreasing accretion rates. Here, we assess whether the $\lesssim$10 year transition timescales we observe for our sample of CL quasars are consistent with the infall timescale of gas in the radiation-pressure dominated inner regions of Shakura-Sunyaev (Shakura & Sunyaev, 1973) thin accretion disks; this is also the timescale on which changes in the accretion rate are reflected in changes in the continuum luminosity. Using Equation 5 from LaMassa et al. (2015), we find that the infall timescale for our sample of changing look quasars are approximately 42, 38, and 868 years for J0159+0033, J0126−0839, and J2336+0017, respectively. Although these infall timescales are longer than

the transition timescales we observed, we note that the transition timescales observed in our CL quasars are lower limits since the multi-epoch spectra do not encompass the full transition (e.g., it is likely that the CL quasars have begun dimming before the first spectral epoch). Furthermore, LaMassa et al. (2015) also point out that magneto-hydrodynamic simulations of quasar accretion flows have suggested that the infall timescale may be a factor of a few shorter than these analytical estimates (Krolik et al., 2005), and much closer to the observed ∼10 year timescales. However, the 868 year infall timescale estimated for J2336+0017 is problematic in this interpretation, and may indicate that other processes such as thermal or dynamical instabilities may be present in the accretion flows of CL quasars.

4.5 Conclusions

The discovery of CL quasars presents a new opportunity to study the nuclear environment and structure of quasars, once the origin of this phenomenon is understood. To provide a larger sample of these objects, we performed an archival spectroscopic search in SDSS, yielding three CL quasars, including two new cases. Using this sample, we investigate the detailed properties of their quasar continuum emission and broad and narrow emission lines, with the goal of attempting to discriminate between various possibilities for the origin of this phenomenon. The primary results of our investigation can be summarized as below:

- The three CL quasars in our sample appear to show similar properties: they are luminous ($L_{\rm bol} \sim 10^{44.0-44.5}$ erg s^{-1}) quasars at relatively low redshifts ($z \sim 0.2-0.3$) that display strong dimming of the quasar continuum and the broad H Balmer emission lines over timescales of approximately 5 to 7 years in the rest-frame.

- In the two CL quasars for which the broad emission lines are detectable in both spectral epochs, the decrease in broad line luminosity coincides with broadening of the broad line widths, such that the derived black hole masses are preserved. This is consistent with a rapid change in their Eddington ratios, which decrease from $L_{\rm bol}/L_{\rm Edd} \sim 0.03-0.005$ until the broad H Balmer lines have dimmed significantly or disappeared. In one CL

quasar (J0126-0839), all quasar continuum emission and broad emission lines have disappeared below the SDSS detection limit.

- Changes in dust extinction required to match the dimming in the quasar continuum cannot account for the changes in the broad emission lines in either of our two CL quasars for which this analysis was possible, disfavoring an extinction origin for this phenomenon. Narrow emission line diagnostics show that our CL quasars all have luminous narrow lines with line ratios consistent with at least partially AGN-like ionizing emission. We argue that these narrow line properties favor a scenario in which the quasar continuum dims intrinsically over a TDE origin for this phenomenon.

If the intrinsic dimming of the quasar emission favored by our analysis is due to draining of the underlying quasar accretion disk, the CL quasar phenomenon will provide a unique new laboratory to study the accretion flow and nuclear environment in luminous AGNs. Long-term spectroscopic and multi-wavelength monitoring of the currently-known changing-look quasars can help further elucidate the origin of CL quasar transitions. For example, observations of the return of any CL quasar to a bright quasar-like state would provide additional constraints on the physical mechanism of this phenomenon as well as estimates of its duty cycle. Current multi-object spectroscopic programs and time-domain imaging surveys are well-poised to serendipitously discover many more CL quasars. For example, the Time-Domain Spectroscopic Survey (Morganson et al., 2015) in SDSS-IV will provide repeat spectroscopy of several thousand low-redshift quasars, while the Pan-STARRS 3π survey has repeated imaged 30,000 deg^2 of sky (including the SDSS imaging footprint). With future instruments and surveys such as the Dark Energy Spectroscopic Instrument (DESI, Levi et al., 2013) and the Large Synoptic Survey Telescope (LSST Ivezic et al., 2008), discovery of such rare phenomena will become more routine.

4.6 Acknowledgments

JJR thanks James R.A. Davenport for helpful discussions. JJR acknowledges support provided by NASA through Fermi Guest Investigator grant NNX14AQ23G.

Funding for SDSS-III has been provided by the Alfred P. Sloan Foundation, the Participating Institutions, the National Science Foundation, and the U.S. Department of Energy Office of Science. The SDSS-III web site is http://www.sdss3.org/.

SDSS-III is managed by the Astrophysical Research Consortium for the Participating Institutions of the SDSS-III Collaboration including the University of Arizona, the Brazilian Participation Group, Brookhaven National Laboratory, Carnegie Mellon University, University of Florida, the French Participation Group, the German Participation Group, Harvard University, the Instituto de Astrofisica de Canarias, the Michigan State/Notre Dame/JINA Participation Group, Johns Hopkins University, Lawrence Berkeley National Laboratory, Max Planck Institute for Astrophysics, Max Planck Institute for Extraterrestrial Physics, New Mexico State University, New York University, Ohio State University, Pennsylvania State University, University of Portsmouth, Princeton University, the Spanish Participation Group, University of Tokyo, University of Utah, Vanderbilt University, University of Virginia, University of Washington, and Yale University.

Based on observations obtained with the Apache Point Observatory 3.5-meter telescope, which is owned and operated by the Astrophysical Research Consortium.

Chapter 5

TIME-DOMAIN SPECTROSCOPIC SURVEY: THE PROPERTIES OF VARIABILITY SELECTED QUASARS

A multitude of wide-field multi-epoch imaging surveys have recently or will soon come online, with primary science goals of systematically exploring new discovery space in the time-domain. TDSS is an SDSS-IV eBOSS subproject primarily aimed at obtaining identification spectra of ∼220,000 optically-variable objects systematically selected from SDSS/Pan-STARRS1 multi-epoch imaging. I present a preview of the science enabled by TDSS, based on TDSS spectra taken over ∼320 deg^2 of sky as part of the SEQUELS survey in SDSS-III, which is in part a pilot survey for eBOSS in SDSS-IV. Using the 15,746 TDSS-selected single-epoch spectra of photometrically variable objects in SEQUELS, I determine the demographics of this variability-selected sample, and investigate the unique spectral characteristics inherent in samples selected by variability. I show that variability-based selection of quasars complements color-based selection by selecting additional redder quasars, and mitigates redshift biases to produce a smooth quasar redshift distribution over a wide range of redshifts. The resulting quasar sample contains systematically higher fractions of blazars and broad absorption line quasars than from color-selected samples. With a factor of ∼15 more spectra, the main TDSS survey in SDSS-IV will leverage the lessons learned from these early results for a variety of time-domain science applications.

Material from this chapter was previously published in collaboration with Scott F. Anderson, Paul J. Green, Eric Morganson, Michael Eracleous, Adam D. Myers, Carles Badenes, Matthew A. Bershady, William N. Brandt, Kenneth C. Chambers, James R. A. Davenport, Kyle S. Dawson, Heather Flewelling, Timothy M. Heckman, Jedidah C. Isler, Nick Kaiser, Jean-Paul Kneib, Chelsea L. MacLeod, Isabelle Paris, Nicholas P. Ross, Jessie C. Runnoe,

Edward F. Schlafly, Sarah J. Schmidt, Donald P. Schneider, Axel D. Schwope, Yue Shen, Keivan G. Stassun, Paula Szkody, Christoper Z. Waters, and Donald G. York in the August 2016 edition of the Astrophysical Journal (Ruan et al., 2016b), and has been reproduced here with permission of the American Astronomical Society.

5.1 Introduction

The proliferation of large-scale time-domain imaging surveys has opened up a new window into the time-variable sky. Surveys including the Sloan Digital Sky Survey (SDSS, York et al., 2000) Stripe 82 (Sesar et al., 2007), Pan-STARRS1 (PS1, Kaiser et al., 2002, 2010), Catalina Sky Survey (CSS, Drake et al., 2009), Palomar Transient Factory (PTF, Law et al., 2009), La Silla-QUEST Variability Survey in the Southern Hemisphere (Hadjiyska et al., 2012), Lincoln Near-Earth Asteroid Research survey (LINEAR, Stokes et al., 2000), OGLE I-OGLE IV surveys (Udalski et al., 2008; Wyrzykowski et al., 2014), Gaia (Gilmore et al., 2012), and future surveys such as the Zwicky Transient Facility (ZTF, Bellm, 2014) and the Large Synoptic Survey Telescope (LSST, Ivezic et al., 2008) will provide publicly available light curves for up to billions of objects over large regions of sky. Many classes of objects exhibit broadband variability at optical wavelengths, and their diverse light curves contain rich temporal information to use in exploring their astrophysics.

Spectroscopic follow-up of photometrically variable objects significantly enhances the science return on time-domain imaging surveys, by providing additional information on their physical nature and parameters that extends well beyond just object identifications/classifications and redshifts. For example, optical spectra of pulsating RR Lyrae stars discovered based on their periodic light curves provide information on their metallicities and radial velocities, enabling more accurate distance determinations and kinematic information. This is useful for probing the stellar distribution of the outer Galactic halo and discovery of halo substructures, which provides valuable insight on the formation of our Galaxy (e.g., Drake et al., 2013a). Furthermore, this spectral information is especially useful if large numbers of follow-up spectra are obtained in a systematic fashion, so that they can be mined for rare

variable objects and events. For example, the elusive sub-parsec scale evolutionary phase of merging binary supermassive black holes may be observable through predicted periodic signatures in their continuum emission using broadband light curves (e.g., D'Orazio et al., 2013; Farris et al., 2015), as well as offset broad emission lines in their optical spectra (e.g., Bogdanović et al., 2008; Eracleous et al., 2012); evidence from a combination of both light curve information (e.g., Graham et al., 2015; Liu et al., 2015) and spectra would result in a much stronger case for claims of their discovery. The large scope of current and future time-domain imaging surveys will yield of order $\gtrsim 10^7$ time-variable objects across the sky, but spectroscopy on this scale will challenge spectroscopic resources and capabilities due to the sheer number of interesting variable objects that are expected to be discovered. To this end, a systematic spectroscopic survey dedicated to follow-up of variable sources will be highly complementary, innately full of scientific insights, and immensely valuable as a training set for time-domain science from current and future multi-epoch imaging surveys.

The Time Domain Spectroscopic Survey (TDSS) is a large spectroscopic survey with the primary goal of obtaining a total of ∼220,000 single-epoch initial identification optical spectra of photometrically-variable objects (generally with >0.1 mag of variability) over 7,500 deg^2 of sky, selected based on the variability in their light curves from multi-epoch PS1 3π survey (Chambers et al., 2016) and SDSS imaging. As a subprogram of the extended Baryon Oscillation Spectroscopic Survey (eBOSS; Dawson et al., 2015) in SDSS-IV, these spectra will be obtained using the upgraded SDSS BOSS spectrograph over the full eBOSS footprint during the period of 2014-2020. TDSS targets are uniquely selected based on their flux variability amplitudes and neither on color nor detailed modeling of their light curve characteristics, providing a relatively inclusive spectroscopic sampling of the time-variable sky to complement various multi-epoch imaging surveys. Technical details of the survey plan and the target-selection method of the main TDSS program in SDSS-IV are described in Morganson et al. (2015).

In 2013-2014, SDSS-III undertook the Sloan Extended QUasar, Emission-Line galaxies, and Luminous red galaxies Survey (SEQUELS), an ancillary SDSS-III BOSS (Dawson et al.,

2013) dark-time program which is in part a pilot program for eBOSS in SDSS-IV. Since TDSS is a subprogram of eBOSS, spectra of TDSS targets were also obtained as part of SEQUELS. In this paper, we use the first 66 multi-object spectroscopic plates observed in the SEQUELS area to present early science results from these TDSS spectra, which will provide promising examples of the science enabled by TDSS in the full SDSS-IV survey. Specifically, we will first determine the demographics of our sample, which provides a ground-truth baseline for variability-selected samples since it is based on visual inspection of our spectra. We will then investigate the uniqueness and advantages of using variability-selected samples for various science applications, with the goal of informing detailed future studies on specific science questions using TDSS spectra.

In Section 5.2, we describe the target-selection method of TDSS, the TDSS spectra taken as part of the SEQUELS survey, previous SDSS spectra of sample objects in this survey area, and our visual classification of these spectra. In Section 5.3, we explore the general demographics and properties of these TDSS objects. In Section 5.4, we investigate the redshift distribution and spectral properties of quasars selected by TDSS, and discuss the unique characteristics inherent in variability-selected quasar samples. We summarize and conclude in Section 5.5.

5.2 Data

5.2.1 TDSS Target Selection

TDSS targets come from two types of observing programs: (1) a Single-Epoch Spectroscopy (SES) program encompassing ∼90% of all TDSS spectra and aimed at obtaining initial single-epoch discovery spectra of photometrically variable objects, and (2) Few-Epoch Spectroscopy (FES) programs encompassing the remaining ∼10% of TDSS spectra and consisting of various smaller projects involving multi-epoch spectroscopy of special targets. Targets for the FES programs (which include e.g., 'hypervariable' quasar and stellar samples) are selected with a variety of methods to address more specific science questions. Since we are focusing

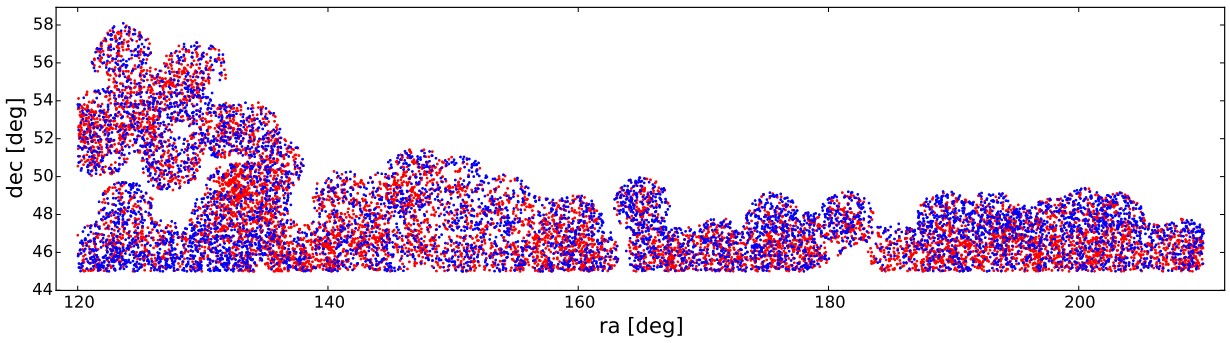

Figure 5.1: The sky area of the 66 SDSS-III SEQUELS plates used in our investigation. Positions of newly-obtained spectra of TDSS-selected objects are shown as red points, and TDSS-selected objects with previous SDSS spectra are shown as blue points. The total geometric area of these plate areas is approximately 320 deg^2 (accounting for geometric plate overlaps but not detailed tiling of targets and adjacent plates, see Section 5.2.1).

on the general properties of variable objects in this current investigation, we utilize only SES spectra, which are instead selected specifically based on their variability properties in a systematic manner. Target selection for the TDSS SES spectra in the SDSS-III SEQUELS survey we use generally follows the method detailed in Morganson et al. (2015) for the main TDSS survey in SDSS-IV, but with minor deviations; below, we only summarize the most salient aspects and highlight the small differences in targeting between these two surveys.

Photometric *griz* light curves of point sources are constructed using a combination of SDSS Data Release 9 (DR9, Ahn et al., 2012) single-epoch imaging and PS1 3π survey multi-epoch imaging. The TDSS targets are in essence selected by their (1) long-timescale ($\sim$10 years observed-frame) variability, (2) shorter-timescale ($\sim$2 years observed-frame) variability, and (3) median PS1 magnitudes. The long-timescale variability is measured as the difference in magnitude between the SDSS and median PS1 epoch magnitudes (where the SDSS magnitudes are color-corrected to match PS1 filters). The shorter-timescale variability is measured as the variance in the PS1 light curves. The median PS1 magnitudes are included in our target selection procedure primarily to take into account the increase in required vari-

Table 5.1. TDSS SEQUELS sample classifications from visual inspection of spectra

Object Type	New SEQUELS spectra	Previous SDSS-I/II/III spectra	Total spectra
Quasars	5503	4422	9925
Stars	4836	287	5123
Galaxies	292	30	322
Other/Unknown	343	33	376
Total	10,974	4,772	15,746

ability for fainter objects to enter our sample due to increased photometric uncertainties, and do not involve color information. These three parameters for each object are input into a 3-dimensional kernel density estimator (KDE) trained on the SDSS Stripe 82 variable object (Sesar et al., 2007) and standard star (i.e., those that do not measurably vary) (Ivezić et al., 2007) catalogs. The KDE assigns a probability that each object is variable, based on the efficiency E with which variable objects are selected in its region of parameter space using the training sets. Specifically, $E = \rho_{\rm var}/\rho_{\rm std}$, where $\rho_{\rm var}$ and $\rho_{\rm std}$ are the KDE density of variable objects and standard stars from the training set, in the region of the 3-dimensional parameter space occupied by TDSS candidate variables. Candidate variable objects with E above some threshold are then selected as 'variable'. Using a single E threshold over the 7500 deg^{-2} footprint of the main TDSS in SDSS-IV would result in a large number of targets at low Galactic latitudes, stemming from the dramatic increase in sky density of stellar variables in those regions. Thus, to ensure a uniform sky density of targets across the survey footprint, the E threshold is calculated independently for different sky regions (each typically 4 deg^2). However, this issue does not strongly affect our current investigation because the sky density of variable objects is nearly constant at the high Galactic latitudes

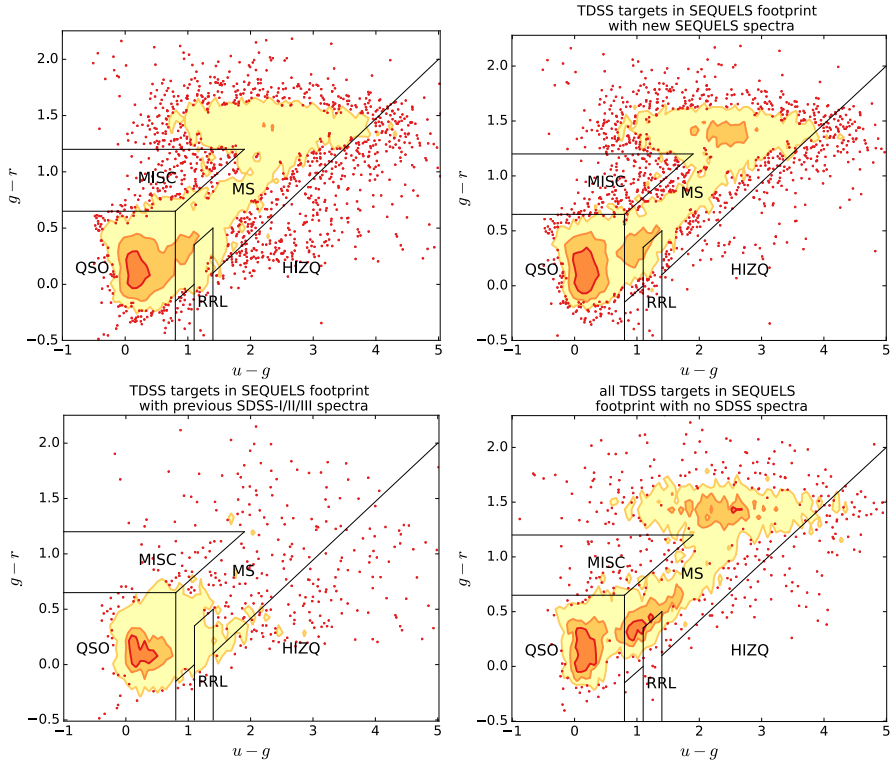

Figure 5.2: Color-color diagrams (using SDSS photometry) of all 15,746 TDSS-selected objects with spectra in our SEQUELS sky area including previous spectra (top left), all 10,974 TDSS-selected objects with new spectra in SEQUELS (top right), all 4,772 TDSS-selected objects in our SEQUELS sky area with previous SDSS-I/II/III spectra (bottom left), and all 4,735 TDSS-selected objects in our SEQUELS sky area for which spectra were not yet obtained (bottom right). Contours enclose 20%, 50%, and 90% of objects (from darkest to lightest), and the remaining 10% are shown as red points. Regions in color-space containing mostly quasars, main-sequence stars, RR Lyrae, high-z quasars, and other miscellaneous objects are labeled following the criteria in Morganson et al. (2015). The sum of the objects in the top right and lower left panels gives the top left panel. These figures show that the vast majority of TDSS-selected objects with previous SDSS-I/II/III spectra have quasar-like colors, while the new SEQUELS spectra are a mix of quasars and stars.

of the SEQUELS survey region. All targets in the SEQUELS portion of TDSS are selected using E thresholds of $E > 8.4$.

The main deviation of the TDSS targeting algorithm in SEQUELS from that of the main TDSS survey in SDSS-IV detailed in Morganson et al. (2015) is the sky density of TDSS-selected fibers. TDSS was allocated a fiber density budget of 20 deg^{-2} in SEQUELS, double the density of 10 deg^{-2} for the main TDSS survey in SDSS-IV. Since target selection is guided by these fiber-density constraints, the higher target fiber density of the TDSS sample in SEQUELS we use in this investigation generally leads to the inclusion of TDSS targets that would not meet the variability criteria to be selected in the same sky regions by the main TDSS survey in SDSS-IV. We note that SDSS plates are shared amongst several surveys, each with a number of differently-targeted samples that often contain overlaps. In particular, TDSS targets contain significant overlaps with the eBOSS CORE quasar sample, though the latter are intentionally color-selected to preferentially lie at redshifts of $z > 0.9$ (Myers et al., 2015). eBOSS aims to obtain a spectroscopic quasar sample (the eBOSS CORE sample) with high completeness and efficiency for cosmological quasar clustering studies over $0.9 < z < 2.2$, and many of these quasars are also independently selected by TDSS due to their optical variability. Spectra of TDSS targets included in the eBOSS CORE sample were also obtained, but these fibers were not charged to the TDSS fiber density budget. These TDSS/CORE-selected spectra are included in our study, and we specifically investigate the differences between the TDSS and CORE quasar samples in Section 5.4.

An additional difference in the TDSS targeting strategy between the SEQUELS sample and the main TDSS survey in SDSS-IV is that TDSS targets in SEQUELS were required to be detected in all four *griz* bands, while this requirement was relaxed in SDSS-IV to allow inclusion of more high-redshift ($z > 4$) quasars. Finally, unlike target selection in SDSS-IV TDSS, ∼30% of the earliest SEQUELS TDSS targets were not visually pre-screened via imaging data before spectra were obtained. This visual pre-screening of TDSS targets uses cutouts of SDSS imaging to remove targets whose variability is suspect due to obvious photometry problems (e.g., lying on spikes of bright stars, lying within the isophotes of a

spatially resolved galaxy, etc.). The majority (∼75%) of TDSS targets passed this visual prescreening, but the non-negligible ∼25% which were rejected highlights the importance of diligent confirmation of variability in sparsely-sampled light curves from broadband imaging surveys. On the other hand, with a much higher surface density of potential targets than fibers allotted to TDSS in SDSS-IV, we have the luxury of being conservative in such exclusions and there are likely many genuine variables among this ∼25%.

The purity of TDSS selection of variable objects (i.e. percentage of targets selected by TDSS that are indeed photometrically variable objects) was investigated in Morganson et al. (2015), who estimated that TDSS targets have purity of 98% at the 10 deg^{-2} fiber density level. At the higher 20 deg^{-2} fiber density level used here in the SDSS-III SEQUELS portion of TDSS, TDSS selects additional less-variable objects that drop the purity to 71%. However, this analysis does not take into account the visual pre-screening of our targets, where 25% of targets are removed due to likely photometry problems in the images. If we assume that these objects rejected in the visual prescreening are indeed non-variable objects, the purity of our TDSS targets in SEQUELS can thus reach 96%.

5.2.2 SDSS-III SEQUELS Spectra

Spectra of TDSS targets in SDSS-III (Eisenstein et al., 2011) were taken as part of the SEQUELS survey, and are publicly available[1] in the SDSS-III Data Release 12 and described in Alam et al. (2015). These spectra were taken with the SDSS BOSS spectrograph (Smee et al., 2013) on the SDSS 2.5m telescope (Gunn et al., 2006), with spectral resolution of $R \sim 2000$ and wavelength coverage from approximately 3600Å to 10,400Å, reduced with the SDSS-III BOSS spectral reduction pipeline (Bolton et al., 2012).

The SEQUELS spectra we utilize are from a set of 66 plates observed and reduced by June 15, 2014, and the sky coverage of these plates is shown in Figure 5.1. This does not encompass the full SEQUELS survey, and many more SEQUELS plates were observed after

[1] https://www.sdss3.org/

this date. We estimate the combined geometric plate area of this portion of the survey to be $\sim$320 deg^2 by Monte Carlo simulation, which takes into account plate overlaps. However, we caution that this plate area is approximate and in some ways misleading; some sky regions observed with one SEQUELS plate will not have complete spectroscopic coverage of all targets due to other plates overlapping the same region that had not yet been observed as part of the survey tiling plan. In the sky area of these 66 SEQUELS plates, TDSS selects 20,184 variable objects for single-epoch spectroscopy; spectra were obtained for 15,746 (about 78%) of these objects (through mid-June 2014). This sample of 15,746 TDSS spectra we use in this study consists of two parts: (1) 10,974 TDSS-selected objects with new spectra taken as part of SEQUELS, and (2) 4,772 TDSS-selected objects in our SEQUELS sky area with previous SDSS-I/II/III spectra. These two subsamples are mutually exclusive since TDSS purposely avoided targeting objects with previous SDSS spectra. To create the sample of TDSS targets with previous SDSS spectroscopy, we match all SDSS-I/II spectra from the SDSS spectrograph and SDSS-III spectra from the BOSS spectrograph (excluding SEQUELS TDSS targets) to the plate areas of the 66 SEQUELS plates we use in this study. These single-epoch TDSS spectra in SEQUELS can be selected from the SDSS DR12 databases using the `EBOSS_TARGET0` selection flag (for details on various TDSS targeting flags in SEQUELS, see Alam et al., 2015).

5.2.3 Visual Classification of Spectra

The vast discovery space in a large-scale time-domain survey has the potential to uncover large numbers of peculiar objects. To ensure that such serendipitous discoveries are not missed, we visually inspect the SDSS spectrum of each of the 15,746 TDSS-selected variable objects in the SEQUELS (including those with previous SDSS spectra in our SEQUELS sky area). Although the SDSS-III pipeline (Bolton et al., 2012) provides automated classification and redshift estimation which generally guides the visual inspection, we find that inspection of each object is crucial in identifying rare cases where the pipeline fails, and to flag especially peculiar objects. In the visual inspection, we classify and group these TDSS-selected objects

into quasar (9,925), stellar (5,123), galaxy (322), and other/unknown (376) subsamples. Out of the other/unknown objects subsample, 32 objects had genuinely interesting spectra that were not classifiable (and not simply due to low signal-to-noise), 109 objects had a blank spectrum (e.g. due to dropped fibers), 30 objects had obvious glitches in the spectrum, and the remaining 205 had low signal-to-noise ratios that made classification difficult. These subsamples are summarized in Table 5.1, and used in our investigation of the properties of these different objects.

5.3 General Properties of the TDSS Variability-Selected Sample

TDSS by design selects targets solely on the basis of optical variability, and in particular does not invoke color cuts or any other criteria that might intentionally select specific classes of astrophysical objects. Therefore, to assess the general properties of TDSS-selected objects in SEQUELS, we show in Figure 5.2 (top left) a color-color diagram of all 15,746 TDSS targets with spectra in our SEQUELS area. Since TDSS intentionally avoided targets in SEQUELS with previous SDSS spectra (except for the relatively small TDSS Few-Epoch Spectroscopy programs which are not included in this investigation), these 15,746 TDSS targets with spectra in our SEQUELS sky area are essentially the sum of the 10,974 TDSS targets with new SEQUELS spectra (top right) and the 4,772 TDSS targets with previous SDSS spectra (bottom left) also shown in Figure 5.2. The $u - g$ and $g - r$ colors for each object in Figure 5.2 and all other diagrams are derived from PSF magnitudes from SDSS photometry, in the SDSS filters (which are slightly different from the overlapping PS1 *grizy* filters). As expected, the majority of TDSS targets with spectra in our SEQUELS sky area have quasar-like colors, and the subset with previous SDSS spectra are almost entirely (93%) quasars. However, a significant number of objects are found in the stellar locus since the uniquely inclusive variability selection criteria of TDSS also selects a wide variety of variable stars.

In the SEQUELS sky area of the 66 plates we use, there are an additional 4,735 TDSS targets for which no previous SDSS spectra exist and no new SEQUELS spectra were ob-

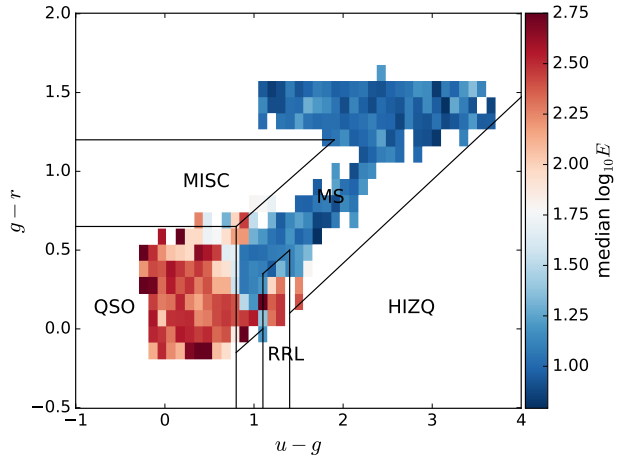

Figure 5.3: Color-color diagram of the variability amplitude E parameter defined in the Morganson et al. (2015) TDSS targeting paper, for all TDSS-selected objects with spectra in our SEQUELS sky area. Quasars and RR Lyrae stars appear to be the most variable (large E) object classes selected by TDSS, as expected.

tained through mid-June 2014, but this is primarily due to fiber allocation limits on the TDSS survey. Figure 5.2 (bottom right), shows a color-color diagram of these 4,735 TDSS targets that do not yet have spectra; this population of objects does not visually appear to be significantly different than the sample with new SEQUELS spectra (top right). This confirms that the TDSS-selected sample with spectra that we use in this study is similar to to these TDSS-selected objects without spectra. More importantly, this suggests that our conclusions on quasar and stellar properties are generally robust to survey incompleteness (e.g., the quasar redshift distribution should not significantly change with a more complete TDSS spectral sample).

The variables selection efficiency parameter E utilized in TDSS target selection can be thought of as an indirect measure of variability amplitude, since a large E for an object implies it has a high probability of being a variable, due to its large variability amplitude. Figure 5.3 shows a color-color diagram of the E parameter calculated for all TDSS-selected objects with spectra in our SEQUELS sky area as part of our KDE target selection procedure.

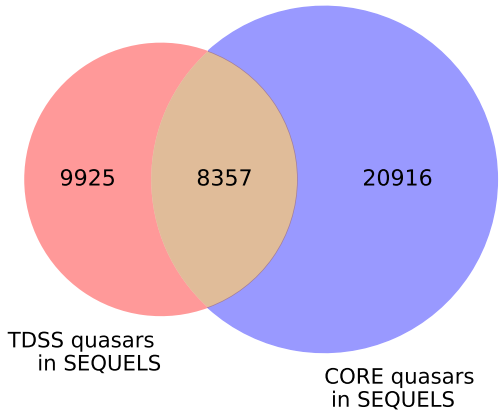

Figure 5.4: Venn diagram illustrating the TDSS and eBOSS CORE quasar samples in the SEQUELS area. In summary, there are 9,925 quasars in our TDSS SEQUELS sample and 20,916 quasars in our CORE SEQUELS sample. The intersection of these two samples includes 8,357 quasars.

Bluer objects with quasar-like colors have significantly larger E than the redder objects along the stellar locus, although the region of color-space occupied by RR Lyrae has E similar to quasars. This is qualitatively consistent with results from the analysis of SDSS Stripe 82 light curves by Sesar et al. (2007).

5.4 Quasars in TDSS

Quasars are well-known to have highly variable continuum emission in the optical and UV, displaying ∼10-30% variability in flux over long timescales. Detailed modeling of quasar light curves has shown that the broadband variability is well-described to first approximation by a first-order continuous autoregressive process (i.e. a damped random walk, e.g., Kelly et al., 2009, 2011; MacLeod et al., 2010), although small deviations from this behavior have been observed at short timescales using well-sampled light curves (e.g., Mushotzky et al., 2011; Zu et al., 2013; Edelson et al., 2014; Graham et al., 2014). This variable quasar continuum emission is believed to originate from their accretion disks, but the cause of the long-term

variability is unclear and has been suggested to originate from localized thermal fluctuations in the disks (Kelly et al., 2009; Dexter & Agol, 2011; Schmidt et al., 2012; Ruan et al., 2014a). Intriguingly, this optical variability is known to scale with quasar properties such as black hole mass and bolometric luminosity as measured from their optical spectra (Vanden Berk et al., 2004; Wilhite et al., 2008; MacLeod et al., 2010). Large samples of quasar light curves from imaging surveys can also be used to study spectral time-lags in the continuum emission (Edelson et al., 2015), and perform multi-object reverberation mapping of broad line regions (e.g., Shen et al., 2015a,b). In these and other science goals, complementary TDSS spectroscopy of these variable quasars provides crucial spectral information on their physical properties.

Morganson et al. (2015) showed that the majority of variable objects selected by TDSS have blue, quasar-like colors, although variability-based selection is known to also efficiently select a significant number of quasars with redder, stellar-like colors in comparison to color-based selection (Butler & Bloom, 2011; MacLeod et al., 2011; Palanque-Delabrouille et al., 2011). We directly compare the colors of variability-selected quasars in TDSS to color-selected quasars in the eBOSS CORE sample in SEQUELS (which uses the XDQSO method, Bovy et al. 2012), to understand the differences in the quasar populations selected by these two methods. The eBOSS CORE sample is primarily designed to yield a complete and efficient color-selected sample in the redshift range of $0.9 < z < 2.2$ for clustering measurements (Myers et al., 2015), although the targeting algorithm is free to select higher-z ($z > 2.2$) quasars. Despite the vastly different approaches in target selection for the TDSS and eBOSS CORE quasar samples in SEQUELS, the majority of TDSS-selected quasars are also selected by the eBOSS CORE algorithm; a Venn diagram showing the size of these two quasar samples is shown in Figure 5.4. Because the fibers for targets for both TDSS and eBOSS are interspersed amongst the same 66 plates, there are no differences in the observing and data reduction procedure.

Figure 5.5 (left) shows a color-color diagram of TDSS-selected quasars in our SEQUELS plate area, as well as those selected by the eBOSS CORE quasar algorithm (including those

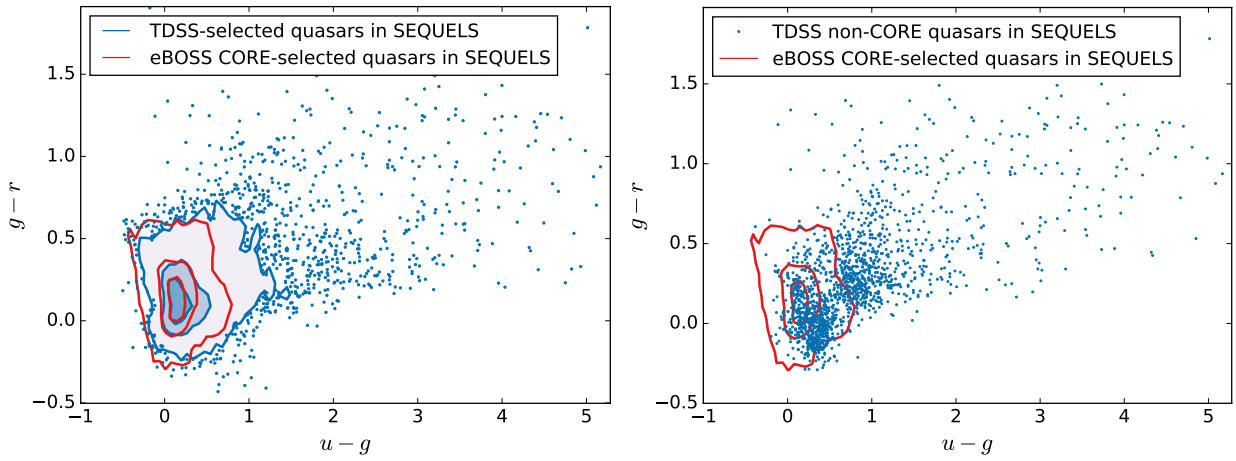

Figure 5.5: Left: Color-color diagram of TDSS-selected quasars, including those jointly selected by the eBOSS CORE sample (blue contours), in comparison to quasars in the eBOSS CORE sample (red contours). Contours enclose 20%, 50%, and 90% of the objects in each sample. The remaining 10% of objects outside of the contours for the TDSS-selected sample are plotted as blue points. There is significant overlap between these two samples, but TDSS selects an additional population of redder quasars than the CORE sample. Right: eBOSS CORE quasars with new SEQUELS spectra (red contours, same as the red contours in left panel), and TDSS-selected quasars which were not selected by the CORE sample (blue points).

with previous SDSS-I/II/III spectra). As expected, there are strong overlaps between these two samples, but the TDSS-selected sample extends further into redder colors. To better highlight these TDSS-selected quasars not selected by the eBOSS CORE quasar sample, Figure 5.5 (right) shows these TDSS non-CORE quasars in SEQUELS, plotted over the same eBOSS CORE quasar sample contours as the left panel. Again this shows a population of red quasars extending into the stellar locus ($u-g \gtrsim 0.6$) which are not selected by the color-based eBOSS CORE quasar selection, but also a clump of blue quasars centered at approximately $g-r,\ u-g = [0.0,\ 0.4]$. The redder quasars selected by variability but not color-selection can have redder colors because they may preferentially extend to higher

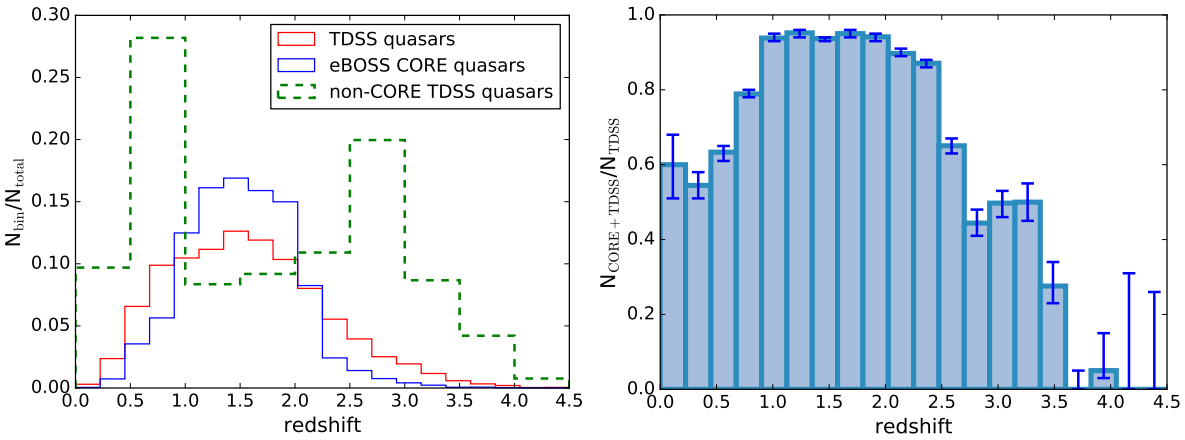

Figure 5.6: Left: Normalized redshift distribution of quasars in our SEQUELS sky area selected by TDSS (red solid), eBOSS CORE (blue solid), and the subset of TDSS quasars not selected by the CORE sample (green dashed). The inclusive variability-based approach of TDSS selects quasars with a broad, smooth redshift distribution. Right: Fraction of TDSS-selected quasars that are also selected by the eBOSS CORE algorithm, as a function of redshift. Error bars indicate the 1σ uncertainly on the computed fraction in each bin, calculated from the binomial distribution using the method of Cameron (2011).

redshifts, or they may be intrinsically redder (e.g. due to higher levels of host-galaxy dust extinction). We explore each of these two possibilities in turn below, and show that the redder TDSS quasars are in fact due to a combination of both these effects. Furthermore, we will show that the blue clump of quasars selected by variability but not colors in Figure 5.5 (right) are primarily low-redshift ($z < 0.9$) quasars outside of the targeted redshift range of the eBOSS CORE sample.

5.4.1 TDSS Quasar Redshift Distribution

Color-based selection of quasars has traditionally been a popular method to apply to large-scale imaging surveys extending into SDSS (e.g., Richards et al., 2002a; Ross et al., 2012). The resulting large samples of quasars are useful for cosmological studies of the Lyα forest

(Slosar et al., 2013; Busca et al., 2013; Font-Ribera et al., 2014), along with its various cross-correlations (e.g., Font-Ribera et al., 2012; Shen et al., 2013), the quasar luminosity function (e.g., Ross et al., 2013; McGreer et al., 2013), quasar clustering (e.g., Myers et al., 2006, 2007a,b; Ross et al., 2009), and quasar physics (e.g., Filiz Ak et al., 2013; Hall et al., 2013; Cai et al., 2014). In many of these science goals, high efficiency of selection and high sample completeness are required over large areas of sky. However, it is well-known that color-based selection can be inefficient and lead to incomplete samples in some regimes; for example, at higher redshifts ($z \gtrsim 2$), quasar colors intersect the stellar locus in optical color-space, leading to a dearth of quasars in the $2.2 \lesssim z \lesssim 3$ redshift range (Fan, 1999). This problem is exacerbated by photometric uncertainties, which further blend together the quasar and stellar populations in color space, although it has been demonstrated that probabilistic approaches to deconvolution can lead to improvements in selection efficiency (Bovy et al., 2011).

Unlike color-selection, a variability-selected sample of quasars is known to suffer less from contamination issues with the stellar locus (Schmidt et al., 2010; MacLeod et al., 2011). Since nearly all Type 1 quasars are variable in the optical (Sesar et al., 2007), our variability-selected sample is likely to be relatively complete and display a redshift distribution relatively close to the intrinsic Type 1 quasar redshift distribution. To understand the differences between our variability-selected quasar sample and a color-selected sample, we compare the redshift distribution of TDSS quasars to the eBOSS CORE sample. Figure 5.6 (top) compares the redshift distribution of TDSS-selected spectroscopic quasars in our SEQUELS plate area to those selected by the color-based eBOSS CORE quasar algorithm, using normalized histograms. These distributions for the TDSS and eBOSS CORE samples include quasars in our SEQUELS plate area that have previous SDSS spectra. Not surprisingly, the TDSS-selected sample shows a broader redshift distribution, selecting quasars at both higher ($z \gtrsim 2.2$) and lower ($z \lesssim 1$) redshifts, outside of the redshift range primarily targeted by the eBOSS CORE algorithm. Thanks to the relatively unbiased nature of variability selection, the redshift distribution of the TDSS-selected quasars in Figure 5.6 (top) is smooth and should be close to the intrinsic redshift distribution of quasars (insofar as the

redshift distribution does not strongly depend on variability amplitude, although cosmological time-dilation may affect selection of high-z quasars depending on their exact variability characteristics). Although the TDSS quasar sample used in this redshift distribution is not complete since there are TDSS-selected quasars in our SEQUELS plate area with post-DR12 spectra, the addition of these missing quasars is unlikely to introduce significant changes to this smooth redshift distribution.

Figure 5.6 (top) also shows the normalized redshift distribution for the subset of TDSS-selected quasars in SEQUELS that were not selected by the eBOSS CORE sample. This subset of TDSS-only quasars shows peaks at redshifts $z \sim 0.8$ and $z \sim 2.7$ (outside of the CORE target redshift range), but also includes additional quasars (with sky density of approximately 1.5 deg^2) in the $0.9 \lesssim z \lesssim 2.2$ range targeted by the CORE sample; this shows that variability is able to select additional quasars to complement the CORE algorithm in producing a more complete quasar sample. We note that the CORE quasar sample (20,916) is approximately a factor of 2 larger than the TDSS sample (9,925 quasars). To illustrate more clearly the complementary utility of variability-based quasar selection, Figure 5.6 (bottom) shows the fraction of TDSS-selected quasars in our SEQUELS plate area that were also selected by the eBOSS CORE sample ($N_{CORE+TDSS}/N_{TDSS}$), as a function of redshift. In this comparison, a fraction of $N_{CORE+TDSS}/N_{TDSS} = 1$ in a redshift bin indicates that all TDSS quasars in that bin were all also independently selected by the CORE algorithm, while a fraction of $N_{CORE+TDSS}/N_{TDSS} = 0$ indicates that none of the TDSS quasars in that bin were also selected by the CORE algorithm. Over the $0.9 \lesssim z \lesssim 2.2$ redshift range in which eBOSS will attempt to make CORE quasar clustering measurements (and where color selection is highly efficient and complete), the CORE XDQSO algorithm selects a very impressive 94% of the TDSS quasars. On the other hand, Figure 5.6 also shows that variability-only selection (i.e. TDSS quasars that were selected by TDSS but not CORE) accounts for more than 40-50% of TDSS quasars in some redshift bins in this particular comparison, reaffirming the complementary utility of variability-selection. Over the entire redshift range encompassed, variability selection adds about 16% (by number) to the quasars that would not have been

selected by eBOSS CORE color-selection alone (and among variability-only selections, there is additional overlap between TDSS and eBOSS selections using Palomar Transient Factory variability data; Palanque-Delabrouille et al., 2015). The additional quasars selected by TDSS at high redshifts contribute at least in part to the redder colors of TDSS quasars in comparison to eBOSS CORE quasars seen in Figure 5.5.

5.4.2 Quasar Properties with Redshift

Quasars with redder, stellar-like colors such as those seen in the TDSS-selected sample in Figure 5.5 can be in part explained if they are drawn from a population of higher-redshift quasars, but they can alternatively have intrinsically redder colors, e.g. due to continuum dust extinction in the host galaxy or substantial intrinsic line absorption. Dust extinction should not affect the continuum variability, while the redder colors can cause these objects to be misclassified as probable stars in color-based selection of quasars; quasars selected on the basis of optical variability may thus be redder than those selected by colors. Luminous quasars with heavy extinction are now commonly found based on their strong infrared emission relative to the optical (e.g., Glikman et al., 2013; Ross et al., 2014), X-ray emission (e.g., Dwelly & Page, 2006; Tozzi et al., 2006), or strong narrow emission lines with weak continuum emission (e.g., Alexandroff et al., 2013). The extinction in these type II quasars is significantly larger than many of the red TDSS-selected broad-line quasars, and they are thus too faint for TDSS to realistically target.

Since the broadband colors of quasars (e.g. in Figure 5.5) are affected by redshift effects, we show in Figure 5.7 the median colors of these quasar samples as a function of redshift. The 1σ uncertainty on the quasar color in each redshift bin is estimated through bootstrap resampling. Over the redshift range of $0.9 \lesssim z \lesssim 2.2$ targeted by the eBOSS CORE sample, the additional quasars selected by TDSS but not the CORE algorithm are systematically redder. The redder colors of these quasars are likely to be due to stronger dust extinction in their host galaxies. At higher redshifts of $z > 2.2$, the redder colors of TDSS quasars relative to the CORE sample may also be due to their intrinsically redder colors. However,

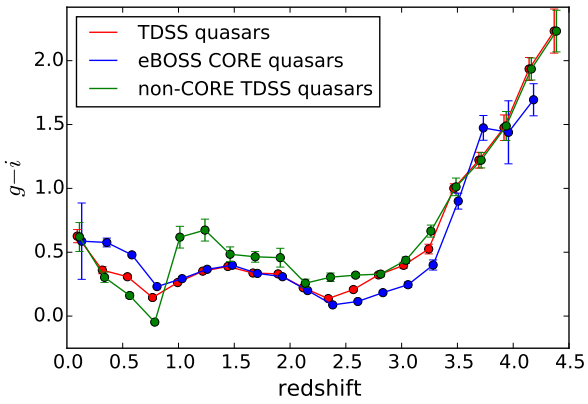

Figure 5.7: Quasar $g - i$ color from SDSS photometry as a function of redshift, for all TDSS-selected (red points), and eBOSS CORE-selected quasars (blue points) with spectra in our SEQUELS plate area. The subset of TDSS-selected quasars not selected by the CORE sample is also shown (green points). TDSS-selected quasars not selected by the eBOSS CORE algorithm in the primary CORE redshift range of $0.9 \lesssim z \lesssim 2.2$ have redder colors, likely due to stronger intrinsic dust extinction or absorption. TDSS quasars at lower- ($z < 0.9$) and higher-redshifts ($z > 2.2$) have bluer and redder colors relative to the CORE sample, respectively, likely due to selection effects in the color-selected CORE sample.

an additional effect that can cause TDSS to select redder quasars at $z > 2.2$ is that the CORE algorithm can confuse bluer quasars at these higher redshifts as lying in their targeted $0.9 \lesssim z \lesssim 2.2$ redshift range. This causes the CORE algorithm to select some bluer quasars at $z > 2.2$, which preferentially leaves redder high-redshift quasars to be selected only by TDSS. The redder quasars at $z > 0.9$ selected by TDSS but not the CORE algorithm comprise the red quasar clump centered at approximately $g - r$, $u - g = [0.2, 1.0]$ in Figure 5.5 (right), which has a long tail extending to redder colors.

Conversely, Figure 5.7 also shows that TDSS-selected quasars at low redshifts ($z \lesssim 0.9$) are instead systematically bluer than CORE quasars. This is likely to be due to the opposite of the effect described above, such that the CORE algorithm is confusing redder quasars at

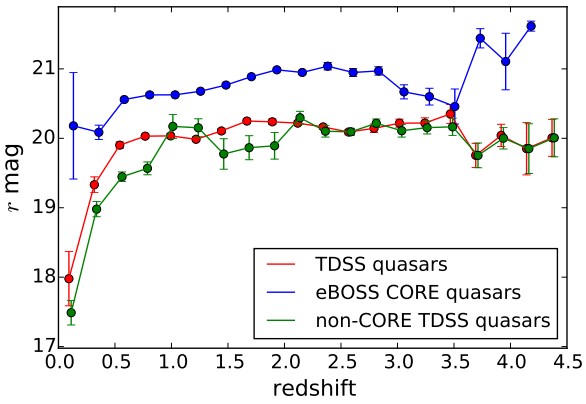

Figure 5.8: Similar to Figure 5.7, but for observed SDSS r-band magnitudes. TDSS-selected quasars are generally brighter than eBOSS CORE quasars, primarily a consequence of the requirement in the TDSS targeting method of robust detections of variability above the photometric uncertainties.

$z \lesssim 0.9$ as lying in the $0.9 \lesssim z \lesssim 2.2$ targeted redshift range, thus preferentially leaving bluer low-redshift quasars to be uniquely selected by TDSS. These bluer low-redshift TDSS quasars are the blue quasar clump centered at approximately $g-r$, $u-g = [0.0, 0.4]$ in Figure 5.5 (right) and discussed in Section 5.4. Overall, these results show that variability selection can find additional quasars that complement some color-selection approaches. Figure 5.8 shows the observed SDSS r-band magnitude of the three quasar samples, also as a function of redshift. Since TDSS target selection requires robust detection of variability in the light curves above the photometric uncertainties, TDSS quasars are preferentially brighter (by $\sim$1 r mag) than CORE quasars.

5.4.3 Unusual Quasars

Many unusual quasars are identified in the visual inspection, but have not been rigorously classified. A few examples of unusual quasars with new spectra in SEQUELS that are selected by TDSS but not by the eBOSS CORE algorithm are shown in Figure 9. We highlight below

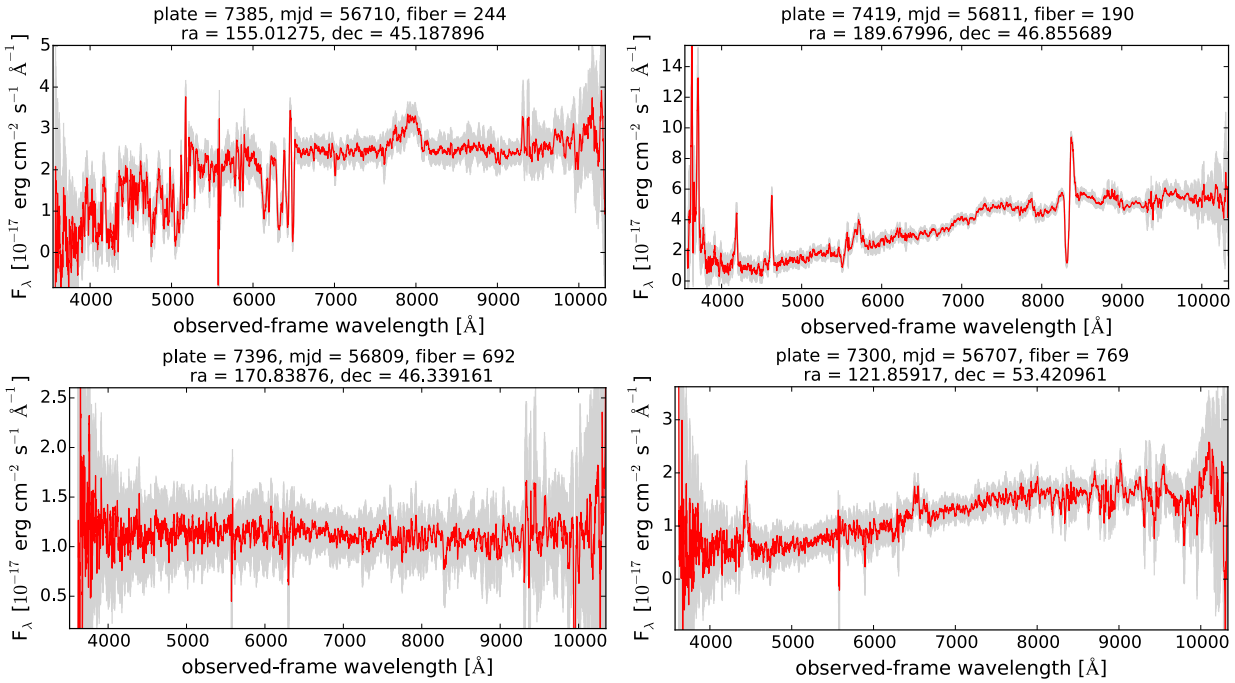

Figure 5.9: Examples of interesting quasar spectra selected only by TDSS in SEQUELS: BAL quasar ($z = 3.18$, top left), LoBAL quasar ($z = 1.99$, top right), blazar candidate with FIRST radio counterpart ($z = 0.55$, bottom left), and quasar with red continuum emission ($z = 1.33$, bottom right). The spectra are shown in red, and 1σ uncertainties in grey.

two major groups of these quasars that are likely to be significant in TDSS: broad absorption line quasars and blazars.

5.4.3.1 Broad Absorption Line Quasars

Intrinsic broad absorption lines (BALs) are observed in approximately 10-15% of quasar spectra of sufficient redshift range, almost always in high-ionization lines such as C IV, but also occasionally in low-ionization lines (e.g., Weymann et al., 1991; Hall et al., 2002; Trump et al., 2006; Gibson et al., 2008). These BALs have blueshifts of up to $\sim 0.1c$, indicative of outflowing winds launched from the accretion disk (e.g., Murray et al., 1995; Proga et al., 2000), which can affect the properties of the host galaxy (Fabian, 2012). Spectroscopic

monitoring of BAL quasars has shown that BAL troughs can vary greatly in depth (e.g., Filiz Ak et al., 2013) and even disappear (e.g., Filiz Ak et al., 2012) over timescales of years, and BAL variability has been observed on timescales as short as days (Grier et al., 2015). It may thus be expected that BAL variability could contribute to increased photometric variability in light curves of BAL quasars, leading to elevated BAL fractions in variability-selected quasar samples relative to color-selected samples. Furthermore, although BAL quasars show a wide range of physical properties, their UV/optical continuum emission is well-known to be systematically redder relative to similar non-BAL quasars (e.g., Reichard et al., 2003; Gibson et al., 2009). Since we showed in Section 5.4 that TDSS-selected quasars have redder continuum emission on average and are less biased in redshift, this may also cause variability-selected samples to contain a higher fraction of BAL quasars relative to color-selected samples, and perhaps one that is actually closer to the true intrinsic BAL fraction. We calculate and compare the BAL fractions between the TDSS and CORE quasar samples in our SEQUELS plate area for quasars at $z > 1.7$. This is performed by matching these two samples to the SDSS DR12 BAL quasar properties catalog (Pâris et al., 2017). We find that 14.1($\pm$0.5)% of TDSS-selected quasars in SEQUELS are robust BAL cases, in contrast to 9.8($\pm$0.3)% of CORE-selected quasars. The occurrence of BALs in quasars is thus 43% higher in the variability-selected TDSS sample than the color-selected eBOSS CORE sample, and is consistent with some previous inferences of the intrinsic BAL fraction (Knigge et al., 2008).

5.4.3.2 Blazars

Relativistic jets in active galaxies are not uncommon, although only a small fraction are aimed directly along the line of sight of the observer (e.g., Antonucci, 1993; Urry & Padovani, 1995). These rare jet-beamed objects are classified as blazars, and strong jet synchrotron continuum emission can dominate their optical/UV spectrum. Their optical spectra often appear as featureless power laws with weak/no broad emission lines relative to common unbeamed Type 1 quasars; this may be due to either their lack of broad line regions (in

the case of the BL Lac blazar subclass, e.g., Nicastro et al., 2003; Elitzur & Ho, 2009), or swamping of the broad emission lines by the jet continuum (in the case of the flat-spectrum radio quasar subclass; Giommi et al., 2012; Ruan et al., 2014b; D'Elia et al., 2015). Furthermore, the relativistic Doppler-boosted jet continuum emission is also highly variable, causing blazars to be systematically more variable than non-beamed quasars observed in synoptic surveys (Bauer et al., 2009c; Ruan et al., 2012). Due to this effect, the TDSS sample of quasars is likely to have a significant blazar fraction.

Blazar candidates in TDSS are identified in our visual inspection based on qualitative assessments of their broad emission line strengths; objects with strong power law-like continuum emission with weak broad emission lines are classified as blazar candidates. Blazars are well-known to almost always be strong emitters in the radio and often in the γ-rays, in strong contrast to the small $\sim$10% of unbeamed quasars that are radio loud (Ivezić et al., 2002; Baloković et al., 2012) and are typically undetected in γ-rays. A detection of any of our quasars in both of these wavelength regions provides strong support for their blazar nature. We thus match our quasars to the *Fermi* Large Area Telescope (LAT, Atwood et al., 2009) 4-year 3FGL catalog of γ-ray point sources (The Fermi-LAT Collaboration, 2015), using the 95% γ-ray source position error radii, as well as the FIRST radio survey (Becker et al., 1995b), using a 2" matching radius. We find that 26 of our visually-identified quasars are γ-ray detected, the majority of which are likely to be false-positives due to the large $10'$ angular resolution of the LAT instrument. However, 6 of these 26 possible blazars are also radio detected, and these 6 are thus highly likely to be γ-ray blazars. Our visual inspection also identified 27 BL Lac candidates with characteristic featureless power-law continuum emission, 21 of which are radio-detected in the FIRST survey. This is larger than the 16 high-confidence BL Lac candidates identified similarly by their SDSS spectrum and FIRST radio emission by Plotkin et al. (2010) in the SDSS Stripe 82 (with sky coverage of approximately 290 deg^2, similar to our SEQUELS plate area). Thus, we estimate that our variability-selected sample contains approximately a 30% higher incidence of BL Lacs than a comparable sample not selected by variability.

5.5 Conclusions

TDSS provides an unprecedented spectroscopic sample of objects selected purely on the basis on their optical flux-variability, useful for a variety of time-domain science to complement light curves from current and future large-scale synoptic imaging surveys. Using an early sample of 15,499 TDSS spectra from the SEQUELS pilot survey for eBOSS, we establish the demographics of our unique variability-selected sample (of which 63% are quasars and 33% are stars) through visual inspection of the spectra, providing a spectroscopically-confirmed ground-truth baseline for variability-selected samples. We then investigate the properties of the different classes of objects in our sample, focusing on understanding the unique advantages of using variability-selected samples for specific science applications.

We show that quasars selected by their variability in TDSS display a broad and smooth redshift distribution, complementing color-selected samples by mitigating many color-based redshift biases. For example, in comparison to the color-selected eBOSS CORE quasar sample in the redshift range of $0.9 < z < 2.2$ intended for eBOSS quasar clustering measurements, TDSS selects additional redder quasars. The redder colors of these quasars selected by variability (without regard to color) are possibly due to intrinsic dust extinction or absorption. The TDSS quasar sample also contains an elevated fraction of BAL quasars that is $\sim$40% higher than the color-selected CORE sample (and likely to be closer to the intrinsic BAL fraction). We also identify other types of peculiar quasars that may be especially common in a variability selected sample, such as blazars which we estimate to be $\sim$30% more common in TDSS than color-selected samples.

The TDSS survey is the first spectroscopic study of a large sample of objects selected using inclusive variability criteria, and our investigation here lays the groundwork for more in-depth studies of particular classes of objects for a diverse variety of science cases. An additional major science goal of TDSS is the discovery of rare objects often thought to exist but heretofore unobserved ('known unknowns'), as well as completely new classes of objects ('unknown unknowns'). Discovery of these rare objects requires robust outlier detection

in large samples; we plan on continued visual inspection of the ∼220,000 spectra in the main TDSS sample that will be observed as part of SDSS-IV over the period of 2014-2020. Looking forward, the main TDSS spectroscopic sample will provide a powerful training set for identifying and understanding the hundreds of millions of variable objects detected in future large imaging surveys, and the combination of these light curves and future planned multi-object spectrographs can be exploited to more fully realize the rich science potential in time-domain astronomy.

5.6 Acknowledgements

JJR acknowledges NASA support through Fermi Guest Investigator grant NNX14AQ23G. WNB acknowledges NSF support through grant AST-1516784.

Funding for SDSS-III has been provided by the Alfred P. Sloan Foundation, the Participating Institutions, the National Science Foundation, and the U.S. Department of Energy Office of Science. The SDSS-III web site is http://www.sdss3.org/.

SDSS-III is managed by the Astrophysical Research Consortium for the Participating Institutions of the SDSS-III Collaboration including the University of Arizona, the Brazilian Participation Group, Brookhaven National Laboratory, Carnegie Mellon University, University of Florida, the French Participation Group, the German Participation Group, Harvard University, the Instituto de Astrofisica de Canarias, the Michigan State/Notre Dame/JINA Participation Group, Johns Hopkins University, Lawrence Berkeley National Laboratory, Max Planck Institute for Astrophysics, Max Planck Institute for Extraterrestrial Physics, New Mexico State University, New York University, Ohio State University, Pennsylvania State University, University of Portsmouth, Princeton University, the Spanish Participation Group, University of Tokyo, University of Utah, Vanderbilt University, University of Virginia, University of Washington, and Yale University.

The PS1 Surveys have been made possible through contributions of the Institute for Astronomy, the University of Hawaii, the Pan-STARRS Project Office, the Max-Planck Society, and its participating institutes, the Max Planck Institute for Astronomy, Heidelberg, and the

Max Planck Institute for Extraterrestrial Physics, Garching, The Johns Hopkins University, Durham University, the University of Edinburgh, Queen's University Belfast, the Harvard-Smithsonian Center for Astrophysics, and the Las Cumbres Observatory Global Telescope Network, Incorporated, the National Central University of Taiwan, and the National Aeronautics and Space Administration under Grant No. NNX08AR22G issued through the Planetary Science Division of the NASA Science Mission Directorate.

Chapter 6

CONCLUSIONS

In this final chapter I briefly summarize and discuss the results from the various investigations contained in each chapter of this thesis. I will then describe some possible avenues for future work to explore in the exciting field of AGN variability.

6.1 Summary

In Chapter 2, I quantified the bluer-when-brighter trend of quasar spectral variability, and used it to constrain simple models of quasar variability. Although the wavelength-dependent spectral variability of quasars in the UV/optical is well-known, it has been largely ignored in constraining models of quasar accretion disks. In particular, recent revelations on quasar accretion disk sizes and characteristic timescales of variability have led to toy models of inhomogeneous accretion disks with large temperature fluctuations as the origin of quasar variability. In this chapter, I tested whether these models are consistent with the observed spectral variability of quasars. Using SDSS repeat spectroscopy of quasars, I perform a careful spectrophotometric recalibration to measure a composite wavelength-dependent quasar variability amplitude. I then compared these observations to predictions of the wavelength-dependent spectral variability from inhomogeneous disk models and accretion rate fluctuations in thin disks. I showed that strongly inhomogeneous disks with large temperature fluctuations are able to reproduce the observed spectral variability. This work is significant because these inhomogeneous disk models are the first to be able to reproduce not only the observed spectral variability, but also accretion disk sizes and UV spectral excess in quasars.

In Chapter 3, I investigated the origin of the 'transition blazars' phenomenon. Blazars are classically classified as BL Lac objects or Flat-Spectrum Radio Quasars that correspond

to low- and high-accretion rate states, respectively. This classification is based on the equivalent widths of the broad emission lines in their optical spectrum. However, a few blazars have been observed to puzzlingly transition between these two classifications, and the origin of this phenomenon is unclear. In this chapter, I searched for a sample of transition blazars in archival repeat SDSS spectra to understand why their transitions occur. I discover 6 cases of transition blazars, and show that their broad emission line strengths are anti-correlated with continuum flux. This is the opposite to the behavior expected from accretion rate fluctuations, and instead suggests that the transition blazars are FSRQs with especially strong beaming. The strongly-beamed continuum swamps the broad emission lines, occasionally causing them to disappear and reappear, causing the transitional phenomenon. This interpretation is supported by archival photometric light curves of the transition blazars, which show continuum variability even stronger than normally observed in blazars; this is further suggestive of strong beaming of the jetted continuum emission. This work suggests that some high-z BL Lacs may in fact be strongly-beamed FSRQs, thus giving credence to claims of a negative redshift evolution of BL Lacs.

In Chapter 4, I investigated the origin of the recently-discovered 'changing-look quasars' phenomenon. Although quasars are expected to transition between luminous quasar states and low-luminosity AGN (or quiescent galaxy) states on timescales of 10^{4-5} years, CL quasars are observed to fade into quiescence on surprisingly short timescales of just a few years. Due to these inconsistencies, the origin of this new phenomenon is debated, and suggestions have included rapid changes in accretion rate, variable dust obscuration, tidal disruption events, and Type IIn supernova. In this chapter, I performed the first large systematic search for CL quasars using archival repeat SDSS spectroscopy to characterize their properties. I discovered two new changing-look quasars, and recover a third discovered previously. I showed that the fading of the continuum and broad emission lines in CL quasars is consistent with rapidly decreasing accretion rates (by factors of $\gtrsim$2.5), while disfavoring changes in intrinsic dust extinction and transient tidal disruption events or supernovae. The results from this chapter are a key first step to establishing the origin of this phenomena, which can be used to study

the physics of AGN accretion state transitions (see Section 6.2.2), and the role of AGN feedback in galaxy evolution (see Section 6.2.3).

In Chapter 5, I turned to the future of variability studies of AGN with the advent of large-scale time-domain imaging surveys. Surveys such as the ZTF and LSST will discover a few $\times 10^7$ variable objects, including new and rare time-variable phenomena. At the magnitude range of these deep multi-epoch surveys, AGN will constitute the majority of variable objects discovered. It is thus imperative that we understand the science enabled through variability-selected samples of AGN. In this chapter, I utilized spectra from TDSS, the first systematic spectroscopic survey of variable objects, to understand the unique properties of variability-selected quasars. I showed that variability-selected quasars complement color-based selection by selecting additional redder quasars, resulting in a smooth redshift distribution. Furthermore, variability selection yields higher fractions of peculiar AGN such as broad absorption line quasars and blazars. The results from this chapter will inform the science enabled by the massive samples of variability-selected quasars discovered in current and future time-domain imaging surveys.

6.2 Future Work

6.2.1 Are Changing-Look Quasars Actually Tidal Disruption Events?

The recent discovery of 'changing-look' (CL) quasars presents potential challenges to our understanding of accretion onto SMBHs (LaMassa et al., 2015). Repeat optical spectroscopy of this new class of objects shows dramatic transitions from luminous broad line quasars into quiescent galaxies or low-luminosity AGN (e.g. see Figure 4.1). I showed in Chapter 4 that the dramatic disappearance of nuclear emission is consistent with a drop in the SMBH accretion rate (e.g., Ruan et al., 2016a; Runnoe et al., 2016), analogous to spectral state transitions observed in X-ray binaries. However, these changes are observed to occur over surprisingly short timescales of just a few years, a factor of $>10^4$ faster than both theoretical expectations and scaling spectral state transition timescales in X-ray binaries to $10^8 M_\odot$ SMBHs (Done &

Gierliński, 2005; Sobolewska et al., 2011). This inconsistency potentially indicates a major breakdown in our understanding of SMBH accretion, and motivates alternative explanations for the rapid disappearance of nuclear emission in CL quasars.

Tidal disruption events (TDEs) are an attractive alternative interpretation for the CL quasar phenomenon (Merloni et al., 2015). In this scenario, the unexpectedly rapid dimming of nuclear emission in CL quasars over a few years is *not* due to a sudden shutdown of accretion in a persistent quasar, but is instead the fading of a months-long optical/UV flare from the tidal disruption of a star by the central SMBH. This TDE interpretation for CL quasars has previously been disfavored for two primary reasons (although new revelations about the properties of TDEs have now reopened this debate). Firstly, available photometric light curves of fading CL quasars typically do not show a transient flare, but instead the fading nuclear emission appears to transition from a prolonged bright state into quiescence (see Figure 6.1). However, the more recent discovery of a decade-long TDE (Lin et al., 2017), in which the transient flare persisted in a bright state for >10 years, suggests that CL quasar light curves may indeed be well-described by a prolonged TDE flare. Secondly, CL quasar host galaxies often display narrow emission line ratios indicative of AGN activity, while TDE host galaxies do not. However, TDEs are now being discovered in AGN host galaxies (Blanchard et al., 2017; Tadhunter et al., 2017), further blurring the line between the AGN accretion shutdown and TDE interpretations for the CL quasar phenomenon. It is entirely possible that the rapid disappearance of nuclear emission in CL quasars is actually due to the fading of prolonged TDE flares in AGN host galaxies. An observational test of whether the CL quasar phenomenon is due to TDE flares or the rapid shutdown of AGN accretion is thus urgently needed.

Using my approved Gemini-N GMOS imaging program, I will conduct a straightforward test of the origin of CL quasars by determining whether the nuclear luminosities of CL quasars were quasar-like $\sim 10^{4-5}$ years ago. If we can determine that CL quasars were luminous quasars in the recent past, this would strongly support the view that the observed disappearance of nuclear emission is due to the shutdown of accretion in a quasar. Conversely,

if we can determine that CL quasars were relatively quiescent $\sim 10^{4-5}$ years ago, this would instead suggest that the observed disappearance of nuclear emission was a fading TDE-like nuclear flare. To determine the nuclear luminosity of CL quasar host galaxies $\sim 10^{4-5}$ years ago, I will conduct a search for 'voorwerpjes' around faded CL quasars. Voorwerpjes are emission line regions that extend up to ∼20 kpc from currently-quiescent galaxies, and were photoionized by past quasar activity in the host galaxy (e.g., Keel et al., 2017). Because the quasar faded to a quiescent state, strong [O III] λ5007 emission from the voorwerp is left as a photoionization echo. For example, the canonical Hanny's Voorwerp lying 15 kpc from the quiescent galaxy IC 2497 has been shown to be photoionized by past quasar activity in IC 2497 (with ionizing luminosity of $\sim 10^{45}$ erg s^{-1}), $\lesssim 10^5$ years ago based on the light travel time (i.e. distance) to the nucleus of IC 2497 (Lintott et al., 2009; Schawinski et al., 2010). The host galaxies of the CL quasars in my sample already show extended voorwerp-like structures in SDSS and Pan-STARRS images (Figure 6.2), but higher-resolution imaging is required for confirmation.

As a first step to determining the nuclear luminosities of CL quasars $\sim 10^{4-5}$ years ago, I will obtain GMOS *gri* broadband imaging of a sample of 4 CL quasars to search for voorwerpjes around their host galaxies. Voorwerpjes emit strongly in [O III] due to photoionization by the now-faded quasar continuum, and will thus stand out in the broadband filter in which the redshifted [O III] emission falls. At the redshifts of my CL quasars ($z \sim 0.2$ - 0.3), voorwerpjes will be luminous in r-band images in comparison to g- and i-band images. This technique based on detecting strong [O III] emission in broadband imaging was used by Keel et al. (2012a) to discover 19 voorwerpjes in SDSS around local galaxies that were photoionized by previous quasar activity. Although SDSS and Pan-STARRS imaging of our CL quasars already show kpc-scale extended features indicative of voorwerpjes (Figure 6.2), the higher redshifts of CL quasars demand imaging with higher spatial resolution for confirmation.

If my higher-resolution images confirm the existence of voorwerpjes around CL quasar host galaxies, I will propose for follow-up GMOS IFU observations in a future call for pro-

posals. Spatially resolved IFU spectroscopy will enable me to determine the past nuclear luminosity of each CL quasar through ionization balance of recombination lines in each voorwerp. This strategy closely follows that of Keel et al. (2017), who successfully traced the nuclear luminosities of 8 quiescent galaxies with voorwerpjes over timescales of $\sim 10^{4-5}$ years based on GMOS IFU spectra.

The four objects in my sample are the four currently-known faded CL quasars (the voorwerpjes search is best done in the faint-state) that have well-characterized properties from their optical spectra (including black hole masses and Eddington ratios), from LaMassa et al. (2015), Ruan et al. (2016a), and Runnoe et al. (2016). Although each of these four objects in my sample displays properties similar to some TDEs, I highlight two objects in particular that are of extreme interest. Firstly, Merloni et al. (2015) examined the SDSS spectral and light curve properties of the CL quasar J0159+0033, and showed that they are similar to commonly observed properties of TDE flares. Secondly, Ruan et al. (2016a) showed that the nuclear emission in the CL quasar J0126-0839 disappeared completely, leaving no evidence of a low-luminosity AGN in its host galaxy. This behavior is also suggestive of a TDE-like transient nuclear flare. The remaining two CL quasars in our sample are J1011+5442 (see Figures 1, 2, and 3) and J2336+0017, both of which are candidate prolonged TDE flares in galaxies with low-luminosity AGN.

6.2.2 Probing AGN Accretion State Transitions with Changing-Look Quasars

The evolution of massive galaxies is thought to be dramatically affected by feedback processes involving accretion onto their central SMBHs, but details on the exact feedback mechanism and energetics are still poorly understood. Current theories suggest that accretion disk winds in luminous quasar phases can drive outflows that expel star forming gas from the host-galaxy ('quasar-mode' feedback), while jets in low-accretion rate states can inject kinetic energy to further prevent star formation ('radio-mode' feedback). Understanding how AGN feedback operates in high- and low-accretion rate regimes would benefit enormously from direct observations of accretion state transitions in AGN, analogous to the rich phe-

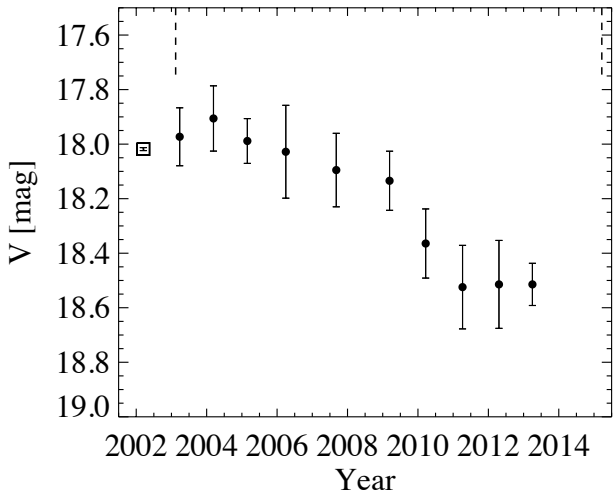

Figure 6.1: Light curves of CL quasars cannot unambiguously discriminate between models for the origin of CL quasars. The photometric light curve of the CL quasar J1011+5442 from Figure 6.1 suggests that the nuclear emission fades from a prolonged high-luminosity state (Runnoe et al., 2016), but cannot rule out the interpretation that this fading is from a prolonged TDE flare. I will determine the nuclear luminosity of this CL quasar $\sim 10^{4-5}$ years ago using voorwerpjes around the host galaxy. This will discern whether the observed disappearance of nuclear emission in this object was the fading of a transient TDE-like nuclear flare, or the surprisingly rapid fading of a persistent quasar into a low-luminosity AGN state.

nomenology now commonly observed in X-ray binary spectral state transitions. However, simple estimates traditionally suggest that the timescale for accretion state transitions in AGN is $\sim 10^{4-5}$ years, and are thus not directly observable on human timescales (Done & Gierliński, 2005; Sobolewska et al., 2011).

Previously, transitions of luminous quasars to quiescent states in individual objects have only been indirectly inferred from extended emission line clouds discovered near seemingly quiescent galaxies. For example, the Hanny's Voorwerp cloud lying 15 kpc from the galaxy IC 2497 has been shown to be photoionized by past quasar activity in IC 2497, approximately

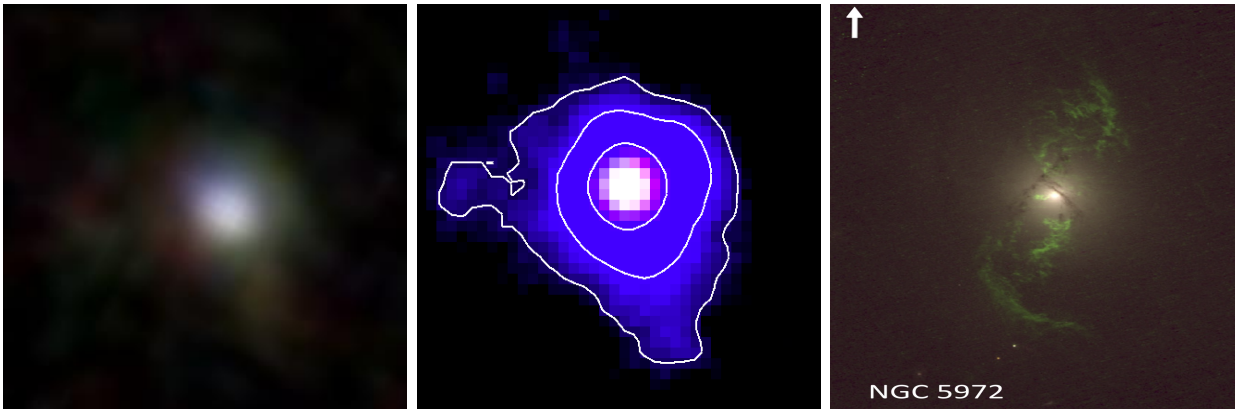

Figure 6.2: CL quasars already show extended kpc-scale structures indicative of voorwerpjes. *Left:* SDSS composite *gri* image of the CL quasar J1011+5442 from Figures 6.1 and 6.2, spanning an approximately 3" x 3" field of view. The marginally-resolved host galaxy displays extended features indicative of AGN-photoionized voorwerpjes, visible on the approximately 1.5" scale of the seeing (6 kpc physical scale). *Center:* Pan-STARRS composite *gri* image of this CL quasar also shows similar extended voorwerp-like structures on kpc scales. *Right:* A *HST* imaging example from Keel et al. (2012b) of a voorwerp (green) around a faded quasar of the sort that might be revealed in the higher-resolution Gemini images.

10^5 years ago (Lintott et al., 2009; Schawinski et al., 2010; Keel et al., 2012a). Deep Chandra observations of the nucleus of IC 2497 show the current presence of not only a very low-luminosity AGN (with $L_{\rm X} = 10^{40.7}$ erg s^{-1}), but also an extended X-ray bubble of diffuse gas (Sartori et al., 2016). This kpc-scale gas bubble with energy of 10^{54-55} erg could be a relic of galactic superwind shocks driven by previous quasar activity, or inflated by injection of kinetic energy from the current low-luminosity AGN (Figure 6.3). Direct X-ray observations of a transition between quasar and low-luminosity accretion states in an AGN would reveal the stage at which such a bubble forms during the transition, thus providing clues to its origin and its effects on the host-galaxy.

CL quasars provide exciting new opportunities to understand AGN physics and feedback,

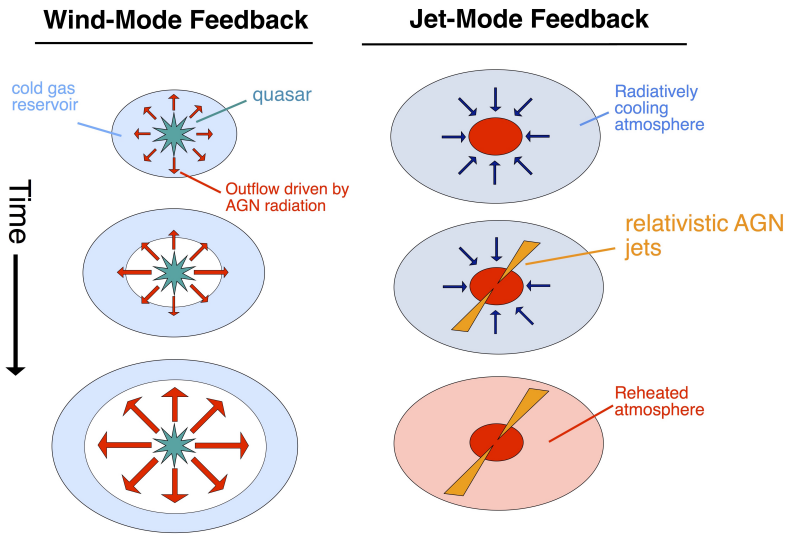

Figure 6.3: Current models of AGN feedback invoke two distinct feedback modes, but these models are observationally uncertain. At high-accretion rates, accretion disk winds during luminous quasar phases may drive outflows that expel star-forming gas (left). At low-accretion rates, relativistic jets may inject kinetic energy into the ISM to prevent star formation (right). However, there is still little observational evidence that both these feedback modes operate to suppress star formation over cosmic time. Figure adapted from Alexander & Hickox (2012).

assuming that this phenomenon is caused by rapid accretion rate drops in quasars. To this end, I will use X-ray observations from my approved *Chandra* Cycle 18 program that will obtain 7 to 33 ks ACIS (69 ks total) exposures of a sample of 5 confirmed CL quasars, each of which have undergone dramatic dimming in repeat SDSS spectroscopy over the past 2-10 years. The main scientific questions I will address with these observations are:

1. *What is the long-term accretion state of changing-look quasars?* Although X-rays are the best and most direct probe of accretion state, a faint-state X-ray luminosity is currently known only for a single CL quasar, SDSS J0159+0033 (LaMassa et al., 2015). For at least one known CL quasar, careful modeling of the latest optical spectrum shows that the broad emission lines and AGN continuum have faded away completely; X-ray observations are thus

required to tell if low-luminosity AGN activity still persists. My exposures from this program will provide a first measurement of the faint-state X-ray luminosity for a sample of confirmed CL quasars, at a 10-count detection sensitivity of $L_{\rm X}(2-10\ {\rm keV}) = 10^{42}$ erg s^{-1} (i.e. a very low-luminosity AGN). This X-ray information will be accompanied by contemporaneous optical photometry and spectra (from which black hole masses, Eddington ratios, etc. can be derived), providing at least strong $L_{\rm X}$ and $\alpha_{\rm ox}$ constraints at the 10-count level. If the faint-state X-ray luminosities of my CL quasars are similar to J0159+0033 (the only CL quasar currently with X-ray observations in its faint-state), our exposures will yield 100 counts, which will additionally provide X-ray photon index Γ and absorbing column constraints to definitively rule out dust obscuration. Nevertheless, a lower or null-detection would perhaps be the most exciting outcome, confirming in X-rays the discovery of the first luminous quasars to directly transition into quiescent galaxies.

2. *Do accretion state transitions in AGN resemble those in X-ray binaries?* Observations of similar spectral state transitions in X-ray binaries now show that the dramatic decrease in accretion rate corresponds to the disappearance of soft thermal accretion disk emission and the emergence of hard Comptonized jet emission (Done et al., 2007). However, the few-years timescales observed for AGN transitions are a factor of $\gtrsim 10^4$ shorter than predicted from X-ray binaries, suggesting that this analogy may not directly scale with black hole mass. X-ray observations from my program will test this analogy through direct comparisons of the SED properties between AGNs and X-ray binaries in both their luminous and faint states. Specifically, using the 2 objects from my sample with previous X-ray detections in their luminous quasar state (plus one additional object with an approved *Chandra* Cycle 17 observation), I will compare their $\alpha_{\rm ox}$ values pre- and post-transition to those predicted from rescaling the SEDs of X-ray binaries in these different accretion states (e.g., Sobolewska et al., 2011). With even a 10-count detection, the predicted decrease of $\Delta\alpha_{\rm ox} \sim -0.5$ is significantly larger than the uncertainties on $\Delta\alpha_{\rm ox}$ of $\sim$0.1. If I observe this predicted dramatic decrease in $\alpha_{\rm ox}$, this would indicate that CL quasars may indeed be well-described by the standard picture of X-ray binary spectral state transitions.

3. *How can we best probe AGN feedback with changing-look quasars?* My observations will assess the suitability of these CL quasars for future quality X-ray spectroscopy. Such a spectrum can reveal the presence and energetics of a hot gas bubble in the host galaxy, similar to that observed in the fading AGN IC 2497. The ability to constrain the stage at which a hot bubble forms during AGN transitions can distinguish whether it originates from quasar-driven winds or the emergence of a jet. Based on the *Chandra* X-ray fluxes of our sample of CL quasars, I intend to select a suitable object (e.g. in a low-luminosity state but with a sufficient count rate) for a future program to obtain a quality X-ray spectrum of an AGN (using *XMM* or *Chandra*) after its accretion state transition, to probe feedback mechanisms. Even with the proposed data in Cycle 18, I would be able to construct a stacked X-ray spectrum for the sample ensemble, as an initial feedback probe.

6.2.3 Measuring the High-z $M_{\rm BH} - \sigma_\star$ Relation

The local $M_{\rm BH} - \sigma_\star$ relation between SMBH masses and stellar velocity dispersion in their host galaxy bulges is commonly thought to be produced by AGN feedback, and this relation is a benchmark constraint for feedback models. Cosmological simulations of galaxy formation with SMBH growth ubiquitously hand-tune their sub-grid models of AGN feedback to match the observed local $M_{\rm BH} - \sigma_\star$ relation. However, the numerous feedback parameters in these models (e.g. feedback energetics during wind-mode and jet-mode feedback) are poorly-constrained by observations.

Beyond the local $M_{\rm BH} - \sigma_\star$ relation, an even more powerful observational constraint on models of AGN feedback is the *redshift evolution* of the $M_{\rm BH} - \sigma_\star$ relation. Simulations of galaxy formation employing different models of AGN feedback currently disagree on how this relation changes at $z > 0$: at fixed $M_{\rm BH}$, simulations have predicted that $\sigma_\star$ will either increase (e.g. Robertson et al., 2006), decrease (e.g. Hopkins et al., 2009), or stay constant (e.g. Taylor & Kobayashi, 2016). Direct measurements of the $M_{\rm BH} - \sigma_\star$ relation as a function of redshift are necessary to distinguish amongst these models and inform sub-grid implementations of feedback in simulations (see Figure 6.4).

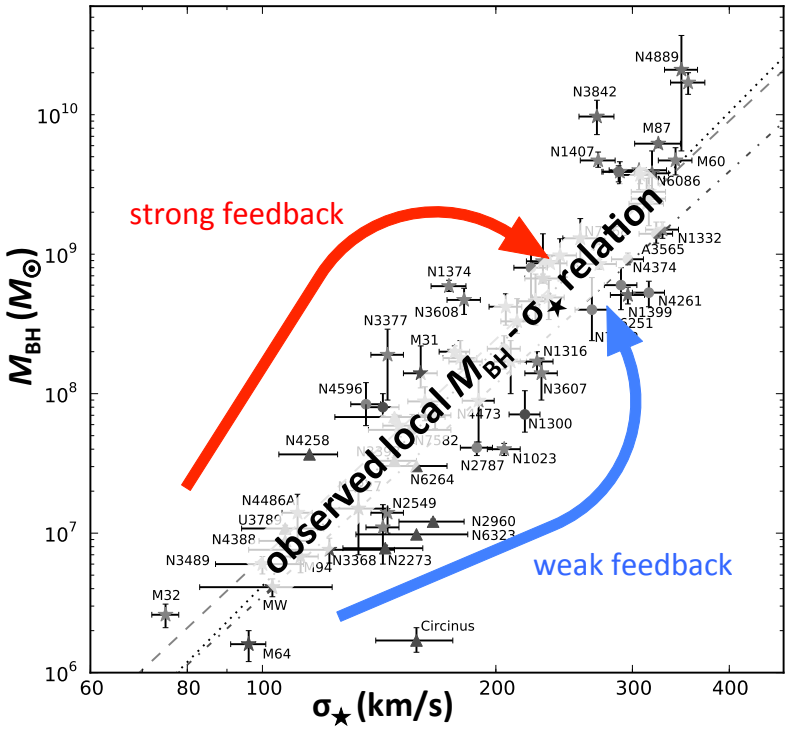

Figure 6.4: Measuring the $M_{\rm BH}-\sigma_\star$ relation at high-z will reveal how AGN feedback produces the observed local relation. As SMBHs and galaxies grow over cosmic time, the strength of AGN feedback dictates which path the galaxy will take up the $M_{\rm BH}-\sigma_\star$ relation before landing on the local relation (Volonteri, 2012). Weak feedback will allow the stellar bulge to grow unchecked, leading to under-massive SMBH masses at high-z (blue path). Conversely, strong feedback will quickly suppress star formation in the bulge, leading to over-massive SMBHs at high-z (red path). I will make this measurement unambiguously using CL quasars, to inform feedback models in galaxy formation simulations. Figure adapted from McConnell & Ma (2013).

Measuring the $M_{\rm BH}-\sigma_\star$ relation at $z>0$ is notoriously difficult and fraught with systematic biases. The main roadblock for direct measurements is the difficulty of measuring both the $M_{\rm BH}$ (through broad emission line widths) and $\sigma_\star$ (through stellar absorption line widths) for the same objects, since the bright optical AGN continuum emission completely

overwhelms the unresolved host galaxy light. This not only leads to selection biases since only low-luminosity AGN can be used, but also biases in the measurements due to dilution of the stellar absorption lines by the AGN continuum. As a result, current results on the high-z $M_{\rm BH} - \sigma_\star$ relation are contradictory and fundamentally limited by these biases (e.g., Woo et al., 2006, 2008; Shen et al., 2015c).

The ideal method to measure the high-z $M_{\rm BH} - \sigma_\star$ relation would be to first measure $M_{\rm BH}$ from a large sample of quasar spectra, make the quasar emission somehow disappear to reveal the underlying host galaxy, and then obtain another epoch of spectra to measure $\sigma_\star$. The rapid disappearance of nuclear emission recently discovered in CL quasars now enables this approach. However, larger samples beyond the dozen currently-published CL quasars are needed for this measurement.

To identify a large sample of new CL quasars, I will lead searches using incoming spectroscopic data. I will use new multi-epoch optical spectra of 15,000 quasars from the ongoing Time-Domain Spectroscopic Survey in SDSS-IV (Ruan et al., 2016b) to search for CL quasars. Our earliest 300 repeat quasar spectra from this survey have already yielded three cases (e.g. Runnoe et al., 2016), and $\sim$100 more are expected. I am also leading searches for CL quasars from the ARC 3.5m telescope, as part of a collaborative program that uses photometric monitoring of quasars to search for rapid dimming and then trigger follow-up spectroscopy. Current estimates suggest that 12% of quasars undergoing optical dimming of $>$1 mag display changing-look behavior (MacLeod et al., 2015), and our early efforts using this approach have already yielded several new cases.

I estimate that the above searches should yield $>$100 new CL quasars, each with optical spectra both before and after their transitions; this sample is an order of magnitude larger than the currently-known handful of CL quasars. Using this first large sample of multi-epoch CL quasar spectra, I will measure the $M_{\rm BH} - \sigma_\star$ relation as a function of redshift. I will measure $M_{\rm BH}$ using Hα and Hβ broad lines widths, and fit for $\sigma_\star$ using the pPFX software (Cappellari & Emsellem, 2004); this method will probe out to $z \sim 1$. My measurement of the high-z $M_{\rm BH} - \sigma_\star$ relation will be a benchmark constraint on AGN feedback models in

galaxy formation simulations.

6.3 Closing Thoughts

At the beginning of my graduate school career, studies of quasar variability using SDSS Stripe 82 light curves were underway, the Time-Domain Spectroscopic Survey was being proposed, and the Astro2010 decadal survey had just endorsed LSST as the top-priority ground-based telescope project. Now nearly 7 years later, the TDSS is more than halfway finished, quasar variability programs based on repeat spectroscopy have been approved for After Sloan 4 (AS4), and ZTF commissioning is underway. Using these future data, we can hope to answer some still-outstanding fundamental questions about AGN physics: What is the origin of AGN variability? What is the structure of quasar accretion disks? What produces relativistic jets? How do AGN affect the evolution of their host galaxies over cosmic time? The work I presented in this dissertation is a small step to answering some of these questions, and enables new avenues for investigation.

BIBLIOGRAPHY

Abazajian, K. N., Adelman-McCarthy, J. K., Agüeros, M. A., et al. 2009, ApJS, 182, 543

Abdo, A. A., Ackermann, M., Agudo, I., et al. 2010, ApJ, 716, 30

Abdo, A. A., Ackermann, M., Ajello, M., et al. 2010, ApJ, 720, 435

Ackermann, M., Ajello, M., Allafort, A., et al. 2011, ApJ, 743, 171

Ahn, C. P., Alexandroff, R., Allende Prieto, C., et al. 2012, ApJS, 203, 21

Ahn, C. P., Alexandroff, R., Allende Prieto, C., et al. 2014, ApJS, 211, 17

Alam, S., Albareti, F. D., Allende Prieto, C., et al. 2015, ApJS, 219, 12

Alexander, D. M., & Hickox, R. C. 2012, New A Rev., 56, 93

Alexandroff, R., Strauss, M. A., Greene, J. E., et al. 2013, MNRAS, 435, 3306

Andersen, J. 1991, A&A Rev., 3, 91

Andrae, R., Kim, D.-W., & Bailer-Jones, C. A. L. 2013, A&A, 554, A137

Antonucci, R. R. J., & Ulvestad, J. S. 1985, ApJ, 294, 158

Antonucci, R. 1993, ARA&A, 31, 473

Antonucci, R. 2015, arXiv:1501.02001

Arcavi, I., Gal-Yam, A., Sullivan, M., et al. 2014, ApJ, 793, 38

Arévalo, P., Papadakis, I., Kuhlbrodt, B., & Brinkmann, W. 2005, A&A, 430, 435

Armitage, P. J., Reynolds, C. S., & Chiang, J. 2001, ApJ, 548, 868

Armitage, P. J., & Reynolds, C. S. 2003, MNRAS, 341, 1041

Arons, J. 1992, ApJ, 388, 561

Atwood, W. B., Abdo, A. A., Ackermann, M., et al. 2009, ApJ, 697, 1071

Balbus, S. A., & Hawley, J. F. 1991, ApJ, 376, 214

Baldwin, J. A., Phillips, M. M., & Terlevich, R. 1981, PASP, 93, 5

Baloković, M., Smolčić, V., Ivezić, Ž., et al. 2012, ApJ, 759, 30

Bauer, A., Baltay, C., Coppi, P., et al. 2009a, ApJ, 696, 1241

Bauer, A., Baltay, C., Coppi, P., et al. 2009b, ApJ, 705, 46

Bauer, A., Baltay, C., Coppi, P., et al. 2009c, ApJ, 699, 1732

Becker, P. A., & Kafatos, M. 1995a, ApJ, 453, 83

Becker, R. H., White, R. L., & Helfand, D. J. 1995b, ApJ, 450, 559

Beckmann, V., Engels, D., Bade, N., & Wucknitz, O. 2003, A&A, 401, 927

Begelman, M. C., Blandford, R. D., & Rees, M. J. 1984, Reviews of Modern Physics, 56, 255

Bell, E. F., Zucker, D. B., Belokurov, V., et al. 2008, ApJ, 680, 295

Bellm, E. 2014, The Third Hot-wiring the Transient Universe Workshop, 27

Bentz, M. C., Peterson, B. M., Netzer, H., Pogge, R. W., & Vestergaard, M. 2009, ApJ, 697, 160

Blackburne, J. A., Pooley, D., Rappaport, S., & Schechter, P. L. 2011, ApJ, 729, 34

Blanchard, P. K., Nicholl, M., Berger, E., et al. 2017, arXiv:1703.07816

Blandford, R. D., & Znajek, R. L. 1977, MNRAS, 179, 433

Blandford, R. D., & Rees, M. J. 1978, BL Lac Objects, 328

Blandford, R. D., & Levinson, A. 1995, ApJ, 441, 79

Bochanski, J. J., Munn, J. A., Hawley, S. L., et al. 2007, AJ, 134, 2418

Bochanski, J. J., Hawley, S. L., Covey, K. R., et al. 2010, AJ, 139, 2679

Bogdanović, T., Smith, B. D., Sigurdsson, S., & Eracleous, M. 2008, ApJS, 174, 455

Böttcher, M., & Dermer, C. D. 2002, ApJ, 564, 86

Bolton, A. S., Schlegel, D. J., Aubourg, É., et al. 2012, AJ, 144, 144

Bonning, E. W., Cheng, L., Shields, G. A., Salviander, S., & Gebhardt, K. 2007, ApJ, 659, 211

Boroson, T. A., & Green, R. F. 1992, ApJS, 80, 109

Bovy, J., Hennawi, J. F., Hogg, D. W., et al. 2011, ApJ, 729, 141

Bovy, J., Myers, A. D., Hennawi, J. F., et al. 2012, ApJ, 749, 41

Bullock, J. S., & Johnston, K. V. 2005, ApJ, 635, 931

Busca, N. G., Delubac, T., Rich, J., et al. 2013, A&A, 552, AA96

Butler, N. R., & Bloom, J. S. 2011, AJ, 141, 93

Caccianiga, A., Maccacaro, T., Wolter, A., Della Ceca, R., & Gioia, I. M. 2002, ApJ, 566, 181

Cáceres, C., & Catelan, M. 2008, ApJS, 179, 242

Cackett, E. M., Horne, K., & Winkler, H. 2007, MNRAS, 380, 669

Cai, Z., Fan, X., Noterdaeme, P., et al. 2014, ApJ, 793, 139

Cameron, E. 2011, PASA, 28, 128

Cardelli, J. A., Clayton, G. C., & Mathis, J. S. 1989, ApJ, 345, 245

Capellupo, D. M., Hamann, F., Shields, J. C., Rodríguez Hidalgo, P., & Barlow, T. A. 2011, MNRAS, 413, 908

Capellupo, D. M., Hamann, F., Shields, J. C., Rodríguez Hidalgo, P., & Barlow, T. A. 2012, MNRAS, 422, 3249

Cappellari, M., & Emsellem, E. 2004, PASP, 116, 138

Celotti, A., Padovani, P., & Ghisellini, G. 1997, MNRAS, 286, 415

Chambers, K. C., Magnier, E. A., Metcalfe, N., et al. 2016, arXiv:1612.05560

Chatterjee, R., Nalewajko, K., & Myers, A. D. 2013, ApJ, 771, L25

Chornock, R., Berger, E., Gezari, S., et al. 2014, ApJ, 780, 44

Christy, R. F. 1966, ApJ, 144, 108

Churazov, E., Sazonov, S., Sunyaev, R., et al. 2005, MNRAS, 363, L91

Corbett, E. A., Robinson, A., Axon, D. J., et al. 1996, MNRAS, 281, 737

Corbett, E. A., Robinson, A., Axon, D. J., & Hough, J. H. 2000, MNRAS, 311, 485

Covey, K. R., Ivezić, Ž., Schlegel, D., et al. 2007, AJ, 134, 2398

Cutri, R. M., Wisniewski, W. Z., Rieke, G. H., & Lebofsky, M. J. 1985, ApJ, 296, 423

Dai, H., Xie, G. Z., Zhou, S. B., et al. 2007, AJ, 133, 2187

Davenport, J. R. A., Becker, A. C., Kowalski, A. F., et al. 2012, ApJ, 748, 58

Davenport, J. R. A., Hawley, S. L., Hebb, L., et al. 2014, ApJ, 797, 122

Davis, S. W., Woo, J.-H., & Blaes, O. M. 2007, ApJ, 668, 682

Davis, S. W., Blaes, O. M., Hirose, S., & Krolik, J. H. 2009, ApJ, 703, 569

Davis, S. W., & Laor, A. 2011, ApJ, 728, 98

Dawson, K. S., Schlegel, D. J., Ahn, C. P., et al. 2013, AJ, 145, 10

Dawson, K. S., Schlegel, D. J., Ahn, C. P., et al. 2013, AJ, 145, 10

Dawson, K. S., Kneib, J.-P., Percival, W. J., et al. 2015, arXiv:1508.04473

D'Elia, V., Padovani, P., Giommi, P., & Turriziani, S. 2015, MNRAS, 449, 3517

Denney, K. D., De Rosa, G., Croxall, K., et al. 2014, ApJ, 796, 134

Dexter, J., & Agol, E. 2011, ApJ, 727, L24

Di Matteo, T., Springel, V., & Hernquist, L. 2005, Nature, 433, 604

Done, C., & Gierliński, M. 2005, MNRAS, 364, 208

Done, C., Gierliński, M., & Kubota, A. 2007, A&A Rev., 15, 1

D'Orazio, D. J., Haiman, Z., & MacFadyen, A. 2013, MNRAS, 436, 2997

Drake, A. J., Djorgovski, S. G., Mahabal, A., et al. 2009, ApJ, 696, 870

Drake, A. J., Catelan, M., Djorgovski, S. G., et al. 2013a, ApJ, 763, 32

Drake, A. J., Catelan, M., Djorgovski, S. G., et al. 2013b, ApJ, 765, 154

Drake, A. J., Graham, M. J., Djorgovski, S. G., et al. 2014, ApJS, 213, 9

Dwelly, T., & Page, M. J. 2006, MNRAS, 372, 1755

Edelson, R., Vaughan, S., Malkan, M., et al. 2014, ApJ, 795, 2

Edelson, R., Gelbord, J. M., Horne, K., et al. 2015, ApJ, 806, 129

Eisenstein, D. J., Weinberg, D. H., Agol, E., et al. 2011, AJ, 142, 72

Elitzur, M., & Ho, L. C. 2009, ApJ, 701, L91

Eracleous, M., Livio, M., & Binette, L. 1995, ApJ, 445, L1

Eracleous, M., Boroson, T. A., Halpern, J. P., & Liu, J. 2012, ApJS, 201, 23

Fabian, A. C. 2012, ARA&A, 50, 455

Fan, X. 1999, AJ, 117, 2528

Farris, B. D., Duffell, P., MacFadyen, A. I., & Haiman, Z. 2015, MNRAS, 446, L36

Filippenko, A. V. 1989, AJ, 97, 726

Filippenko, A. V. 1997, ARA&A, 35, 309

Filiz Ak, N., Brandt, W. N., Hall, P. B., et al. 2012, ApJ, 757, 114

Filiz Ak, N., Brandt, W. N., Hall, P. B., et al. 2013, arXiv:1309.5364

Fine, S., Jarvis, M. J., & Mauch, T. 2011, MNRAS, 412, 213

Font, A. S., McCarthy, I. G., Crain, R. A., et al. 2011, MNRAS, 416, 2802

Font-Ribera, A., Miralda-Escudé, J., Arnau, E., et al. 2012, JCAP, 11, 059

Font-Ribera, A., Kirkby, D., Busca, N., et al. 2014, JCAP, 5, 027

Fossati, G., Maraschi, L., Celotti, A., Comastri, A., & Ghisellini, G. 1998, MNRAS, 299, 433

Francis, P. J., Hewett, P. C., Foltz, C. B., et al. 1991, ApJ, 373, 465

Frank, J., King, A., & Raine, D. J. 2002, Accretion Power in Astrophysics, by Juhan Frank and Andrew King and Derek Raine, pp. 398. ISBN 0521620538. Cambridge, UK: Cambridge University Press, February 2002.,

Gammie, C. F. 1998, MNRAS, 297, 929

Garcia, A., Sodré, L., Jablonski, F. J., & Terlevich, R. J. 1999, MNRAS, 309, 803

Gaskell, C. M. 1982, ApJ, 263, 79

Genzel, R., & Townes, C. H. 1987, ARA&A, 25, 377

Gezari, S., Martin, D. C., Milliard, B., et al. 2006, ApJ, 653, L25

Gezari, S., Heckman, T., Cenko, S. B., et al. 2009, ApJ, 698, 1367

Gezari, S., Chornock, R., Rest, A., et al. 2012, Nature, 485, 217

Gezari, S., Martin, D. C., Forster, K., et al. 2013, ApJ, 766, 60

Gezari, S., Hung, T., Cenko, S. B., et al. 2017, ApJ, 835, 144

Ghisellini, G., & Tavecchio, F. 2008, MNRAS, 387, 1669

Ghisellini, G., Tavecchio, F., Foschini, L., & Ghirlanda, G. 2011, MNRAS, 414, 2674

Gibson, R. R., Brandt, W. N., Schneider, D. P., & Gallagher, S. C. 2008, ApJ, 675, 985

Gibson, R. R., Jiang, L., Brandt, W. N., et al. 2009, ApJ, 692, 758

Gibson, R. R., Brandt, W. N., Gallagher, S. C., Hewett, P. C., & Schneider, D. P. 2010, ApJ, 713, 220

Gilmore, G., Randich, S., Asplund, M., et al. 2012, The Messenger, 147, 25

Giommi, P., Padovani, P., Polenta, G., et al. 2012, MNRAS, 420, 2899

Giveon, U., Maoz, D., Kaspi, S., Netzer, H., & Smith, P. S. 1999, MNRAS, 306, 637

Gizis, J. E., Reid, I. N., & Hawley, S. L. 2002, AJ, 123, 3356

Glikman, E., Urrutia, T., Lacy, M., et al. 2013, ApJ, 778, 127

Goodrich, R. W. 1995, ApJ, 440, 141

Graham, M. J., Djorgovski, S. G., Drake, A. J., et al. 2014, MNRAS, 439, 703

Graham, M. J., Djorgovski, S. G., Stern, D., et al. 2015, Nature, 518, 74

Green, P. J., Anderson, S. F., Morganson, E., et al. 2014, American Astronomical Society Meeting Abstracts, 223, #116.15

Greene, J. E., & Ho, L. C. 2005, ApJ, 630, 122

Greene, J. E., Peng, C. Y., & Ludwig, R. R. 2010, ApJ, 709, 937

Grier, C. J., Hall, P. B., Brandt, W. N., et al. 2015, ApJ, 806, 111

Guainazzi, M. 2002, MNRAS, 329, L13

Gunn, J. E., Carr, M., Rockosi, C., et al. 1998, AJ, 116, 3040

Gunn, J. E., Siegmund, W. A., Mannery, E. J., et al. 2006, AJ, 131, 2332

Hadjiyska, E., Rabinowitz, D., Baltay, C., et al. 2012, IAU Symposium, 285, 324

Haehnelt, M. G., Natarajan, P., & Rees, M. J. 1998, MNRAS, 300, 817

Hainline, K. N., Hickox, R., Greene, J. E., Myers, A. D., & Zakamska, N. L. 2013, ApJ, 774, 145

Hall, P. B., Anderson, S. F., Strauss, M. A., et al. 2002, ApJS, 141, 267

Hall, P. B., Brandt, W. N., Petitjean, P., et al. 2013, MNRAS, 434, 222

Hawley, S. L., & Pettersen, B. R. 1991, ApJ, 378, 725

Hawley, S. L., Gizis, J. E., & Reid, I. N. 1996, AJ, 112, 2799

Hickox, R. C., Mullaney, J. R., Alexander, D. M., et al. 2014, ApJ, 782, 9

Hirose, S., Krolik, J. H., & Blaes, O. 2009, ApJ, 691, 16

Hinshaw, G., Larson, D., Komatsu, E., et al. 2013, ApJS, 208, 19

Holoien, T. W.-S., Prieto, J. L., Bersier, D., et al. 2014, MNRAS, 445, 3263

Homan, J., & Belloni, T. 2005, Ap&SS, 300, 107

Hook, I. M., McMahon, R. G., Boyle, B. J., & Irwin, M. J. 1994, MNRAS, 268, 305

Hopkins, P. F., Hernquist, L., Martini, P., et al. 2005, ApJ, 625, L71

Hopkins, P. F., Hernquist, L., Cox, T. J., Keres, D., & Wuyts, S. 2009, ApJ, 691, 1424

Ichimaru, S. 1977, ApJ, 214, 840

Isler, J. C., Urry, C. M., Coppi, P., et al. 2013, ApJ, 779, 100

Ivezić, Ž., Menou, K., Knapp, G. R., et al. 2002, AJ, 124, 2364

Ivezić, Ž., Smith, J. A., Miknaitis, G., et al. 2007, AJ, 134, 973

Ivezic, Z., Tyson, J. A., Abel, B., et al. 2008, arXiv:0805.2366

Jarvis, M. J., & McLure, R. J. 2006, MNRAS, 369, 182

Janiuk, A., & Misra, R. 2012, A&A, 540, A114

Jiang, Y.-F., Stone, J. M., & Davis, S. W. 2013, ApJ, 767, 148

Jiang, Y.-F., Green, P. J., Greene, J. E., et al. 2017, ApJ, 836, 186

Jiménez-Vicente, J., Mediavilla, E., Kochanek, C. S., et al. 2014, ApJ, 783, 47

Johnston, K. V., Bullock, J. S., Sharma, S., et al. 2008, ApJ, 689, 936

Kaiser, N., Aussel, H., Burke, B. E., et al. 2002, Proc. SPIE, 4836, 154

Kaiser, N., Burgett, W., Chambers, K., et al. 2010, Proc. SPIE, 7733, 77330E

Kauffmann, G., Heckman, T. M., Tremonti, C., et al. 2003, MNRAS, 346, 1055

Keel, W. C., Lintott, C. J., Schawinski, K., et al. 2012a, AJ, 144, 66

Keel, W. C., Chojnowski, S. D., Bennert, V. N., et al. 2012b, MNRAS, 420, 878

Keel, W. C., Maksym, W. P., Bennert, V. N., et al. 2015, AJ, 149, 155

Keel, W. C., Lintott, C. J., Maksym, W. P., et al. 2017, ApJ, 835, 256

Keller, S. C., Murphy, S., Prior, S., Da Costa, G., & Schmidt, B. 2008, ApJ, 678, 851

Kelly, B. C., Bechtold, J., & Siemiginowska, A. 2009, ApJ, 698, 895

Kelly, B. C., Vestergaard, M., Fan, X., et al. 2010, ApJ, 719, 1315

Kelly, B. C., Sobolewska, M., & Siemiginowska, A. 2011, ApJ, 730, 52

Kewley, L. J., Dopita, M. A., Sutherland, R. S., Heisler, C. A., & Trevena, J. 2001, ApJ, 556, 121

Kim, D.-W., Protopapas, P., Byun, Y.-I., et al. 2011, ApJ, 735, 68

Kishimoto, M., Antonucci, R., Blaes, O., et al. 2008, Nature, 454, 492

Knigge, C., Scaringi, S., Goad, M. R., & Cottis, C. E. 2008, MNRAS, 386, 1426

Kollgaard, R. I., Wardle, J. F. C., Roberts, D. H., & Gabuzda, D. C. 1992, AJ, 104, 1687

Kormendy, J., & Richstone, D. 1995, ARA&A, 33, 581

Kowalski, A. F., Hawley, S. L., Hilton, E. J., et al. 2009, AJ, 138, 633

Kowalski, A. F., Hawley, S. L., Wisniewski, J. P., et al. 2013, ApJS, 207, 15

Kozłowski, S., Kochanek, C. S., Udalski, A., et al. 2010, ApJ, 708, 927

Kraus, A. L., & Hillenbrand, L. A. 2007, AJ, 134, 2340

Krolik, J. H., Hawley, J. F., & Hirose, S. 2005, ApJ, 622, 1008

LaMassa, S. M., Cales, S., Moran, E. C., et al. 2015, ApJ, 800, 144

Law, N. M., Kulkarni, S. R., Dekany, R. G., et al. 2009, PASP, 121, 1395

Lépine, S., & Gaidos, E. 2011, AJ, 142, 138

Levi, M., Bebek, C., Beers, T., et al. 2013, arXiv:1308.0847

Li, S.-L., & Cao, X. 2008, MNRAS, 387, L41

Lin, D. N. C., & Shields, G. A. 1986, ApJ, 305, 28

Lin, D., Guillochon, J., Komossa, S., et al. 2017, Nature Astronomy, 1, 0033

Lintott, C. J., Schawinski, K., Keel, W., et al. 2009, MNRAS, 399, 129

Liu, G., Zakamska, N. L., Greene, J. E., Nesvadba, N. P. H., & Liu, X. 2013, MNRAS, 430, 2327

Liu, T., Gezari, S., Heinis, S., et al. 2015, ApJ, 803, L16

Lodato, G., King, A. R., & Pringle, J. E. 2009, MNRAS, 392, 332

Lodato, G., & Rossi, E. M. 2011, MNRAS, 410, 359

Lynden-Bell, D. 1969, Nature, 223, 690

Lynden-Bell, D., & Rees, M. J. 1971, MNRAS, 152, 461

Maccacaro, T., Gioia, I. M., Maccagni, D., & Stocke, J. T. 1984, ApJ, 284, L23

MacLeod, C. L., Ivezić, Ž., Kochanek, C. S., et al. 2010, ApJ, 721, 1014

MacLeod, C. L., Brooks, K., Ivezić, Ž., et al. 2011, ApJ, 728, 26

MacLeod, C. L., Ross, N. P., Lawrence, A., et al. 2015, arXiv:1509.08393

MacLeod, C. L., Green, P. J., Anderson, S. F., et al. 2017, arXiv:1706.04240

Malkan, M. A., & Sargent, W. L. W. 1982, ApJ, 254, 22

Maoz, D., Edelson, R., & Nandra, K. 2000, AJ, 119, 119

Maraschi, L., & Tavecchio, F. 2003, ApJ, 593, 667

Marchã, M. J. M., & Caccianiga, A. 2013, MNRAS, 430, 2464

Marchese, E., Braito, V., Della Ceca, R., Caccianiga, A., & Severgnini, P. 2012, MNRAS, 421, 1803

Martini, P., & Weinberg, D. H. 2001, ApJ, 547, 12

Massaro, E., Giommi, P., Leto, C., et al. 2009, A&A, 495, 691

Matt, G., Guainazzi, M., & Maiolino, R. 2003, MNRAS, 342, 422

McConnell, N. J., & Ma, C.-P. 2013, ApJ, 764, 184

McGreer, I. D., Jiang, L., Fan, X., et al. 2013, ApJ, 768, 105

McHardy, I. M., Cameron, D. T., Dwelly, T., et al. 2014, MNRAS, 444, 1469

McLure, R. J., & Dunlop, J. S. 2004, MNRAS, 352, 1390

Melia, F., & Falcke, H. 2001, ARA&A, 39, 309

Merloni, A., Dwelly, T., Salvato, M., et al. 2015, MNRAS, 452, 69

Meusinger, H., Hinze, A., & de Hoon, A. 2011, A&A, 525, A37

Meusinger, H., & Weiss, V. 2013, A&A, 560, A104

Moderski, R., Sikora, M., Coppi, P. S., & Aharonian, F. 2005, MNRAS, 363, 954

Moffett, T. J. 1974, ApJS, 29, 1

Morgan, C. W., Kochanek, C. S., Morgan, N. D., & Falco, E. E. 2010, ApJ, 712, 1129

Morganson, E., Green, P. J., Anderson, S. F., et al. 2015, ApJ, 806, 244

Mortlock, D. J., Warren, S. J., Venemans, B. P., et al. 2011, Nature, 474, 616

Murray, N., Chiang, J., Grossman, S. A., & Voit, G. M. 1995, ApJ, 451, 498

Mushotzky, R. F., Edelson, R., Baumgartner, W., & Gandhi, P. 2011, ApJ, 743, LL12

Myers, A. D., Brunner, R. J., Richards, G. T., et al. 2006, ApJ, 638, 622

Myers, A. D., Brunner, R. J., Nichol, R. C., et al. 2007a, ApJ, 658, 85

Myers, A. D., Brunner, R. J., Richards, G. T., et al. 2007b, ApJ, 658, 99

Myers, A. D., Palanque-Delabrouille, N., Prakash, A., et al. 2015, ApJS, 221, 27

Narayan, R., & Yi, I. 1994, ApJ, 428, L13

Netzer, H., & Laor, A. 1993, ApJ, 404, L51

Nicastro, F., Martocchia, A., & Matt, G. 2003, ApJ, 589, L13

Noble, S. C., Krolik, J. H., & Hawley, J. F. 2009, ApJ, 692, 411

Noble, S. C., & Krolik, J. H. 2009, ApJ, 703, 964

Nolan, P. L., Abdo, A. A., Ackermann, M., et al. 2012, ApJS, 199, 31

Osten, R. A., Hawley, S. L., Allred, J. C., Johns-Krull, C. M., & Roark, C. 2005, ApJ, 621, 398

Padmanabhan, N., Schlegel, D. J., Finkbeiner, D. P., et al. 2008, ApJ, 674, 1217-1233

Padovani, P., & Giommi, P. 1995, MNRAS, 277, 1477

Padovani, P., Giommi, P., Landt, H., & Perlman, E. S. 2007, ApJ, 662, 182

Palanque-Delabrouille, N., Yeche, C., Myers, A. D., et al. 2011, A&A, 530, AA122

Palanque-Delabrouille, N., Magneville, C., Yèche, C., et al. 2015, arXiv:1509.05607

Pâris, I., Petitjean, P., Aubourg, É., et al. 2014, A&A, 563, A54

Pâris, I., Petitjean, P., Ross, N. P., et al. 2017, A&A, 597, A79

Penna, R. F., McKinney, J. C., Narayan, R., et al. 2010, MNRAS, 408, 752

Pereyra, N. A., Vanden Berk, D. E., Turnshek, D. A., et al. 2006, ApJ, 642, 87

Perlman, E. S., Stocke, J. T., Schachter, J. F., et al. 1996, ApJS, 104, 251

Planck Collaboration, Ade, P. A. R., Aghanim, N., et al. 2015, arXiv:1502.01589

Plotkin, R. M., Anderson, S. F., Brandt, W. N., et al. 2010, AJ, 139, 390

Pringle, J. E. 1981, ARA&A, 19, 137

Pringle, J. E., & Rees, M. J. 1972, A&A, 21, 1

Proga, D., Stone, J. M., & Kallman, T. R. 2000, ApJ, 543, 686

Puccetti, S., Fiore, F., Risaliti, G., et al. 2007, MNRAS, 377, 607

Rector, T. A., Stocke, J. T., Perlman, E. S., Morris, S. L., & Gioia, I. M. 2000, AJ, 120, 1626

Rees, M. J., Begelman, M. C., Blandford, R. D., & Phinney, E. S. 1982, Nature, 295, 17

Rees, M. J. 1978, Phys. Scr, 17, 193

Rees, M. J. 1988, Nature, 333, 523

Reichard, T. A., Richards, G. T., Hall, P. B., et al. 2003, AJ, 126, 2594

Reid, I. N., Hawley, S. L., & Gizis, J. E. 1995, AJ, 110, 1838

Reid, I. N., Gizis, J. E., Cohen, J. G., et al. 1997, PASP, 109, 559

Reiners, A., & Basri, G. 2010, ApJ, 710, 924

Richards, G. T., Fan, X., Newberg, H. J., et al. 2002a, AJ, 123, 2945

Richards, G. T., Vanden Berk, D. E., Reichard, T. A., et al. 2002b, AJ, 124, 1

Richards, G. T., Lacy, M., Storrie-Lombardi, L. J., et al. 2006, ApJS, 166, 470

Richards, G. T., Kruczek, N. E., Gallagher, S. C., et al. 2011, AJ, 141, 167

Risaliti, G., Salvati, M., Elvis, M., et al. 2009, MNRAS, 393, L1

Robertson, B., Bullock, J. S., Cox, T. J., et al. 2006, ApJ, 645, 986

Ross, N. P., Shen, Y., Strauss, M. A., et al. 2009, ApJ, 697, 1634

Ross, N. P., Myers, A. D., Sheldon, E. S., et al. 2012, ApJS, 199, 3

Ross, N. P., McGreer, I. D., White, M., et al. 2013, ApJ, 773, 14

Ross, N. P., Hamann, F., Zakamska, N. L., et al. 2014, arXiv:1405.1047

Ruan, J. J., Anderson, S. F., MacLeod, C. L., et al. 2012, ApJ, 760, 51

Ruan, J. J., Anderson, S. F., Dexter, J., & Agol, E. 2014a, ApJ, 783, 105

Ruan, J. J., Anderson, S. F., Plotkin, R. M., et al. 2014b, ApJ, 797, 19

Ruan, J. J., Anderson, S. F., Cales, S. L., et al. 2016a, ApJ, 826, 188

Ruan, J. J., Anderson, S. F., Green, P. J., et al. 2016b, ApJ, 825, 137

Runnoe, J. C., Brotherton, M. S., & Shang, Z. 2012, MNRAS, 422, 478

Runnoe, J. C., Brotherton, M. S., Shang, Z., Wills, B. J., & DiPompeo, M. A. 2013, MNRAS, 429, 135

Runnoe, J. C., Cales, S., Ruan, J. J., et al. 2016, MNRAS, 455, 1691

Sakata, Y., Morokuma, T., Minezaki, T., et al. 2011, ApJ, 731, 50

Salpeter, E. E. 1964, ApJ, 140, 796

Sambruna, R. M., Maraschi, L., & Urry, C. M. 1996, ApJ, 463, 444

Sarzi, M., Falcón-Barroso, J., Davies, R. L., et al. 2006, MNRAS, 366, 1151

Sartori, L. F., Schawinski, K., Koss, M., et al. 2016, MNRAS, 457, 3629

Sbarrato, T., Ghisellini, G., Maraschi, L., & Colpi, M. 2012, MNRAS, 421, 1764

Schawinski, K., Evans, D. A., Virani, S., et al. 2010, ApJ, 724, L30

Schawinski, K., Koss, M., Berney, S., & Sartori, L. F. 2015, MNRAS, 451, 2517

Schlafly, E. F., & Finkbeiner, D. P. 2011, ApJ, 737, 103

Schlegel, D. J., Finkbeiner, D. P., & Davis, M. 1998, ApJ, 500, 525

Schmidt, M. 1963, Nature, 197, 1040

Schmidt, K. B., Marshall, P. J., Rix, H.-W., et al. 2010, ApJ, 714, 1194

Schmidt, K. B., Rix, H.-W., Shields, J. C., et al. 2012, ApJ, 744, 147 (SC12)

Schmidt, S. J., Hawley, S. L., West, A. A., et al. 2015, AJ, 149, 158

Schneider, D. P., Richards, G. T., Hall, P. B., et al. 2010, AJ, 139, 2360

SDSS Collaboration, Albareti, F. D., Allende Prieto, C., et al. 2016, arXiv:1608.02013

Sesar, B., Ivezić, Ž., Lupton, R. H., et al. 2007, AJ, 134, 2236

Sesar, B., Ivezić, Ž., Grammer, S. H., et al. 2010, ApJ, 708, 717

Sesar, B., Stuart, J. S., Ivezić, Ž., et al. 2011, AJ, 142, 190

Sesar, B., Ivezić, Ž., Stuart, J. S., et al. 2013, AJ, 146, 21

Shakura, N. I., & Sunyaev, R. A. 1973, A&A, 24, 337

Shang, Z., Brotherton, M. S., Green, R. F., et al. 2005, ApJ, 619, 41

Shappee, B. J., Prieto, J. L., Grupe, D., et al. 2014, ApJ, 788, 48

Shaw, M. S., Romani, R. W., Cotter, G., et al. 2012, ApJ, 748, 49

Shaw, M. S., Romani, R. W., Cotter, G., et al. 2013, ApJ, 764, 135

Shaw, M. S., Filippenko, A. V., Romani, R. W., Cenko, S. B., & Li, W. 2013b, AJ, 146, 127

Shen, Y., Greene, J. E., Strauss, M. A., Richards, G. T., & Schneider, D. P. 2008, ApJ, 680, 169

Shen, Y., Richards, G. T., Strauss, M. A., et al. 2011, ApJS, 194, 45

Shen, Y., McBride, C. K., White, M., et al. 2013, ApJ, 778, 98

Shen, Y., Brandt, W. N., Dawson, K. S., et al. 2015a, ApJS, 216, 4

Shen, Y., Horne, K., Grier, C. J., et al. 2015b, arXiv:1510.02802

Shen, Y., Greene, J. E., Ho, L. C., et al. 2015c, ApJ, 805, 96

Shields, G. A. 1978, Nature, 272, 706

Siemiginowska, A., Czerny, B., & Kostyunin, V. 1996, ApJ, 458, 491

Slosar, A., Iršič, V., Kirkby, D., et al. 2013, JCAP, 4, 026

Smee, S. A., Gunn, J. E., Uomoto, A., et al. 2013, AJ, 146, 32

Sobolewska, M. A., Siemiginowska, A., & Gierliński, M. 2011, MNRAS, 413, 2259

Soltan, A. 1982, MNRAS, 200, 115

Springel, V., Di Matteo, T., & Hernquist, L. 2005, MNRAS, 361, 776

Starkey, D., Horne, K., Fausnaugh, M. M., et al. 2017, ApJ, 835, 65

Stickel, M., Padovani, P., Urry, C. M., Fried, J. W., & Kuehr, H. 1991, ApJ, 374, 431

Stocke, J. T., Morris, S. L., Gioia, I. M., et al. 1991, ApJS, 76, 813

Stokes, G. H., Evans, J. B., Viggh, H. E. M., Shelly, F. C., & Pearce, E. C. 2000, Icarus, 148, 21

Stoughton, C., Lupton, R. H., Bernardi, M., et al. 2002, AJ, 123, 485

Stratta, G., Capalbi, M., Giommi, P., et al. 2011, arXiv:1103.0749

Strubbe, L. E., & Quataert, E. 2009, MNRAS, 400, 2070

SubbaRao, M., Frieman, J., Bernardi, M., et al. 2002, Proc. SPIE, 4847, 452

Taddia, F., Stritzinger, M. D., Sollerman, J., et al. 2013, A&A, 555, A10

Tadhunter, C., Spence, R., Rose, M., Mullaney, J., & Crowther, P. 2017, Nature Astronomy, 1, 0061

Taylor, P., & Kobayashi, C. 2016, MNRAS, 463, 2465

The Fermi-LAT Collaboration 2015, arXiv:1501.02003

Thomas, D., Steele, O., Maraston, C., et al. 2013, MNRAS, 431, 1383

Torres, G., Andersen, J., & Giménez, A. 2010, A&A Rev., 18, 67

Tozzi, P., Gilli, R., Mainieri, V., et al. 2006, A&A, 451, 457

Trèvese, D., Kron, R. G., & Bunone, A. 2001, ApJ, 551, 103

Trèvese, D., & Vagnetti, F. 2002, ApJ, 564, 624

Trump, J. R., Hall, P. B., Reichard, T. A., et al. 2006, ApJS, 165, 1

Turner, N. J., Blaes, O. M., Socrates, A., Begelman, M. C., & Davis, S. W. 2005, ApJ, 624, 267

Udalski, A., Szymanski, M. K., Soszynski, I., & Poleski, R. 2008, Acta Astronomica, 58, 69

Ulrich, M.-H., Maraschi, L., & Urry, C. M. 1997, ARA&A, 35, 445

Urry, C. M., & Padovani, P. 1995, PASP, 107, 803

Uttley, P., Edelson, R., McHardy, I. M., Peterson, B. M., & Markowitz, A. 2003, ApJ, 584, L53

Vanden Berk, D. E., Richards, G. T., Bauer, A., et al. 2001, AJ, 122, 549

Vanden Berk, D. E., Wilhite, B. C., Kron, R. G., et al. 2004, ApJ, 601, 692

Vanden Berk, D. E., Shen, J., Yip, C.-W., et al. 2006, AJ, 131, 84

Vermeulen, R. C., Ogle, P. M., Tran, H. D., et al. 1995, ApJ, 452, L5

Vestergaard, M., & Peterson, B. M. 2006, ApJ, 641, 689

Volonteri, M. 2012, Science, 337, 544

Wang, J.-M., Staubert, R., & Ho, L. C. 2002, ApJ, 579, 554

Weaver, B. A., Blanton, M. R., Brinkmann, J., Brownstein, J. R., & Stauffer, F. 2015, PASP, 127, 397

West, A. A., Hawley, S. L., Walkowicz, L. M., et al. 2004, AJ, 128, 426

West, A. A., Bochanski, J. J., Hawley, S. L., et al. 2006, AJ, 132, 2507

West, A. A., Hawley, S. L., Bochanski, J. J., et al. 2008, AJ, 135, 785

West, A. A., & Basri, G. 2009, ApJ, 693, 1283

West, A. A., Morgan, D. P., Bochanski, J. J., et al. 2011, AJ, 141, 97

Weymann, R. J., Morris, S. L., Foltz, C. B., & Hewett, P. C. 1991, ApJ, 373, 23

Wilhite, B. C., Vanden Berk, D. E., Kron, R. G., et al. 2005, ApJ, 633, 638 (WI05)

Wilhite, B. C., Brunner, R. J., Grier, C. J., Schneider, D. P., & vanden Berk, D. E. 2008, MNRAS, 383, 1232

Wills, B. J., & Browne, I. W. A. 1986, ApJ, 302, 56

Wolter, A., Caccianiga, A., della Ceca, R., & Maccacaro, T. 1994, ApJ, 433, 29

Woo, J.-H., Treu, T., Malkan, M. A., & Blandford, R. D. 2008, ApJ, 681, 925-930

Woo, J.-H., Treu, T., Malkan, M. A., & Blandford, R. D. 2006, ApJ, 645, 900

Wyrzykowski, Ł., Kostrzewa-Rutkowska, Z., Kozłowski, S., et al. 2014, Acta Astronomica, 64, 197

Yip, C. W., Connolly, A. J., Vanden Berk, D. E., et al. 2004a, AJ, 128, 2603

Yip, C. W., Connolly, A. J., Szalay, A. S., et al. 2004b, AJ, 128, 585

York, D. G., Adelman, J., Anderson, J. E., Jr., et al. 2000, AJ, 120, 1579

Zheng, W., Kriss, G. A., Telfer, R. C., Grimes, J. P., & Davidsen, A. F. 1997, ApJ, 475, 469

Zu, Y., Kochanek, C. S., Kozłowski, S., & Udalski, A. 2013, ApJ, 765, 106

Zuo, W., Wu, X.-B., Liu, Y.-Q., & Jiao, C.-L. 2012, ApJ, 758, 104